An Abstract of the Thesis of

Bianca A. Hermann for the degree of Master of Science in Physics presented on August 21, 1992.

Title: Resistance in Superconductors - A Comparison between NdCeCuO and YBaCuO Thin Films.

Redacted for privacy

Abstract approved: _____

Dr. Janet Tate

Stable current-voltage characteristics and resistance-temperature curves for thin-film samples of the high temperature superconductors $Nd_{2-x}Ce_xCuO_{4-\delta}$ and $Y_1Ba_2Cu_3O_{6+x}$ were obtained for magnetic fields up to 8 T and for temperatures around the superconducting transition temperatures. The resistance in the low-current regime was analysed within the framework of thermally activated motion of flux lines, and the field- and temperature-dependent activation energies were found by two different methods. For $Y_1Ba_2Cu_3O_{6+x}$, the activation energy ranged from 1 to 150 eV for fields from 8 to 1 T, and for $Nd_{2-x}Ce_xCuO_{4-\delta}$, 5 to 50 meV for the same field range. Two limits of thermally activated flux motion, flux creep and thermally assisted flux flow, were identified in the current-voltage characteristics, as well as a transition to a vortex-glass state. For $Y_1Ba_2Cu_3O_{6+x}$, isothermal current-voltage characteristics at constant field could be scaled onto two universal curves with scaling exponents $\nu = 1.65$, $z = 4.95$ and $d = 3$.

A low-noise, variable-temperature cryostat was brought into operation, and the parameters for control in liquid helium and nitrogen coolants were found. A computer interface was established to regulate temperature and to measure the voltage drop across the superconductor.

Resistance in Superconductors - A Comparison between NdCeCuO and YBaCuO Thin Films

by

Bianca A. Hermann

A THESIS

submitted to

Oregon State University

in partial fulfillment of

the requirements for the

degree of

Master of Science

Completed August 21, 1992

Commencement June 1993

APPROVED:

Redacted for privacy

Assistant Professor of Physics in charge of major

Redacted for privacy

Chairman of the Department of Physics

Redacted for privacy

Dean of Graduate School

Date thesis is presented August 21, 1992

Typed by Bianca Hermann for Bianca A. Hermann

Acknowledgements

I would like to acknowledge the Baden-Württemberg - Oregon exchange program, without which it would not have been possible to study at Oregon State University. Being a participant in the International Cultural Service Program (ICSP) not only paid my tuition for the second year, but also improved my speech skills and cultural awareness. The summer support from Dr. Tate's Sloan fellowship supplemented my living expenses.

I have to thank Dr. Tate for her outstanding guidance throughout this project, the freedom I had in conducting this research and the time consuming grammar corrections and suggestions on the content of my thesis. Both Dr. Tate and Susan Schwartz, program director of ICSP, have been excellent role models.

My fellow students within the research group were very supportive. I would like to acknowledge the numerous scientific discussions I had with Jeanette Roberts, Goran Karapetrov, and Dennis Tom; the useful inputs and help I got from the undergraduate students Jeff Arasmith, Joel Dille and Amy Spofford. I am thankful to all my fellow students for giving me a hand in soldering unpleasant connectors, taking and analyzing data, even during the night and on weekends.

I would like to thank my committee members and Dr. Gardner for suggestions on my research and generosity with their time and advice, and also, Dr. Krane and Dr. Manogue for their valuable career advice.

I have to thank Dr. Halbritter and Prof. Wühl for their inputs and valuable suggestions. I also would like to acknowledge the encouragements from Prof. Martensen and Prof. Engelhardt to study abroad.

I thank John Archibald for his excellent machining skills and his patience with our designs.

My parents not only financially supported me, but also showed a lot of interest in my work.

Last but not least, I have to acknowledge Holger Delfs for all the emotional support I received from him and for reminding me that there are other things besides physics.

Table of Contents

List of Figures

List of Tables

List of Appendix Figures

Resistance in Superconductors - A Comparison between NdCeCuO and YBaCuO Thin Films

1. Introduction

The superconductor $Nd_{2-x}Ce_xCuO_{4-\delta}$, discovered in 1989[1], has a special place in the high critical temperature copper oxide superconductor family. Hall effect measurements[2,3] revealed that its charge carriers are electrons and not holes as in many other high T_c superconductors. There are at least three other reasons which make it exciting to study this material; it's simple structure of equally spaced CuO_2 sheets separated by Nd-O layers (see chapter 1.2) and second the two dimensionality some authors see and some others do not. Third, the fact that it has some qualities which put it rather close to conventional type II superconductors. Some authors claim it could be a bridge between conventional and high T_c superconductors[4].

We chose resistance measurements to compare thin film samples of $Nd_{2-x}Ce_xCuO_{4-\delta}$ with $Y_1Ba_2Cu_3O_{6+x}$. Since it is difficult to obtain high quality thin film samples of $Nd_{2-x}Ce_xCuO_{4-\delta}$ the studies on this material have been rather limited. A comparison with a hole superconductor was straightforward. The highly studied $Y_1Ba_2Cu_3O_{6+x}$ seemed a good choice, because we wanted to test our brand new system for the transport measurements. A lot of effort in this work went into getting the set up and software to work in the first place and then to perform at its best (see chapter 2 for details). Another reason for comparing just these two

materials was to have good quality samples available of both of them *prepared by the same method* of thermal co-evaporation, which is described in chapter 1.3. The analysis of the resistance measurements was extensive. Not everything is presented in this thesis. The presented material is organized as follows: current-voltage characteristics are described in the third chapter and resistance-temperature in the fourth. In chapter 5 all conclusions of this work are summarized.

1.1 Resistance in Type II Superconductors

When Bednorz and Müller (1986) discovered the first high critical temperature (high T_c) superconductor[5], the excitement about being able to build a high field magnet was enormous. Soon researchers discovered that despite high critical current, high critical fields and T_c's above liquid nitrogen temperature, the new materials showed a broad transition in a magnetic field and the resistivity was very small but not zero below T_c. The effects causing this were not unknown, but became now accessible due to the high critical temperatures of the new materials.

The new materials, like most of the superconductors discovered until today, are type II superconductors. In fact only a small number, the element superconductors with the exception of Nb, V and Tc, are of type I. The classification type II or type I depends on the behavior of the superconductor in magnetic field. A type I superconductor expels all magnetic field from its interior below a field H_c. A type II superconductor reaches a minimum in the Gibbs free energy by allowing the magnetic flux to penetrate into the superconductor in small

quantized quantities ϕ_0. The quantized magnetic field arranges itself in long cylindrical tubes (flux lines or vortices) in a hexagonal array. In such a superconductor left by itself, thermal vibrations lead to a random motion of the vortices (see e.g. [6]).

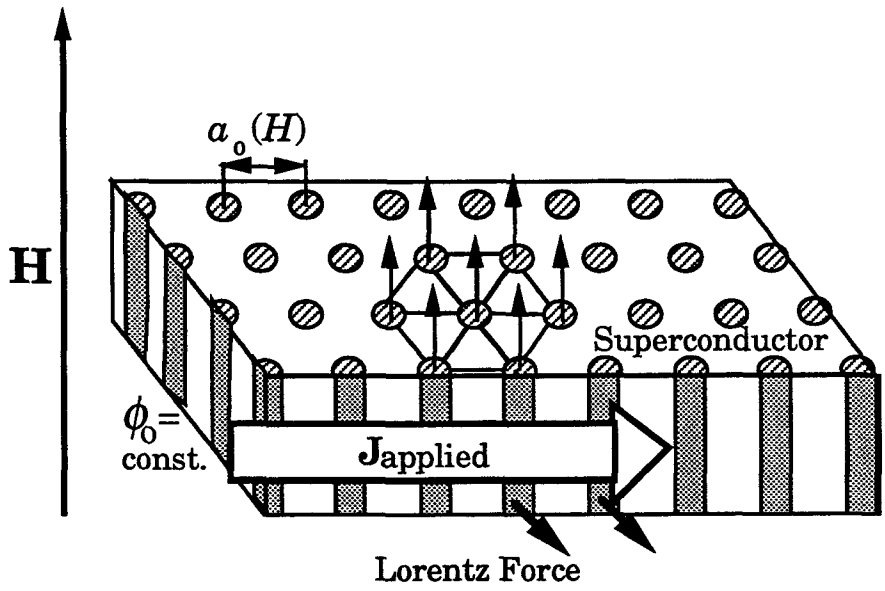

Figure 1.1 Flux lattice in a type II superconductor. The vortices form a hexagonal array.

In a magnet application a transport current is applied to the superconductor, just like we apply a measuring current. The magnetic field acts on the current with a Lorentz force and the applied current will react on the vortices with the same force. This causes the flux lines to move. A vortex can be modeled as normal region within the superconductor. A moving flux line has to break superconducting pairs in front of it and recreate them behind. Another way of looking at it is, that within the flux line there are normal electrons; if they move through a material they interact with phonos, just like electrons in a metal. This causes the observed resistance in type II superconductors below T_c.

If the flux lines could be held down, the Lorentz force would have to overcome a potential and until then perfect conductance would be established. In fact it turns out that imperfection and dirt in the material or any normal region within a superconductor can hold flux lines down, because it is energetically favorable for them to stay there. Since energy has to be provided to drive a superconducting region normal, vortices prefer those parts of the superconductor which are already partially or fully normal conducting. The exact mechanisms of the Lorentz force overcoming the pinning strength are described by many different models, which will be discussed in detail in chapter 3 and 4. Twin boundaries, screw dislocations and defects in the material can act as pinning centers. In order to implant such pinning centers it is important to understand the mechanism behind pinning and be able to describe it. Since there are no perfect materials, studying transport measurements means studying pinning. A good and brief overview on type II superconductivity is given in [7].

1.2 Important Length Scales and Critical Quantities

Some length scales and critical quantities are important for the understanding of the theoretical parts in chapter 3 and chapter 4.

The critical temperature T_c: T_c is not very well defined in high T_c materials, due to the broad transition. In a midpoint definition, T_c is the temperature at 50% of the normal resistance. Another definition extrapolates the steepest part of the normal to superconducting transition and defines T_c where this line hits zero resistance. When T_c of different samples is compared usually one understands T_c to be the

temperature at which the resistance becomes unmeasurable. We use the last definition and rather specify ΔT, the difference between T_c and the onset of the transition as a measure of the transition width. A common definition of the transition width ΔT is the range in which ρ drops from 90% to 10% of its value just above the onset. In Ginzburg-Landau theory[6], T_c defines the limit when the Gibbs free energy density of a superconductor becomes equal to that of the normal state.

The *critical current density* J_c: if current densities higher than J_c are applied, superconductivity is quenched (the material is normal conducting). The current density at which an electric field of 0.1 μVcm is observed determines J_c in one particular criterion.

The thermodynamic critical field H_c: the energy density difference between normal and superconducting state in zero field (see e.g.[8]): $H_c^2/8\pi$ defines the thermodynamic critical field H_c. A volume multiplied by this energy density leads to the energy which is necessary to bring this volume from the superconducting into the normal state. The temperature dependence of H_c is given by

$$H_c(T) = H_c(0)\left(1-(T/T_c)^2\right) \qquad (1)$$

The coherence length ξ: it defines the minimum distance between the superconducting electron density n_s being at maximum and zero. The normal core of a vortex line is of diameter 2ξ. The temperature dependence of ξ is given by:

$$\xi(T) = \xi(0)\sqrt{\frac{1+(T/T_c)^2}{1-(T/T_c)^2}} \text{ with } \xi(T) \approx \frac{\xi(0)}{\sqrt{1-(T/T_c)}} \text{ for } T \to T_c \qquad (2)$$

from Ginzburg-Landau theory[6].

The magnetic penetration depth λ: the distance over which a magnetic field falls to 1/e from a normal region into a superconductor. The magnetic field of a vortex line extends over an area with radius λ. The penetration depth has the same temperature dependence as ξ.

The dimensionless ratio $\kappa = \lambda/\xi$: it defines the border line between type II and type I superconductors. The Gibbs free energy at the surface between a superconductor and a normal conductor is positive if $\xi > \sqrt{2}\lambda$. The superconductor then expels the magnetic field (Meissner state) to have the smallest possible interface. For $\xi < \sqrt{2}\lambda$, the surface energy is negative and the magnetic field splits up into many small quantized flux tubes to have maximum surface between magnetic field and superconductor.

The lower critical field H_{c1}: even a type II superconductor completely expels the magnetic field as long as the external applied field stays below H_{c1}. In this state the magnetization $M = -H$ inside the superconductor[9].

The upper critical field H_{c2}: this is the field which quenches superconductivity. Above this field the magnetization $M = 0$ since the magnetic field has fully penetrated.

The flux quantum ϕ_0: one flux line contains exactly one ϕ_0, where[10] $\phi_0 = h/2e = 2.07\times10^{-15}$ T m^2 = 2.07×10^{-7} G cm^2.

The flux line spacing a_0: depends on the external field H and ϕ_0, if a hexagonal flux line lattice is assumed, a_0 is given by:

$$a_0 = \sqrt{2\phi_0/\sqrt{3}\mu_0 H} \quad . \tag{3}$$

The values of most of these quantities for our samples are listed in table 1.2 and table 4.1. A good introduction to Ginzburg-Landau theory is given in Tinkham's book[6] .

1.3 General Properties of High-Temperature Superconductors

Compared to conventional type II superconductors, high T_c copper oxides show many similar features in the superconducting state: paired charge carriers, an indication of energy gaps[11,12], and a jump in heat capacity[10] at $T = T_c$. In the normal region both show a metallic behavior (in the sense of having a Fermi surface).

There are many new features. High T_c materials have an antiferromagnetic, insulating parent and have to be doped to conduct. The dopants make planes in the material metallic, which explains the observed anisotropy: all the new materials show different conductance along and perpendicular to these planes. The critical fields and the coherence lengths show this anisotropic behavior as well. In the normal region a linear behavior of resistance with temperature is observed. The feature occurs in some other layered conductors like $ZrTe_3$[4] , but $Nd_{2-x}Ce_xCuO_{4-\delta}$ is an exception in the copper oxides, showing a quadratic behavior. $Y_1Ba_2Cu_3O_{6+x}$ shows a "fan"-shaped broadening of the transition in an applied magnetic field, while $Nd_{2-x}Ce_xCuO_{4-\delta}$ has a slightly broadened and shifted transition similar to conventional superconductors. There are many other new features of high T_c materials, but we restrict ourselves to the effects important for understanding the transport measurements for these materials.

1.4 Structure and Charge Carriers

The structure of $Nd_{2-x}Ce_xCuO_{4-\delta}$ is simple: neodymium layers alternate, followed by CuO layers and oxygen layers. The CuO planes are equally spaced. The copper is bound to four oxygen atoms (T' structure). Tetravalent cerium substitutes for the trivalent neodymium. It is not clear if the dopants are randomly distributed or an ordering exists[14]. Nd_2CuO_4 by itself is insulating and antiferromagnetic and upon doping with cerium it becomes an n-type metal. In the narrow range $0.14<x<0.17$, the material is superconducting, and has a metallic phase for $x>0.17$. Superconductivity peaks at $x=0.15$ ($T_c \approx 24K$), which corresponds to every 13.3 Nd atom being replaced by a cerium atom (there is one cerium atom every 3 1/2 unit cell). One additional condition for the superconducting state has to be met: reduction in the oxygen content. It is hard to measure the exact oxygen content of a compound, but it is believed[15] that $\delta \approx 0.01$. Both the additional electron of Ce^{4+} and the missing oxygen account for the n-type charge carriers. $Y_1Ba_2Cu_3O_{6+x}$ on the other hand, has a more complicated structure. The unit cell contains two different groups of copper atoms: one group is part of a copper oxygen plane surrounded by five oxygen atoms: four in plane oxygen atoms and one apical oxygen along the c-axis (T* structure). The other group has only four nearest-neighbor oxygens: two atoms in each of the c- and b-directions. They are part of the so called copper-oxygen chains, which run along the b-axis. In the beginning of high T_c superconductivity it was believed that the chains were a necessary condition for superconductivity; they are an additional charge reservoir for the CuO planes. In $Y_1Ba_2Cu_3O_{6+x}$, the excess oxygen accounts for

the p-type doping. The oxygen varies over a much larger range, the oxide is superconducting for $0.2<x<1$. Superconductivity peaks at $x=1$ with $T_c \approx$ 92K.

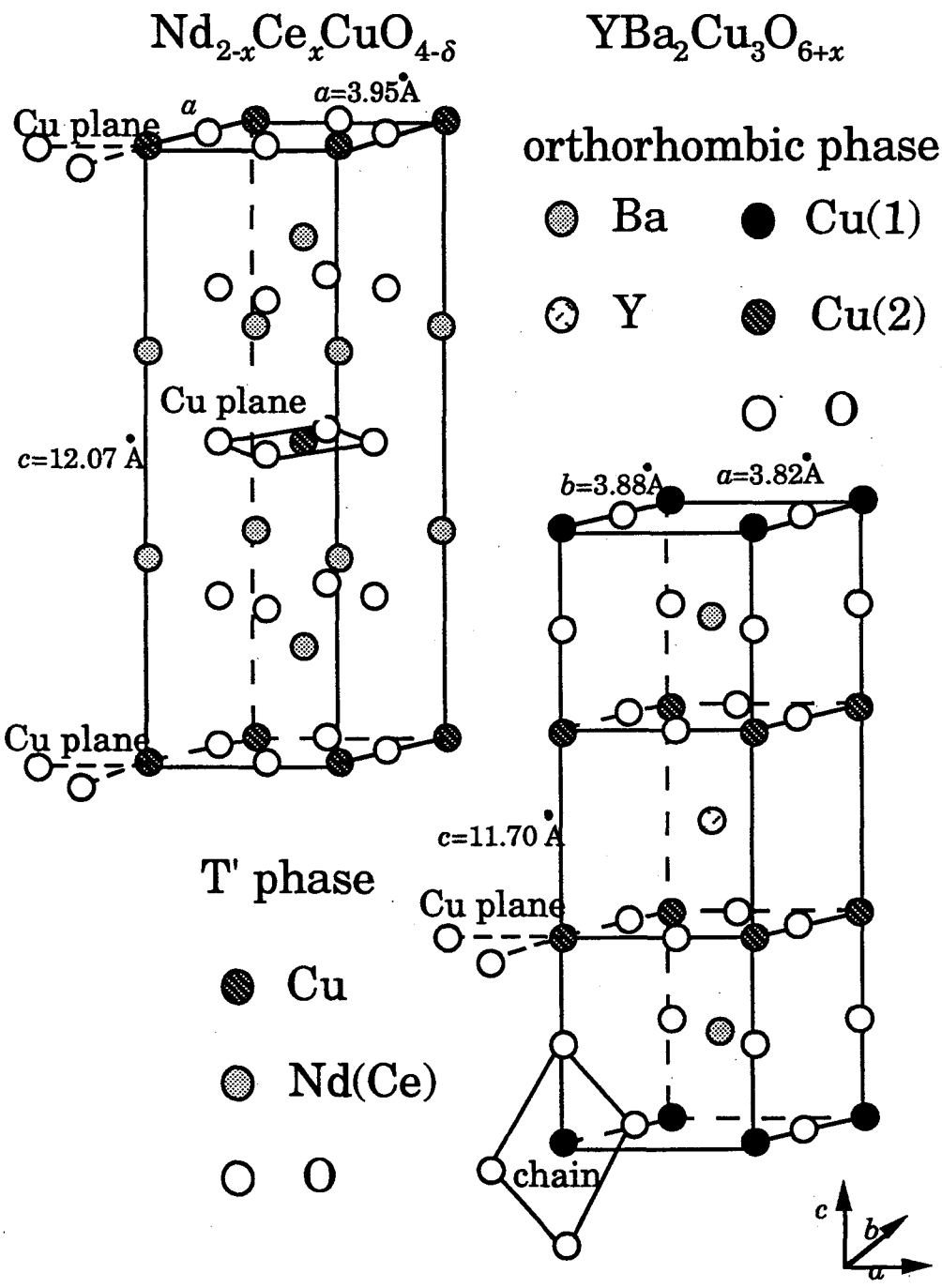

Figure 1.2 Crystal structure of $Nd_{2-x}Ce_xCuO_{4-\delta}$ (left) and $Y_1Ba_2Cu_3O_{6+x}$ (right).

1.5 Production and Quality of the Specimens

The superconducting films were produced by thermal coevaporation at the Technische Universität München, by the group of Prof. H. Kinder. Dr. J. Tate[16] provided the $Nd_{2-x}Ce_xCuO_{4-\delta}$ and Dr. P. Berberich[17] the $Y_1Ba_2Cu_3O_{6+x}$ samples investigated in this thesis. The co-evaporation method is briefly described here. The three metals were evaporated from metal boats (tungsten for Cu, tantalum for the other metals) in an oxygen atmosphere of about 8×10^{-3} mbar. The deposition rates were regulated by quartz monitors, and the stoichiometry was determined by the relative evaporation rates. The films were deposited onto heated substrates (about 650 - 700°C). At this temperature, the films are oriented with the c-axis perpendicular to the substrate (MgO in the case of $Y_1Ba_2Cu_3O_{6+x}$ and $SrTiO_3$ in the case of $Nd_{2-x}Ce_xCuO_{4-\delta}$). After the deposition, the $Y_1Ba_2Cu_3O_{6+x}$ films were cooled to room temperature in 1 torr of oxygen, and the $Nd_{2-x}Ce_xCuO_{4-\delta}$ films were cooled in vacuum. The films were usually between 500 and 3000Å thick and about 7 mm on a side.

The stoichiometry was determined by J. Roberts and R. Nielson at OSU using electron microprobe wavelength dispersive analysis. A $Y_1Ba_2Cu_3O_{6+x}$ thin film standard was used whose stoichiometry had been determined to 1% by Rutherford backscattering spectroscopy (RBS) by L. C. McIntyre, Jr. at the University of Arizona. For the two $Y_1Ba_2Cu_3O_{6+x}$ samples studied, the Cu : Ba : Y ratio were 3 : 2 : 1. The $Nd_{2-x}Ce_xCuO_{4-\delta}$ sample showed Cu : Nd : Ce = 1 : 1.95 : 0.15. From RBS Cu : Nd + Ce was determined, because the Nd and Ce peak cannot be resolved, and microprobe determined Nd : Ce.

The X-ray diffraction pattern showed strong 00ℓ peaks for $Y_1Ba_2Cu_3O_{6+x}$ and little evidence of any other phase or orientation. For $Nd_{2-x}Ce_xCuO_{4-\delta}$ the 002, 004, 006, 008 and 00<u>10</u> peaks were evident as expected, and also smaller peaks which were consistent with 110 and 220 reflections. The surfaces were examined by scanning electron microscopy (SEM). The $Y_1Ba_2Cu_3O_{6+x}$ surfaces are rather featureless, while the $Nd_{2-x}Ce_xCuO_{4-\delta}$ surfaces show a grid of small, Cu-rich grains spaced by about 1 μm. The diffraction patterns for $Y_1Ba_2Cu_3O_{6+x}$ are collected in Appendix A.

	$Nd_{2-x}Ce_xCuO_{4-\delta}$	$Y_1Ba_2Cu_3O_{6+x}$	
	19.08.89	05.08.91	27.08.91
critical temp. T_c	22.4-21.2 K	88.4-90 K	86.2-88 K
$\rho(T_c)$	680 μΩcm	280 μΩcm	420 μΩcm
ρ_{300K}/ρ_{100K}	-	2.8	2.6
J_c at 0.1 μV/cm	1.1×10^4A/cm^2	2.3×10^6A/cm^2	1.7×10^6A/cm^2
substrate	$SrTiO_3$	MgO	MgO
thickness d	300 nm	135 nm	109 nm
bridge width w	50 mm	50 μm	50 μm
bridge length l	3 μm	50 μm	50 μm
contacts	SC -> silver print -> indium -> beryllium copper	SC -> gold layer -> indium -> beryllium copper	

Table 1.1 Material properties of the thin film superconductors. See also table 4.1. J_c is taken in ambient field at 4.2 K for $Nd_{2-x}Ce_xCuO_{4-\delta}$ and 77 K for $Y_1Ba_2Cu_3O_{6+x}$.

The samples have a superconducting transition temperatures around 89 K ($Y_1Ba_2Cu_3O_{6+x}$) and 22K ($Nd_{2-x}Ce_xCuO_{4-\delta}$). The resistivity will be discussed in great detail in subsequent chapters, but here it is

noted that for $Y_1Ba_2Cu_3O_{6+x}$ the resistivity at room temperature is 2223 μΩ cm (sample 27.8.92) and 1082 μΩ cm (sample 5.8.92), and at 490 μΩ cm (sample 27.8.92) at 100 K. For $Nd_{2-x}Ce_xCuO_{4-\delta}$, the resistivities at room temperature and 20 K are 1950 μΩ cm and 650 μΩ cm, respectively. A value for the critical current J_c can be estimated with the 0.1 μV/cm criterion. We obtained 1.1×10^4 A/cm^2 at 4.2 K and ambient field for $Nd_{2-x}Ce_xCuO_{4-\delta}$, and $J_c = 2.3\times10^6$ and 1.7×10^6 A/cm^2 at 77 K for $Y_1Ba_2Cu_3O_{6+x}$. All these material properties are summarized in Table 1.1.

2. Experimental Details

The purpose of the experiment was to map out current-voltage characteristics of $Nd_{2-x}Ce_xCuO_{4-\delta}$, and $Y_1Ba_2Cu_3O_{6+x}$ in temperature and magnetic field space, and determine the resistance with temperature behavior in different applied fields. For this purpose, the films were patterned to define a thin stripe, electrical contacts were applied, and they were cooled to low temperatures in a variable temperature cryostat located in the bore of a superconducting magnet. The dewar and the instruments used are described in section 2.1 Experimental Setup, while 2.2 Data Acquisition focuses on the software and the process of taking data in the system.

2.1 Experimental Setup

The system consists of a Janis 7RD 7"-diameter dewar with a liquid nitrogen jacket. A variable temperature insert supplied by Cryo-Industries allows operation between 4.2 and 300K in the 2" bore of a Cryomagnetics NbTi magnet. All vacuum jackets were at 10^{-5} torr. The system is sketched in figure 2.1. Magnetic fields up to 9 T can be generated by the Cryomagnetics IPS-100 power supply with a homogeneity of 0.1% in a sphere of 1 cm diameter.

The sample is mounted onto a copper disk attached to a long stainless steel rod which allows adjustment of the position of the sample in the magnet. The disk may be positioned in two orientations, so that $\mathbf{H} \parallel \mathbf{c}$ or $\mathbf{H} \perp \mathbf{c}$, with the latter shown in figure 2.2. Embedded in the copper disk are two additional thermometers - a carbon glass 500 and a

platinum resistance thermometer. Cry-Con 78703A grease keeps them in good thermal contact with the sample block. Both the resistances are monitored in four terminal mode and recorded with Tektronix DM5120 multimeters.

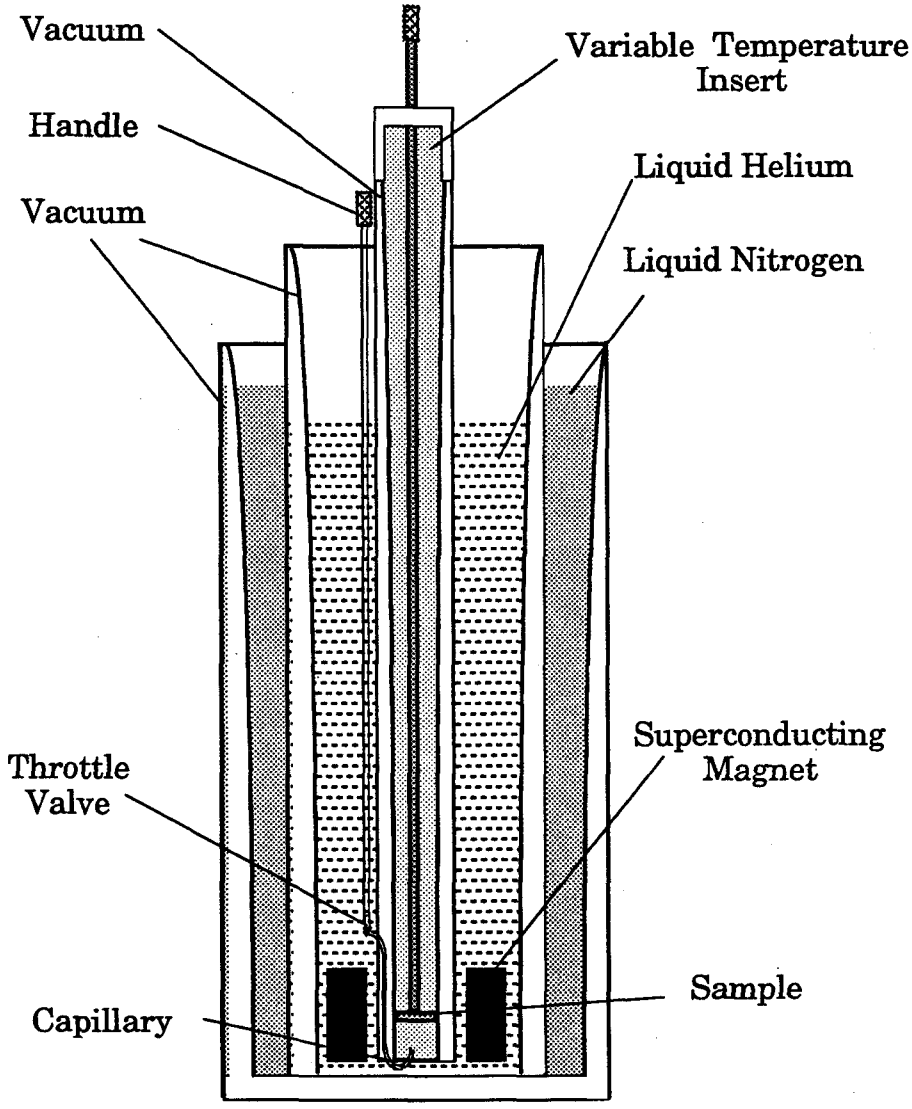

Figure 2.1 Schematic of the dewar with variable temperature insert.

The sample holder (see figure 2.2) was designed with M. Dragowsky to incorporate the following features: lead connection after the mounting, an adapting system that does not require making new contact for changing the orientation and use of beryllium-copper press contacts (beryllium increases elasticity). This sample holder has a large mass of copper, which makes the system slow to respond to temperature changes, but the temperature can be better stabilized for *I-V* curves.

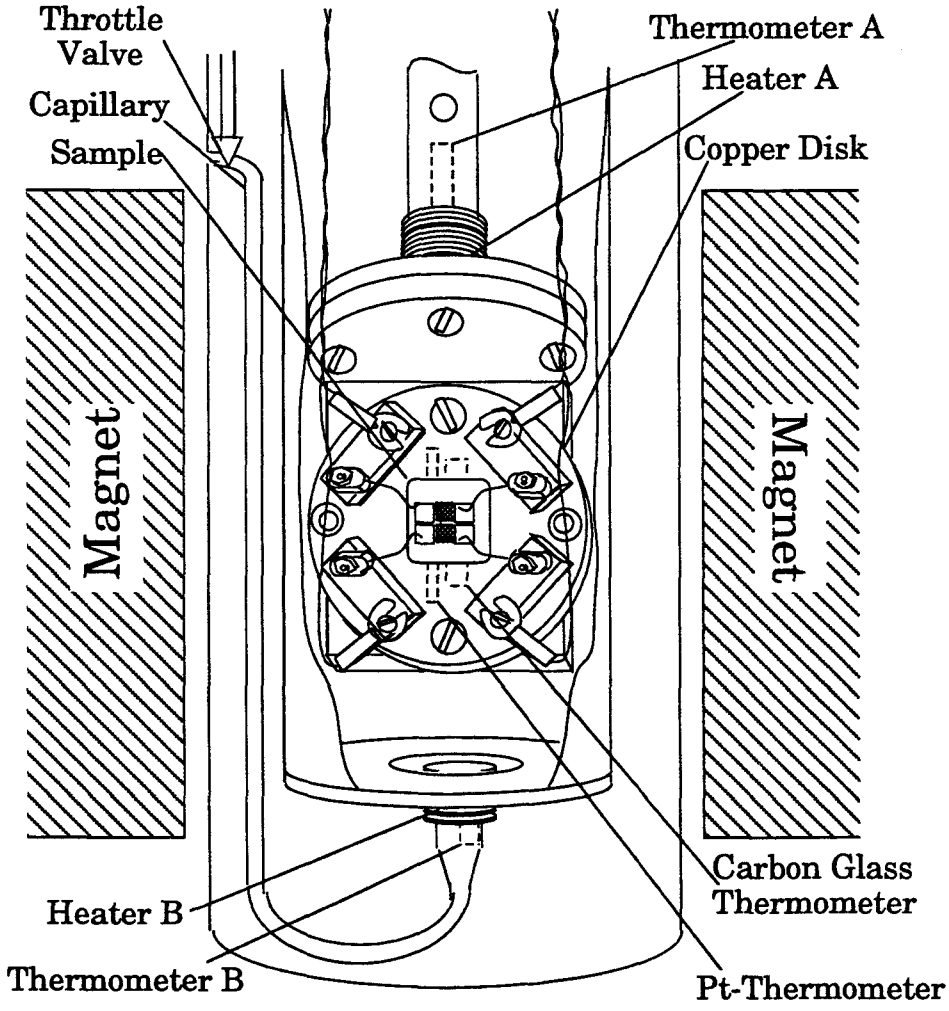

Figure 2.2 Sample holder with location of heaters and thermometers.

The temperature is controlled with a flow of liquid helium through a 1/16-inch diameter capillary regulated by a mechanical throttle valve. A careful cool-down of the system as well as exchange of the sample is very important, in order to not freeze any air, nitrogen or water in the capillary. The liquid helium vaporizes at the bottom of the variable temperature insert and the gas is heated with a 20-Watt heater B. A feedback system, controlled by a Lakeshore model DRC-91CA temperature controller, uses a calibrated carbon glass reference thermometer B to control the heater power and keep T_B close to the setpoint. Another heater A and a calibrated carbon glass thermometer A are located near the sample, and can also be controlled by the Lakeshore controller. The proportional (P or gain), integral (I or reset) and differential (D or rate) settings had to be determined carefully for optimal performance. The correct settings depend on the coolant (liquid nitrogen or helium), geometry of the dewar, the flow rate and the temperature region. They are like a fingerprint of the system. There is a procedure described in the system manual[18], but in practice it is trial and error. For liquid helium $P:I:D = 250 : 5 : 30$ and for liquid nitrogen $200 : 8 : 31$ worked well. The settings depend slightly on the temperature range.

There always exists a gradient between T_A and T_B, the size of which depends on the temperature range. It is especially severe after a big change in setpoint, and can be lowered by giving the system more time to adjust to the new temperature. The superconductor, with its very small mass, responds much faster to temperature changes than any of the thermometers, so a small gradient ensures consistent temperatures. The mean difference between T_A and T_B as well as maximum and

minimum of the gradient are recorded with each set, like a quality seal. Typical cooling rates are 1 K/min and 1.2 K/min for heating in the 70 to 90 K range. Faster cooling or heating causes hysteresis, and the golden rule is to take data only when T_B and T_A are both changing in the same direction.

The sample current is supplied by a Keithley 220 current source. The currents range from 1×10^{-9} A to 100 mA. The accuracy depends on the current range and some examples are listed in table 2.1 a. The sample voltage is measured by a Keithley 182 nanovoltmeter which has both a digital and an analog filter. We could not see any significant improvement by using the analog filter; on the contrary the acquisition time tripled with no apparent improvement in noise. The digital filter is a finite impulse response weighted pole filter. Set on medium or fast, it works with a threshold. If consecutive readings differ by less than 13 ppm (50 ppm in the most sensitive range) of the maximum reading possible in any range, the last reading is averaged with the previous readings. If the reading falls outside of this window, a new average is begun. The size of the window and the number of readings averaged depends on the integration time and filter setting (see table 2.1 b). Changes of order 10 nV cannot be resolved in the presence of a large offset, so the instrument must be properly zeroed.

Our best noise level was 10 nV over 30 min, with the magnet turned off and no other electrical appliances but the instruments being used in the same room. The noise level seemed to increase with applied magnetic field, but there was no significant improvement with the

a.)

applied current	
current	accuracy
100 mA	±150 μA
1 mA	±1.5 μA
10 μA	±15 nA
1 μA	±2 nA
10 nA	±40 pA

b.)

voltage			
threshold		maximum	waiting
range	window	filter	readings
3 mV	±150 nV	off	1
30 mV	±400 nV	fast	30 (21)
300 mV	±4 μV	medium	93 (43)
3 V	±40 μV	slow	370

Table 2.1 a.) Examples of accuracy of applied current (at 18-28°C, for one year). b.) Rang-dependent threshold (left) and number of voltage readings taken, if a reading lies out of window (right). Numbers in brackets for 3 mV range. Note: assumption of analog filter off and integration time 16.6 msec, trigger: one shot on GET.

magnet operating in persistent mode. This may indicate that flux noise is the origin. In order to obtain a noise level of 10 nV in the first place, the system was rewired. A stranded, twisted pair copper wire from Reedex was used outside the system, carefully twisted Belden 8082 polythermalized 32 gauge magnet wire led down to the sample inside. All connections were either crimp connections or solder joints with BiPb (Indalloy 255) solder from Indium Corporation. This special solder has a thermal EMF of only 0.4 μV/K.

The films were patterned to have a defined geometry so that the resistivity could be determined from the resistance. The $Y_1Ba_2Cu_3O_{6+x}$ film was patterned by standard photolithographic methods, while the $Nd_{2-x}Ce_xCuO_{4-\delta}$ film was patterned by laser ablation. The bridges so formed were of order 100 μm wide. The exact dimensions and geometries are found in figure 2.3 and table 1.2. Gold contacts were

evaporated onto the $Y_1Ba_2Cu_3O_{6+x}$ film soon after deposition. Silver print (GC Electronics 22-201) contacts were painted onto the $Nd_{2-x}Ce_xCuO_{4-\delta}$ film after it had been etched in a 10:1 de-ionized water / glacial acetic acid solution for 9 minutes, and rinsed in methanol. The contacts were baked at 150°C for 3 minutes. Small beryllium-copper press contacts coated with indium metal pressed firmly against the contact pads, this allowed a contact area as small as 3x5 mm. The contacts also secured the sample in place.

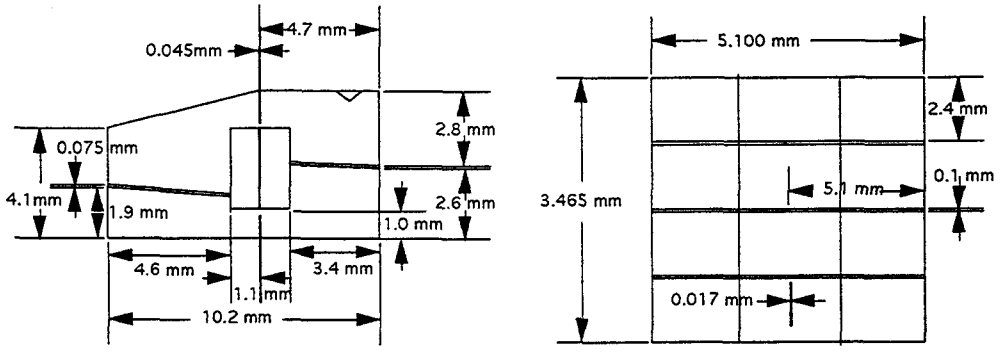

Figure 2.3 Sample pattern for $Nd_{2-x}Ce_xCuO_{4-\delta}$ (left) and $Y_1Ba_2Cu_3O_{6+x}$ (right).

2.2 Data Acquisition

The system operates either in current-voltage mode (I-V) or resistance-temperature mode (R-T). In the former the temperature is held constant and the current scanned, while in the latter the temperature is scanned and current held constant. The magnetic field is always constant. To obtain one data point, a current was applied, the voltage across the superconductor read, and the average temperature of the film recorded. A program written in LabVIEW II (National Instruments) interfaces all instruments except the magnet power supply, to a Macintosh IIci computer by means of an IEEE-488 bus. LabVIEW is picture based and data driven, and as easy to learn as any other language, but programs are structured like a flow charts, so those written by someone else are easier to follow. A particularly nice feature of LabVIEW is the program front panel, which allows the user to change variables in the program by means of instrument-like interface. A picture is shown in figure 2.4. The data were analyzed and presented with the analysis and graphics presentation program Kaleidagraph by Abelbeck software.

Below, the features of the interface are described and the data-taking routine together with the flow chart of the program are discussed. A listing of the complete program is in Appendix C.

Following Page: **Figure 2.4** Front panel of LabVIEW II interface program. It shows all important controls and indicators of the different instruments.

Figure 2.4

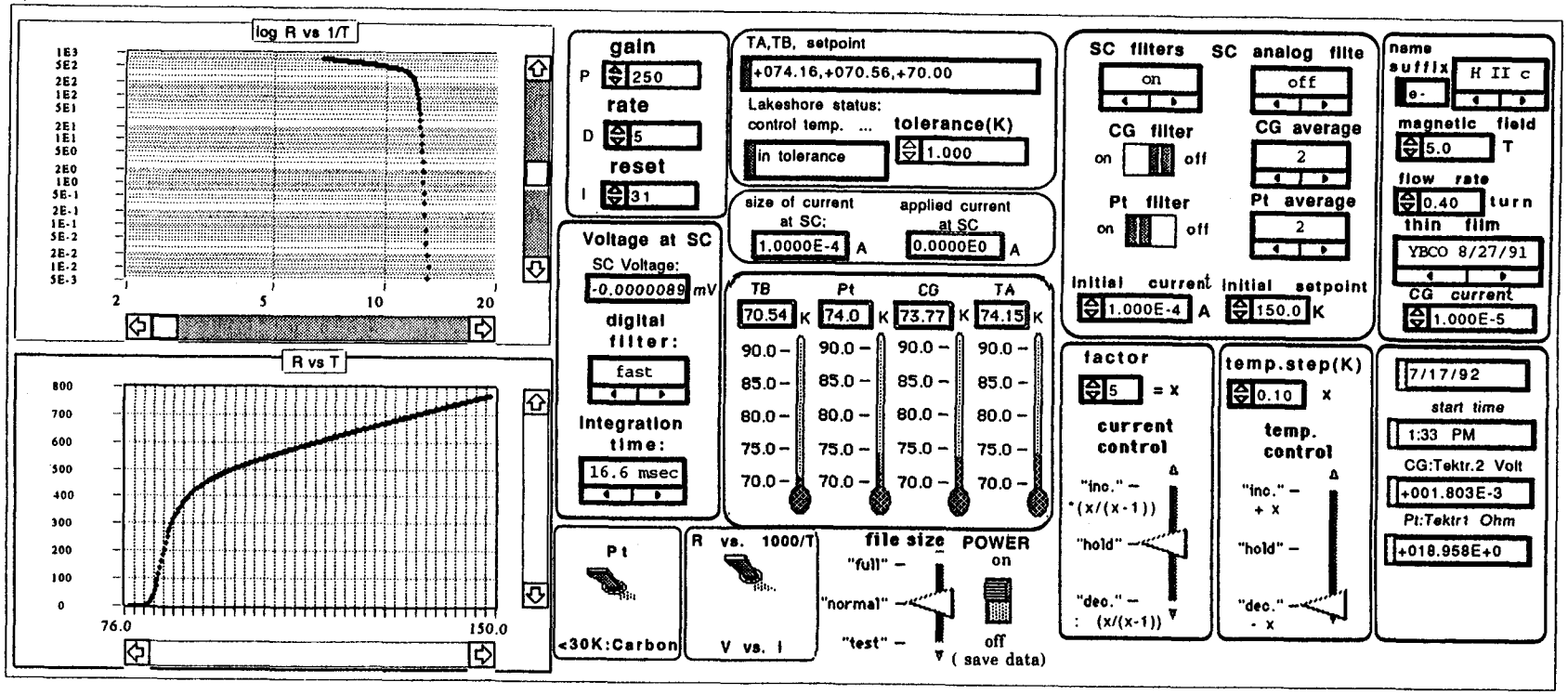
log R vs 1/T
1E3
5E2
2E2
1E2
5E1
2E1
1E1
5E0
2E0
1E0
5E-1
2E-1
1E-1
5E-2
2E-2
1E-2
5E-3
2
5
10
20
R vs T
800
700
600
500
400
300
200
100
0
76.0
150.0
gain
P 250
rate
D 5
reset
I 31
TA,TB, setpoint
+074.16,+070.56,+70.00
Lakeshore status:
control temp. ...
in tolerance
tolerance(K)
1.000
size of current at SC:
1.0000E-4 A
applied current at SC
0.0000E0 A
Voltage at SC
SC Voltage:
-0.0000089 mV
digital filter:
fast
Integration time:
16.6 msec
TB
70.54 K
Pt
74.0 K
CG
73.77 K
TA
74.15 K
90.0
85.0
80.0
75.0
70.0
SC filters
on
SC analog filte
off
CG filter
on off
CG average
2
Pt filter
on off
Pt average
2
initial current
1.000E-4 A
initial setpoint
150.0 K
name
suffix
e-
H II c
magnetic field
5.0 T
flow rate
0.40 turn
thin film
YBCO 8/27/91
CG current
1.000E-5
factor
5 = x
current control
"inc." – *(x/(x-1))
"hold"
"dec." – : (x/(x-1))
temp.step(K)
0.10 x
temp. control
"inc." – + x
"hold"
"dec." – - x
7/17/92
start time
1:33 PM
CG:Tektr.2 Volt
+001.803E-3
Pt:Tektr1 Ohm
+018.958E+0
Pt
<30K:Carbon
R vs. 1000/T
V vs. I
file size
"full"
"normal"
"test"
POWER
on
off
(save data)

The *I-V* and *R-T* modes are technically only different in the plot and in which of temperature or current is kept constant. The program runs in either mode, according to a setting on the program front panel. A switch on the front panel determines whether the Pt-thermometer (above 30K) or the CG-thermometer (below 30K) is recorded. It can be changed at any time.

While data-taking is underway, it is important to see the data in two different plot types at the same time. Either log$V$ versus log$I$ and V versus I are plotted, or log$R$ versus $1/T$ and R versus T. Only both together allow one to estimate when to stop and start taking data.

Both current and temperature set-point (for $T_{B)}$ are controlled with a set-point system in the program: initially a value is set, after a measurement an increase or decrease to a new set-point by a changeable step-size follows. The current is stepped logarithmically, while the temperature is changed linearly, to achieve an equal data point spacing in the different plot types. A measurement cycle commences once the temperature is within ΔT for the setpoint. This tolerance can be changed at any time. Usually, thermometer B and heater B control the temperature in the sample chamber. When heater B broke, for the *I-V* curves of $Nd_{2-x}Ce_xCuO_{4-\delta}$, thermometer A and heater A had to be used.

To correct for all thermal offsets we use a cycle of forward current and then reverse current for one voltage measurement of the superconductor: while I_+ is applied the voltage $V_+ = V_{true} + V_{offset}$ is recorded, then while I_- is applied $V_- = -V_{true} + V_{offset}$ is measured. The corrected voltage is $V = (V_+ - V_-) / 2 = V_{true}$. While the temperature is

controlled and measured, zero current is applied to the superconductor to avoid any heating.

The Keithley nanovoltmeter receives a trigger from the computer (one shot on GET mode), after the current is applied. After a delay time

Panel icon ...	controls ...	with typical settings ...		
throttle valve	coolant flow	cooling 1/2 to 1 turn		heating 1/4 to zero turn
Keithley 182 voltage at super-conductor	voltage averaging	digital filter on		analog filter off
		integration time 16.6 msec		filter fast or medium
LakeShore temperature controller	heater power in LHe in LN	*P* (gain)	*I* (reset)	*D* (rate)
		250	5	30
		200	8	31
program toggle switch	mode: *I-V* or *R-T*	temperature control		current control
		hold		increase or decrease
		increase or decrease		hold
program: curr. contr. temp. contr.	stepping: $\times$ or / (x/(x-1)) $\pm x$	fast scan		thorough scan
		x=2 to 5		x=10 to 20
		x=1 to 1.5 K		x=0.1 to 0.5 K
program toggle switch	thermometer selection	Pt for temperature > 30 K CG for temperature < 30 K		
Tektronix I Pt-therm.	resistance averaging	filter on		average 3
Tektronix II CG-therm.	voltage averaging	filter on		average 3
Lakeshore curr.source	CG-therm. current	10 mA current and apply current (value needed for front panel)		

Table 2.2 Typical program settings for data acquisition.

of 300 msec it begins to process readings. This allows the current to settle and any transients to die away.

Once all readings are taken, the program calculates several derived quantities and tabulates them along with the raw data. The columns are labeled and the geometry independent quantities (ρ, E, J) are calculated and appended to the table. This features takes only a couple seconds in the program and saves us hours of analysis later. Two forms are possible: the *test form* records $V, I, \rho, 1/T, T_{pt}, T_{cg}, T_A$ and T_B in R-T mode or $V, I, E, J, T_{pt}, \ldots$ in the I-V mode. The *normal form* is smaller, recording $V, I, \ln\rho, 1/T, \rho, T$ in the R-T mode and V, I, E, J, ρ, T in the I - V mode. In addition to the table, an information panel records the date, time of run, start time, all filter settings, a temperature gradient statistic, and all units and conversion factors. It also contains information about the magnetic field, sample, and flow rate, which had been entered on the front panel.

The interfacing program initializes all instruments, then sets them to the appropriate values. Typical setting are listed in table 2.2. To obtain one data point the following routine is executed. The nanovoltmeter filters and the *PID* parameters are set. When the temperature is within a chosen tolerance of the set-point, all thermometers are read. Then the current cycle for the voltage measurement is executed. The thermometers are read again and the average temperature recorded. The plot is updated with the new data point. Then the new current or temperature setpoint is changed and the process starts from the beginning. Finally, a data set is tabulated in test or normal form and the information section is attached.

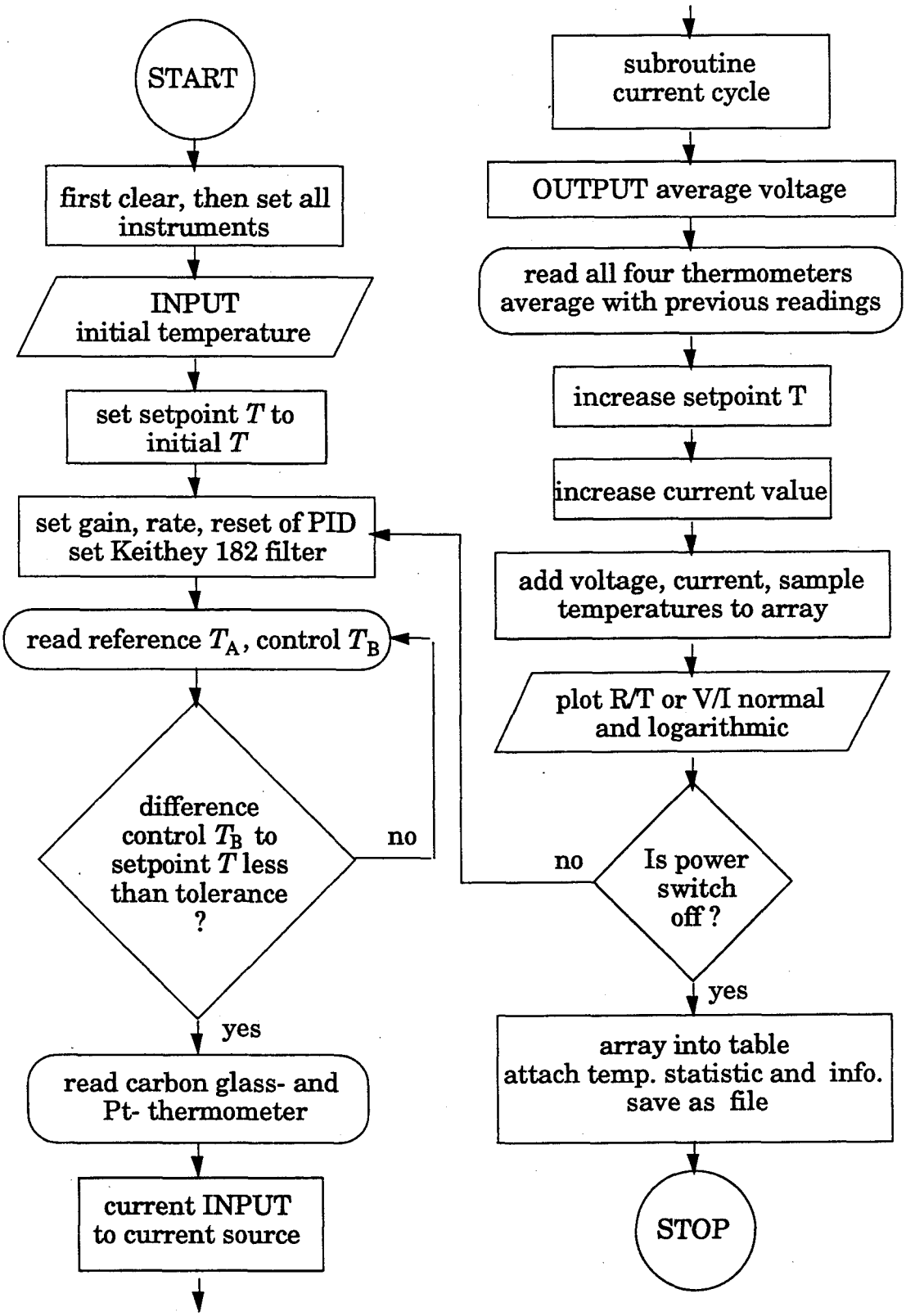

Figure 2.5 Flowchart of interface.

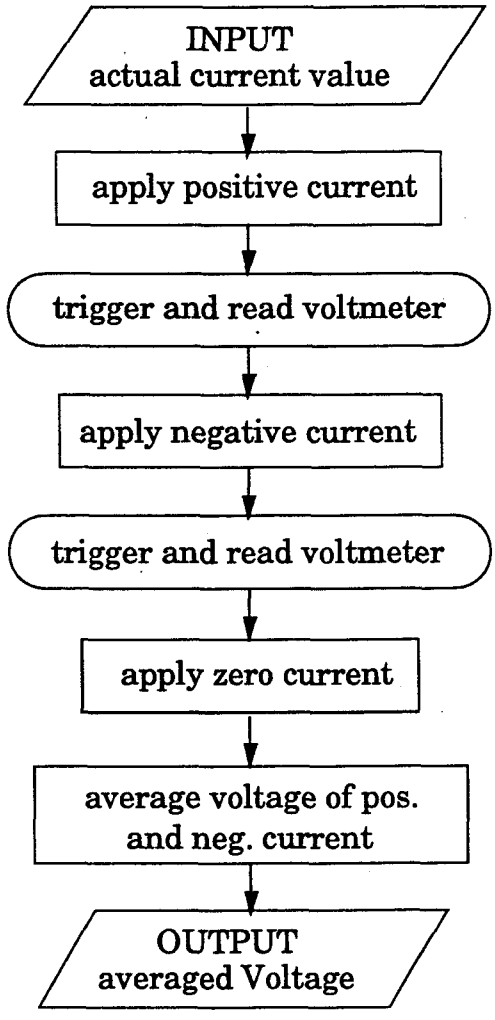

Figure 2.6 Subroutine flowchart of interface.

3. Current - Voltage Characteristics

Even though many researchers work in high temperature superconductivity, a clear picture of vortex motion is only beginning to emerge. How do flux lines arrange and move around? Do they bend or stay stiff, and to what extent is the motion correlated in the field direction? One could say: if you don't know, then look. Decoration experiments have confirmed a flux array at low temperatures already for conventional type II superconductors[19]. However imaging methods give only surface pictures. The surface of high T_c superconductors, though, has different material properties than inside, mainly because of oxygen diffusion. Most imaging methods are possible only at very low temperature, where the flux lattice is not yet thermally activated, but the resistance in this region is well below the resolution of ordinary instruments. Recent measurements on $Y_1Ba_2Cu_3O_{6+x}$ with small SQUID's[20] (superconducting devices which can detect tiny changes in the local magnetic field) have revealed that signals from flux lines on the top of a superconductor may not coincide with signals obtained directly below at the bottom of the superconductor. This suggests flexible flux lines. Optical methods[21] have imaged flux lines entering and leaving superconductor surfaces. A scanning electron tunneling microscope image[22,23] has shown the conductance is increased in the middle of a flux line. These measurements are also limited to low temperatures, because a static flux lattice is necessary to obtain a high resolution picture.

The other choice is to make theoretical models, which predict some kind of transport behavior and see if the experimental data support it. There have been different models presented to explain the broadening of the resistance transition in high T_c superconductors.

Close to T_c *fluctuations* are predicted[24-27] and experimentally verified[28,29]: above T_c the resistance is suppressed, because some electrons pair and become superconducting. Below T_c, it is increased, because some pairs break up and become normal conducting. The fluctuation effects are big because of the much smaller coherence length in cuprates than in conventional superconductors, and because thermal energies at the transition are higher.

Flux motion due to a Lorentz force driven flux lattice is predicted to describe a wide range of the transition. From the applied current flux lines experience a Lorentz force $\mathbf{F} \propto \mathbf{J} \times \mathbf{B}$. They start to move and cause an electric field $\mathbf{E} \propto \mathbf{v} \times \mathbf{B}$, which is parallel to J. The flux lines will not move completely freely, because a viscous drag force will impede their motion. The characteristic of this *flux flow model* is an ohmic behavior: a higher applied current leads to a linear increase in flux motion and therefore higher resistance. For details on flux flow see e.g. Tinkham[6] or Kim *et al.*[30]. In the presence of strong pinning, the flux lines can be thermally activated across the potential barrier and creep to the next pinning location. The dynamics of this process can be described by an logarithmic decay in time[6] , which has been experimentally proven (see e.g. [31]). This model has two limits: for low temperatures a linear behavior between E and J is predicted. Since it shares this quality with the flux flow model it is confusingly called *thermally assisted flux flow*

(TAFF). For high temperatures a more complicated relationship between E and J is predicted. This limit is called *flux creep*. The consequences of the flux motion models (flux flow, TAFF and flux creep) for the current-voltage characteristics are discussed extensively in the next section on thermally activated depinning.

The *vortex glass* proposed by *Fisher et al.*[32,33] directs its attention to a scaling behavior which is observed in some of the cuprates e.g.[34,35]. Like a spin glass, the flux lines are not mobile in this phase, but are frozen in a pattern matching the local defect structure and undergo a true thermodynamic transition at $T = T_g$. A short discussion on this will follow in the next section. A review of the models discussed so far with focus on vortex glass is given in [36].

For two dimensional superconductivity, the *Kosterlitz-Thouless*[37] model may apply; vortex-antivortex pairs have a finite binding energy there, above a certain temperature free vortices are created thermally and move across with the applied current.

Halbritter's[38] model of weak links assumes that insulating planes force the current to meander through the superconductor. The effective resistivity is a superposition of resistance caused by "inter-" and "intra-" grain boundaries.

An early theory, proposed by *Müller et al.*[39], models the oxides being coherent only in small domains interconnected by Josephson-junctions, where flux motion along these junctions causes a phase slip of the order parameter and finite resistance.

A phenomenological superconducting-normal-superconducting (SNS) junction model[40] suggests planar normal defects, which behave

like SNS weak links in a magnetic field, there the critical current through the links is exponentially suppressed by the applied field in a low field limit.

Some of the models discussed above depend on the Lorentz force. These are the flux motion models, the model of Müller *et al.* and the Kosterlitz-Thouless model. For them the resistance depends on the configuration of current to applied field, so an excess resistivity can be defined as the difference between ρ for $\mathbf{J} \parallel \mathbf{H}$ and $\mathbf{J} \perp \mathbf{H}$. Kwok *et al.*[41] give experimental evidence on single crystal $Y_1Ba_2Cu_3O_{6+x}$ that the excess resistivity follows a $\sin^2$-dependence with the angle between current and magnetic field. Some groups could not find such an angular dependence for single crystal $(La,Sr)_2CuO_4$[42], thin film $Bi_2Sr_2Ca_2O_{8+y}$[43] and $Tl_2Ba_2CaCu_2O_x$[44]. Ivley and Kopnin[45] have made an attempt to explain such angular independent dissipation: for $\mathbf{H} \perp \mathbf{c}$ and $\mathbf{J} \parallel \mathbf{H}$ some flux lines cross the CuO planes and form vortex kinks, which are perpendicular to the field and can be thermally activated and start moving.

From the limitations of imaging methods, it is clear that either verification or contradiction of these models has an important place in putting the puzzle pieces together to find out what is causing resistance in high T_c superconductors. This work will look mainly into the flux motion models and into Fisher's vortex glass.

3.1 Theory of Thermally Activated Depinning

A type-II superconductor in an applied field is generally not in thermal equilibrium, because the flux lines are pinned[46]. After a change

in the external applied field $\mathbf{H_a}$, flux lines enter or exit the specimen. The internal field $\mathbf{B}(r)$ exhibits a gradient, which generally does not exceed a critical value. Therefore the following relation holds everywhere in the specimen:

$$|\nabla \times \mathbf{B}| \approx |\nabla |\mathbf{B}|| \leq \mu_0 J_c \tag{4}$$

At temperatures above zero, thermal motion may allow some of the flux lines to overcome the pinning potential. The flux-density gradient and the current density will then gradually decrease by thermally activated depinning. This slow decrease of trapped flux is observed only close to T_c in classical superconductors. Due to smaller pinning energies and higher temperatures, flux creep is observed in a much larger temperature interval in high-T_c superconductors. This behavior is generally modelled according to Anderson's idea[47] picturing the vortices as particles in a tilted potential well, see figure 3.1.

The attempt frequency ν to overcome the barrier is given by

$$\nu = \nu_0 \exp(-U / k_B T), \tag{5}$$

where U is the height of the potential well, k_B the Boltzmann constant. If pinning is absent (U=0), the attempt frequency ν_0 may be interpreted as a typical frequency of thermal fluctuations of an ideal vortex lattice[48]:

$$\nu_0 = \frac{\rho_n}{2\pi\lambda^2} \frac{H}{H_{c2}} \left(1 - \frac{H}{H_{c2}}\right). \tag{6}$$

If a current is applied, the activated jumps of a flux line or a flux line bundle with and against the Lorentz force can be described with jump rates ν_+ and ν_- for forward and backward jumps respectively. The drift velocity of the vortices is then given by $v = \nu \delta l$, where δl is the jump

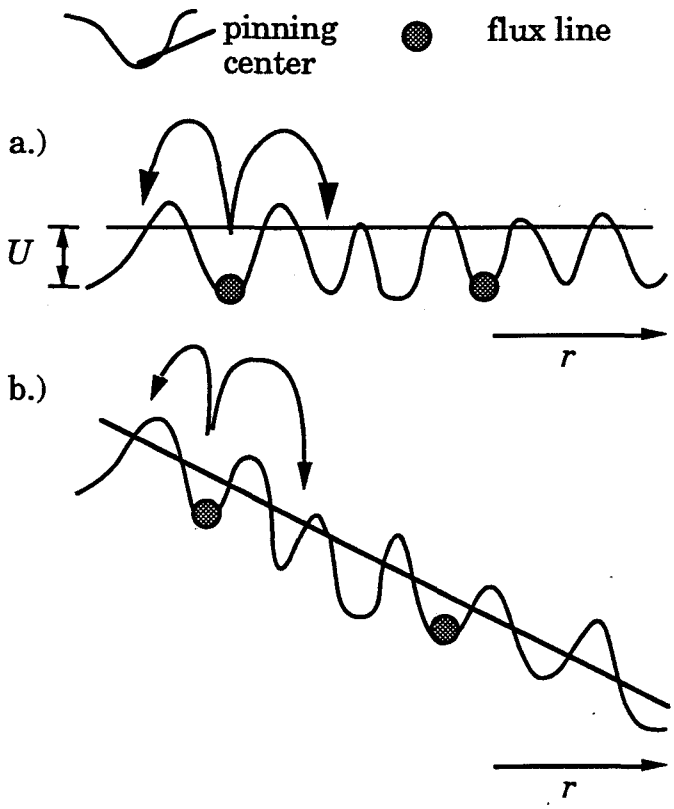

Figure 3.1 Pinning Potential in Anderson's model. Potential well a.) *without*, and b.) *with* transport current applied.

distance, and the electric field $E = \mu_0 H v$. This leads to:

$$E(J,H,T) = (\nu_+ - \nu_-)\delta l \mu_0 H \equiv \rho J \qquad (7)$$

For forward (backward) jumps the activation energy U in (5) is lowered (increased) by $\delta W = J\mu_0 H \delta V \delta l$, the work done by a vortex of volume δV jumping a distance δl, thus

$$E = \delta l \mu_0 H\left(\nu_0 \exp\left(-(U-\delta W)/k_B T\right) - \nu_0 \exp\left(-(U+\delta W)/k_B T\right)\right). \qquad (8)$$

One can introduce the parameters $J_{c0}(H) = U/\mu_0 H \delta V \delta l$ (critical current density, when $U = W$) and $\rho_{c0}(H)$ (resistivity at $J = J_{c0}$ and small T),

approximated from:

$$\rho_c = \frac{\mu_0 H \delta l}{J_{co}} \nu\Big|_{J=J_{co}} = \frac{\mu_0 H \delta l}{J_{co}} \nu_0 \left(1 - \exp\left(-2 J_{co} \mu_0 H \delta V \delta l / k_B T\right)\right) . \quad (9)$$

With $\exp(-2J_{co}\mu_0 H \delta V \delta l/k_B T) << 1$ for small T, $\rho_{co}(H) = \mu_0 H \delta l \nu_0 / J_{co}$. Using J_{co} one can rewrite $\delta W = UJ/J_{co}$. This all leads to the current, temperature and field dependence of the electric field:

$$E(J) = 2\rho_{co} J_{co} \exp\left(-U / k_B T\right) \sinh\left(JU / J_{co} k_B T\right) . \quad (10)$$

In the following discussion *U is always large compared to $k_B T$*, otherwise the thermal energy alone would be larger than the potential well, and the latter loses its purpose. With the limits at small current densities $J << J_1 = J_{co}\, k_B T/U$ one can approximate the $\sinh(x)$ for small arguments with a linear relation. This leads to an ohmic regime of thermally assisted flux flow (TAFF). At larger currents $J \approx J_{co}$, $E(J)$ becomes nonlinear (flux creep regime):

$$E = \left(2J\rho_{co} U / k_B T\right) \exp\left(-U / k_B T\right) = J\rho_{TAFF} \qquad \text{for } J << J_1 \quad (11)$$

$$E = \rho_{co} J_{co} \exp\left(\left(J / J_{co} - 1\right) U / k_B T\right) \qquad \text{for } J \gtrsim J_{co} . \quad (12)$$

For $J >> J_{co}$ one ends up in the flux flow ohmic regime[6]:

$$E \approx J\rho_{FF} \left(1 - J_{co}^2 / J^2\right)^{1/2} \approx J\rho_{FF} \qquad \text{for } J >> J_{co} . \quad (13)$$

At lower T and lower H different nonlinear regime, the vortex glass state, is predicted to scale as[32] :

$$E = J \exp\left(-\left(J_2 / J\right)^{\alpha}\right) \qquad \text{low } T, \text{ low } B. \quad (14)$$

The regions where the different theories apply were mapped out by Brandt[49]: see figure 3.2.

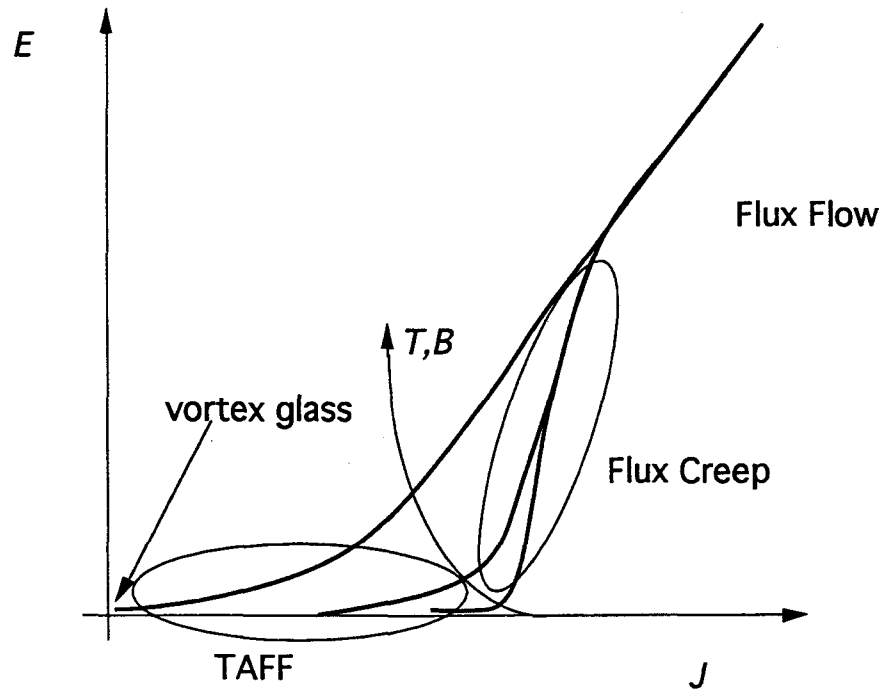

Figure 3.2 Theoretical current-voltage characteristics for various temperatures and applied fields, schematic after Brandt[49]. The areas where the different models apply are indicated.

3.2 Analysis of Data

So far, we have mostly looked at $Y_1Ba_2Cu_3O_{6+x}$ (sample 27.08.91) current-voltage characteristics, where we either kept a constant field and varied the temperature (see figure 3.3) or stayed at a constant temperature and varied the magnetic field (see figure 3.5).

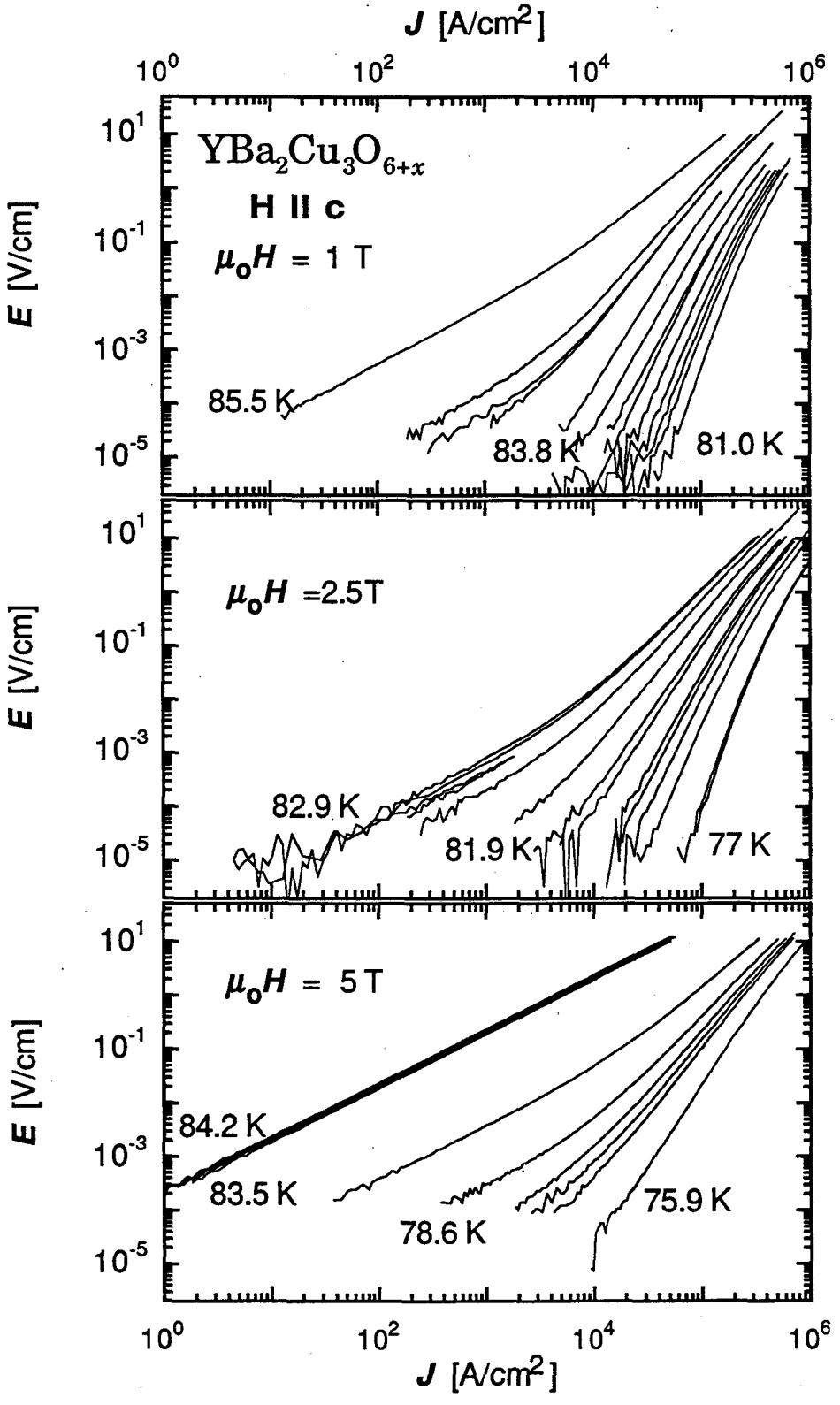

Figure 3.3 Electric field versus current density for $Y_1Ba_2Cu_3O_{6+x}$ for applied fields 1 T, 2.5 T and 5 T.

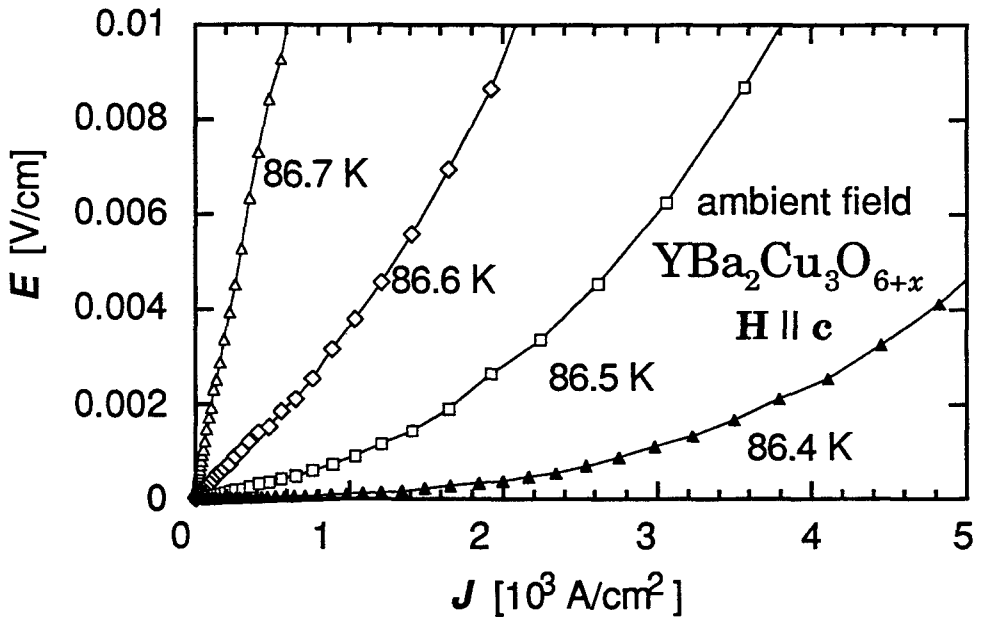

Figure 3.4 Linear plot of E versus J in *ambient field* for $Y_1Ba_2Cu_3O_{6+x}$. Linear TAFF for low E and J and a turnover into flux creep is visible.

For both cases the data can in principle be divided into three regions. Starting at high temperatures and high fields the electric field varies linearly with the current density. We will take a closer look at this region in chapter 4.1. This is shown in figure 3.3 for 5 T applied field. We did not go high enough to obtain this linear region for 2.5 T and 1 T. However we obtained such curves for a wide range of fields on the sample 5.8.91 of $Y_1Ba_2Cu_3O_{6+x}$.

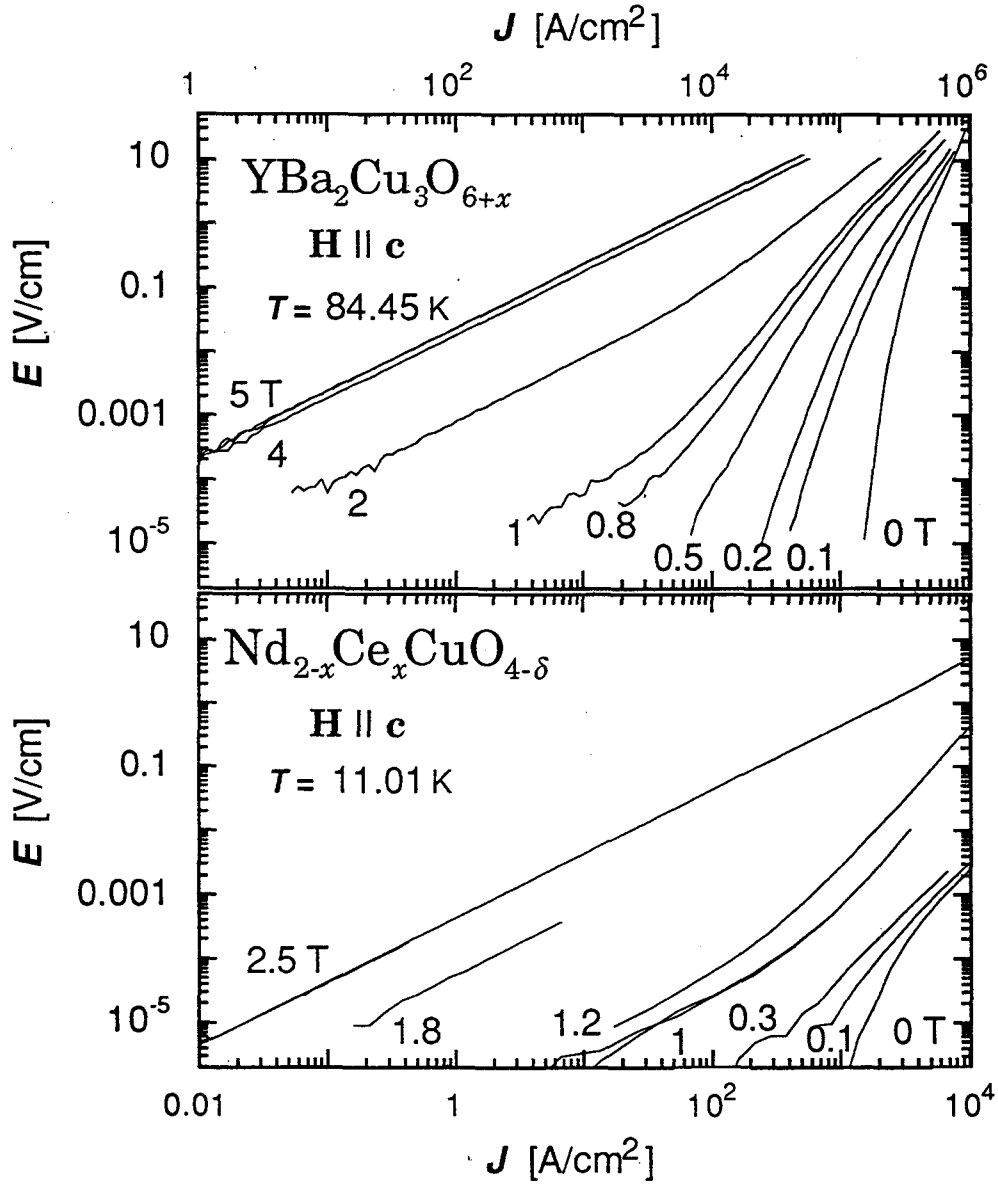

Figure 3.5 Log$E$ versus log$J$ at constant temperature for varying fields. Top: $Nd_{2-x}Ce_xCuO_{4-\delta}$ top, and bottom: $Y_1Ba_2Cu_3O_{6+x}$.

At slightly lower temperatures or fields, the curves are linear at the low current density, as predicted by the TAFF model. At higher current density, there is an much steeper increase of E with J, indicating a crossover into the creep regime. At the highest current densities, the increase becomes less rapid again. For clarity this region is blown up

and shown in a linear plot in figure 3.4 for $Y_1Ba_2Cu_3O_{6+x}$ in ambient field. The data points are thin due to the logarithmic spacing. For low currents the curves show a true linear relation between E and J. Then a smooth crossover to an upwardly bending curve with constantly increasing slope can be observed. For even lower temperatures (as shown in figure 3.4) the linear region disappears and the curves show an upward bend even for very small currents.

At the lowest temperatures and applied fields, there is a downturn in the log$E$-log$J$ plot. The electric-field drops exponentially in this region with decreasing applied current. It is not clear if the linear relation between E and J (see figure 3.3), into which the steep vortex glass curves, as well as the S-shaped curves turn over for higher currents, are due to flux flow.

We verified Brandt's theoretical predictions for the TAFF and flux creep model; however we observed the vortex glass at lower temperatures and not below the TAFF region, as indicted in figure 3.2.

Figure 3.3 shows that the crossover to vortex glass shifts to higher currents and lower temperatures with increasing applied field. The crossover can be observed around 84K for applied field = 1 T, 81.5K for 2.5 T and it is below 75.9K for 5 T. In figure 3.5 the temperature is constant and the applied field varies. Here a crossover can be observed for $Y_1Ba_2Cu_3O_{6+x}$ (top) between 0.5 T and 0.8 T and $Nd_{2-x}Ce_xCuO_{4-\delta}$ (bottom) between 0.3 T and 1 T. Not shown are the crossovers for $Y_1Ba_2Cu_3O_{6+x}$ for 80 K around 3 T and for 75 K around 5 T. For $Nd_{2-x}Ce_xCuO_{4-\delta}$ we observed the crossover at 7 K between 0.7 and 1.5 T and at 4.2 K between 1 and 3.5 T.

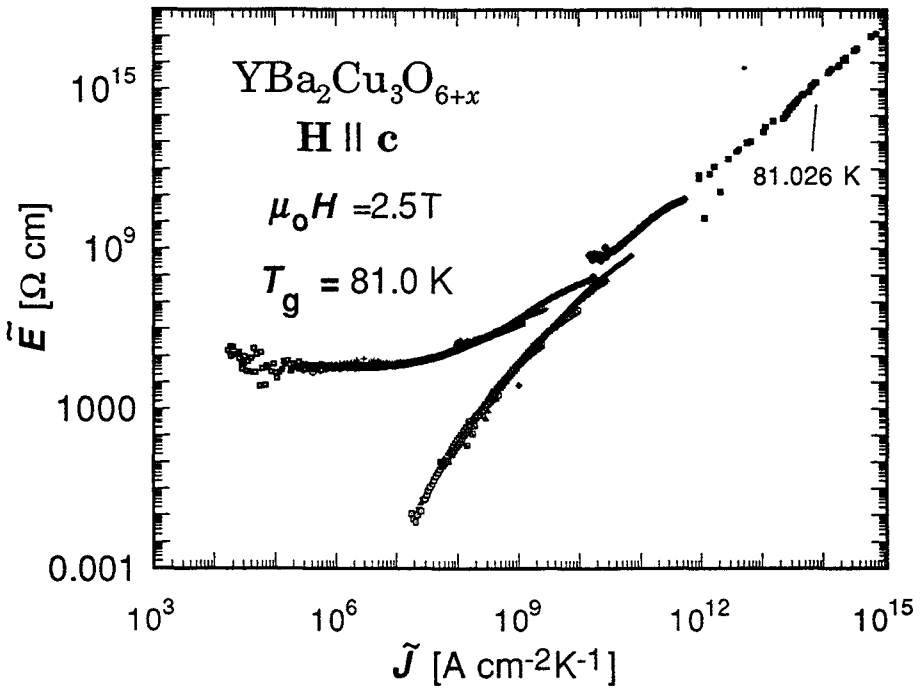

Figure 3.6 Scaling around T_g = 81.0 K for $Y_1Ba_2Cu_3O_{6+x}$ in 2.5 T applied field.

If a true thermodynamic transition occurs, critical exponents describe the behavior of the important length scales and quantities. The coherence length ξ diverges near T_g with exponent ν: $\xi \propto |1\text{-}T/T_g|^{-\nu}$. By plotting the scaled functions[50]

$$\tilde{E} = \frac{E}{J}\left(1-\frac{T}{T_g}\right)^{\nu(d-2-z)} \quad \text{versus} \quad \tilde{J} = \frac{J}{T}\left(1-\frac{T}{T_g}\right)^{\nu(1-d)}, \qquad (15)$$

with z dynamic exponent and d dimension, all data fell on two curves, one with an upward turn reflecting the S-shaped data and one with downward turn reflecting the glassy behavior[51]. We obtained ν = 1.65, z = 4.95 and d = 3. These values match the values obtained by Koch *et*

al.[34] for thin film $Y_1Ba_2Cu_3O_{6+x}$, however not Yeh's *et al.*[50] values for a single crystal.

The scaling is shown for $I-V$ curves in an applied field of 2.5 T in figure 3.6. The dependence of the glass temperatures with the magnetic field is shown in figure 3.7. $T_g(H)$ lies almost on a straight line starting at 86 K with slope -2 K/T.

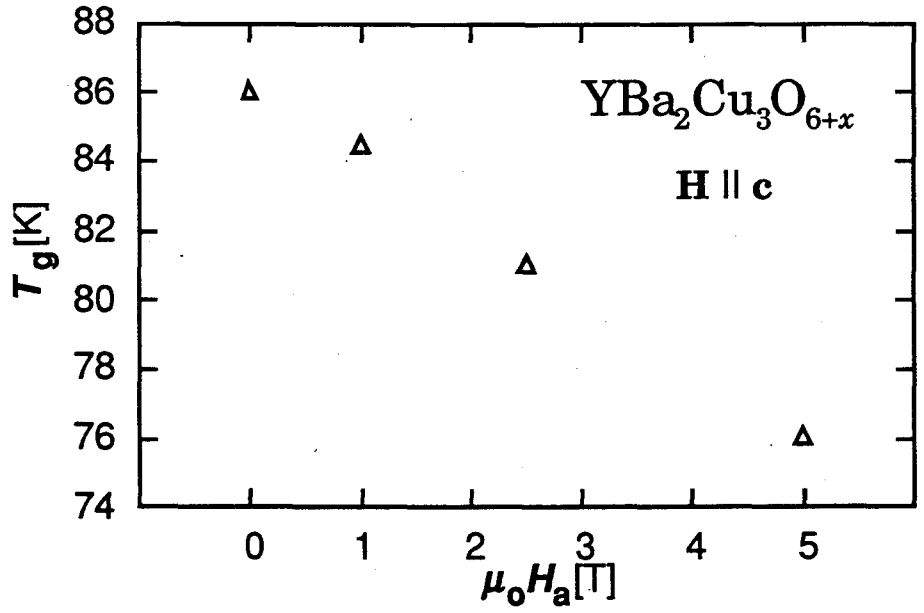

Figure 3.7 Field dependence of T_g for $Y_1Ba_2Cu_3O_{6+x}$.

4. Resistance with Temperature Behavior

The resistive transition of the two superconductors we examined showed very different behaviors: the transition shifts and slightly broadens with increasing field for $Nd_{2-x}Ce_xCuO_{4-\delta}$ and broadens and fans for $Y_1Ba_2Cu_3O_{6+x}$. This is very clear from figure 4.2. While the behavior of $Nd_{2-x}Ce_xCuO_{4-\delta}$ comes close to conventional type II superconductors, that of $Y_1Ba_2Cu_3O_{6+x}$ is common to most of the high T_c materials.

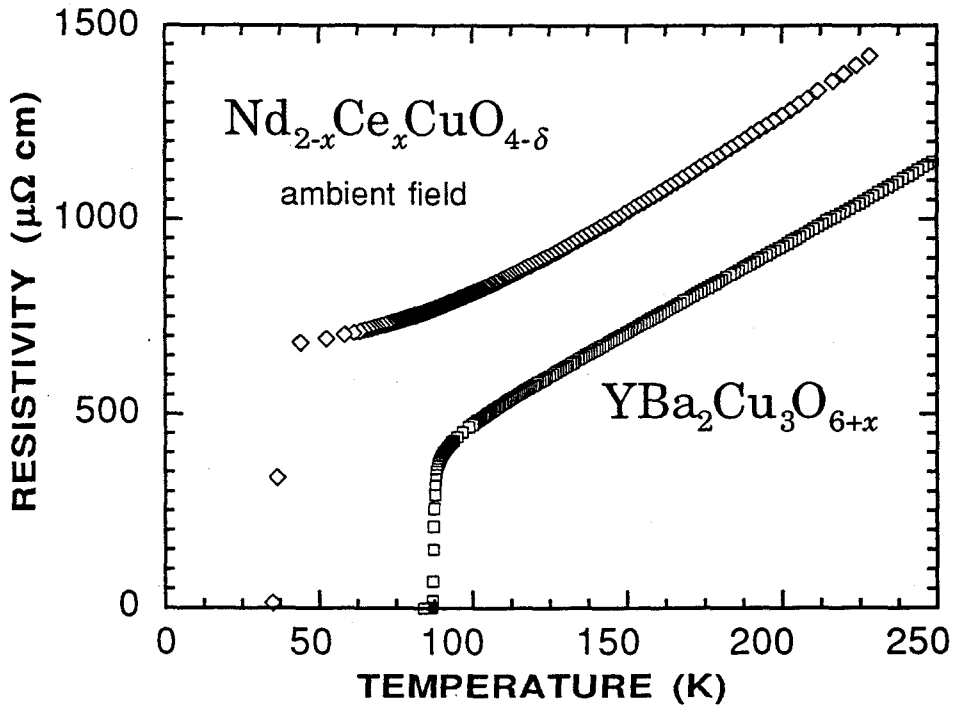

Figure 4.1 Resistive transition for $Nd_{2-x}Ce_xCuO_{4-\delta}$ and $Y_1Ba_2Cu_3O_{6+x}$ from 250 K down in ambient field.

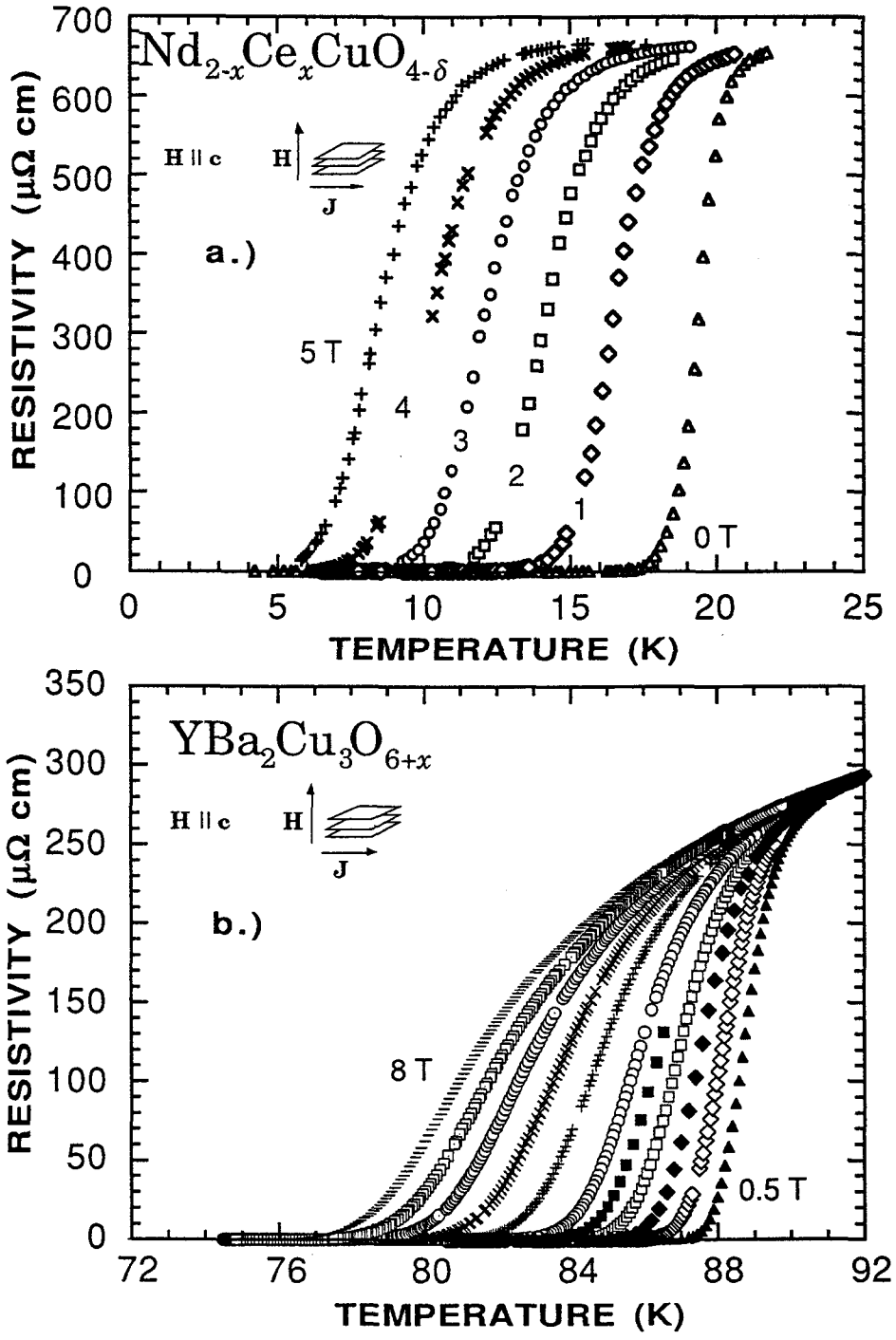

Figure 4.2 Resistivity versus temperature in linear plot for HIIc, $Nd_{2-x}Ce_xCuO_{4-\delta}$ at top and $Y_1Ba_2Cu_3O_{6+x}$ at bottom.

$Y_1Ba_2Cu_3O_{6+x}$ and $Nd_{2-x}Ce_xCuO_{4-\delta}$ also differ when they are normal conducting. $Y_1Ba_2Cu_3O_{6+x}$ shows an almost linear dependence of ρ with T, while for $Nd_{2-x}Ce_xCuO_{4-\delta}$ ρ increases quadratically with T. A plot from 250 K to below the transition for both superconductors is shown in figure 4.1. A linear fit to the $Y_1Ba_2Cu_3O_{6+x}$ data in a temperature region 100 K to 250 K results in a slope of 4.47 μΩcm/K and an intersection at $T = 0$ at $\rho = 38.83$ μΩcm. The correlation of the fit is 0.9998.

$Nd_{2-x}Ce_xCuO_{4-\delta}$ fits a quadratic dependence $\rho = \rho^* + m\ T^2$ with $\rho^* = 0.015$ μΩcm and $m = 656$ μΩcm/K^2, between 45 and 230 K. Here the data tend to slightly deviate from the fit at high temperatures.

4.1 Dependence of the Resistivity on the Applied Current

From the E-J analysis it is obvious that the applied current plays a major role for applying models to resistivity with temperature behavior[52]. In figure 4.3 we show how the resistivity depends on the measuring current. The glass temperatures are marked in the plot, error bars are within the thickness of the border line. All three sets show curves all most on top of each other (the resistivity depends only weakly on the applied current) and one curve far different. Note that the curve with the shallowest slope is at different current densities for the different fields: 18400 A/cm^2 for 1 and 2.5 T, but 184000 A/cm^2 for 5 T. For ρ (T) curves at different applied fields, J is generally constant. In such a set, for high current densities, the low field data could be in the vortex glass region, while the high fields could be in the TAFF regime particularly in the low T region. Note also the different scales for 1000/T. The curves within one

plot fan out with increasing current at a resistivity which is below the normal resistivity. However the point where the different data sets fan out shifts from 11.5 K^{-1} (1 T) to 11.65 K^{-1} (2.5 T) to 12.0 K^{-1} (5 T). We can therefore conclude that the ρ-T data for high resistivities should be described by a model which is independent of the measuring current, but strongly dependent on the applied field. Fluctuations and flux flow would both be good candidates, TAFF would be possible, too.

The white circles were obtained from linear E-J curves: they reflect the point where the the straight line dependence of E with J (see for example figure 3.4) goes smoothly over into an exponential behavior. It should approximately mark the border line between which the TAFF limit (currents lower than marked by the symbol) and flux creep limit. One can clearly see that the low currents lie in the TAFF limit. All the analysis subsequent to this section will be done in this region, where ρ versus T is almost independent of the applied current.

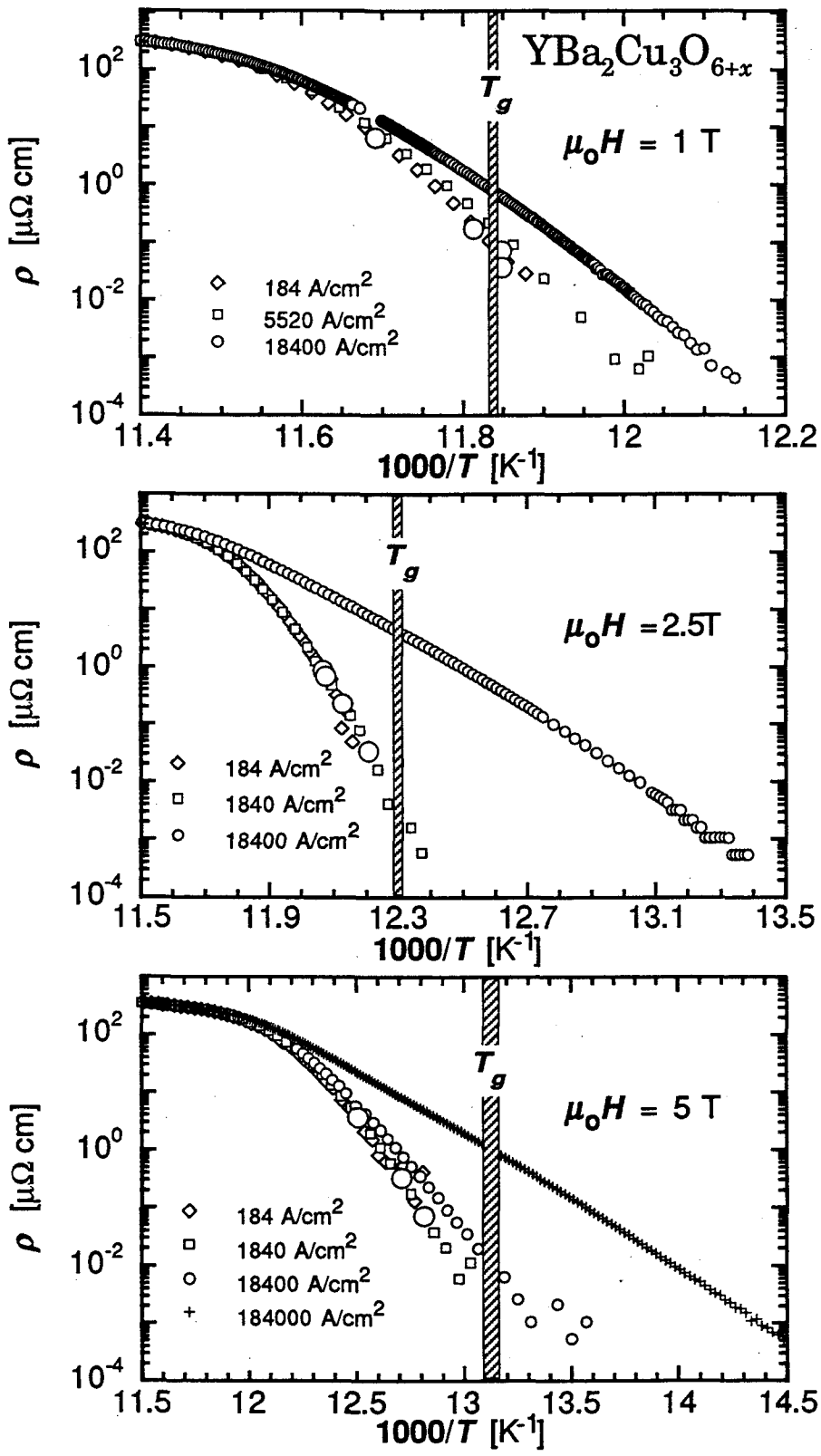

Figure 4.3 ρ versus $1/T$ with varying measurement current in the three fields 1 T, 2.5 T and 5 T. See also text.

4.2 Extracting the Upper Critical Field and Coherence Lengths

Upper critical fields in high T_c superconductors are high and therefore not accessible in direct measurements, but values for H_{c2} can be inferred from magnetization measurements and ρ-T curves at different applied magnetic field.

According to Helfand and Werthamer[53], a formula for H_{c2} can be derived from the Gor'kov equations:

$$H_{c2}(T=0) = -0.69 \cdot T_c \left.\frac{dH_{c2}(t)}{dT}\right|_{T=T_c} . \qquad (16)$$

With this the upper critical field $H_{c2}(T=0)$ can be obtained from the slope $dH_{c2}(T)/dT$ at $T=T_c$. The criterion used to determine T_c can change the results appreciably: generally $T_c(H)$ is defined as that temperature at which the resistivity in an applied field H drops to 50% of its normal state value. Figure 4.4 depicts how one determines $H_{c2}(T)$.

Figure 4.5 shows $H_{c2}(T)$ for both films. $Y_1Ba_2Cu_3O_{6+x}$ shows an almost linear $H_{c2}(T)$ versus T dependence at $T = T_c$ with slight upward bending for lower temperature values. Similar $H_{c2}(T)$ behavior is observed for $Nd_{2-x}Ce_xCuO_{4-\delta}$ in the H || c orientation. For H $\perp$ c, on the other hand, the relation follows a steep slope at low temperatures which goes over into a shallow slope close to T_c. Tinkham[61] claims that the shallow slope is due to flux pinning and therefore follows a different H_{c2} versus T dependence.

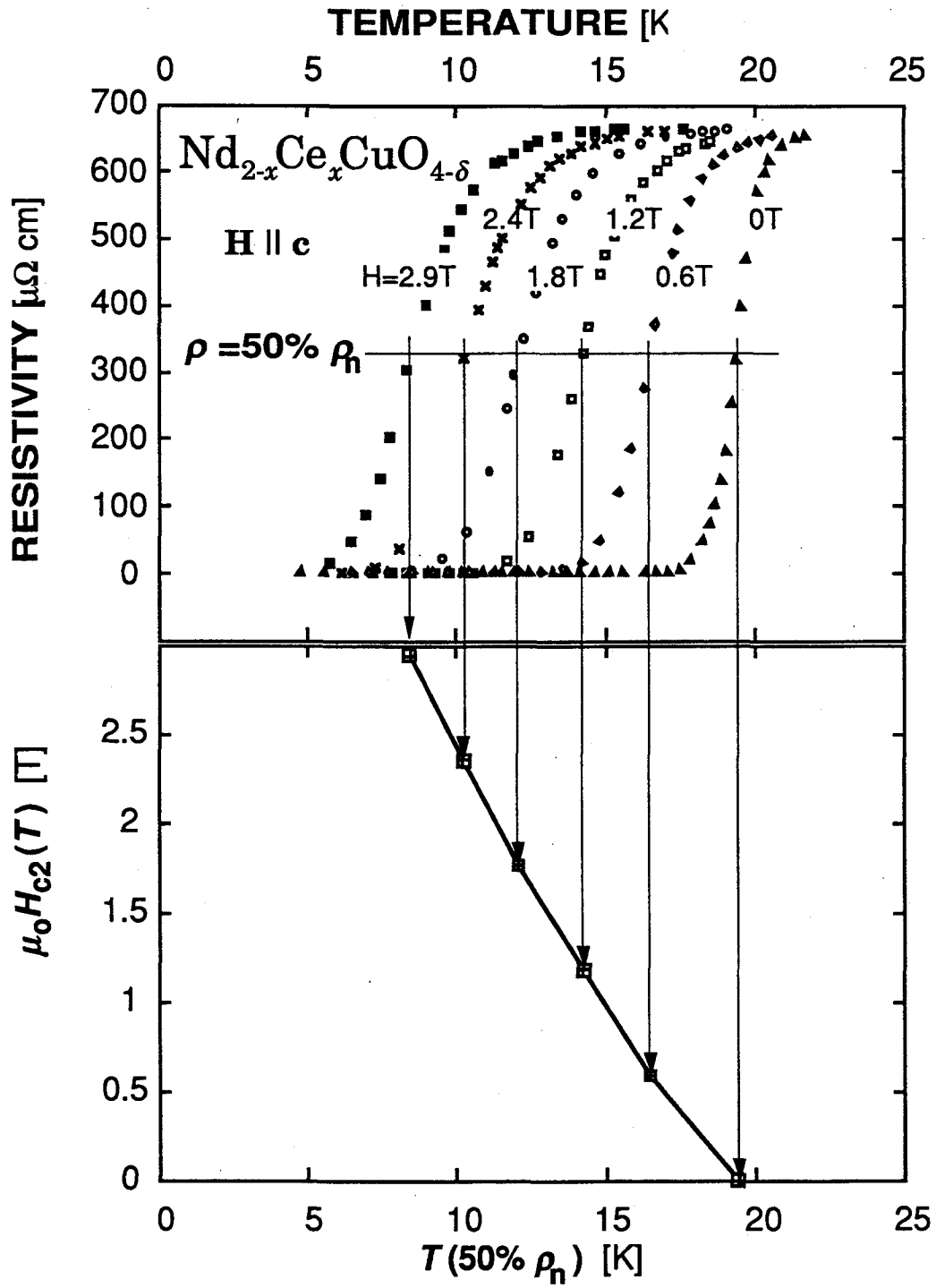

Figure 4.4 Determining H_{c2} with the 50% criterion.

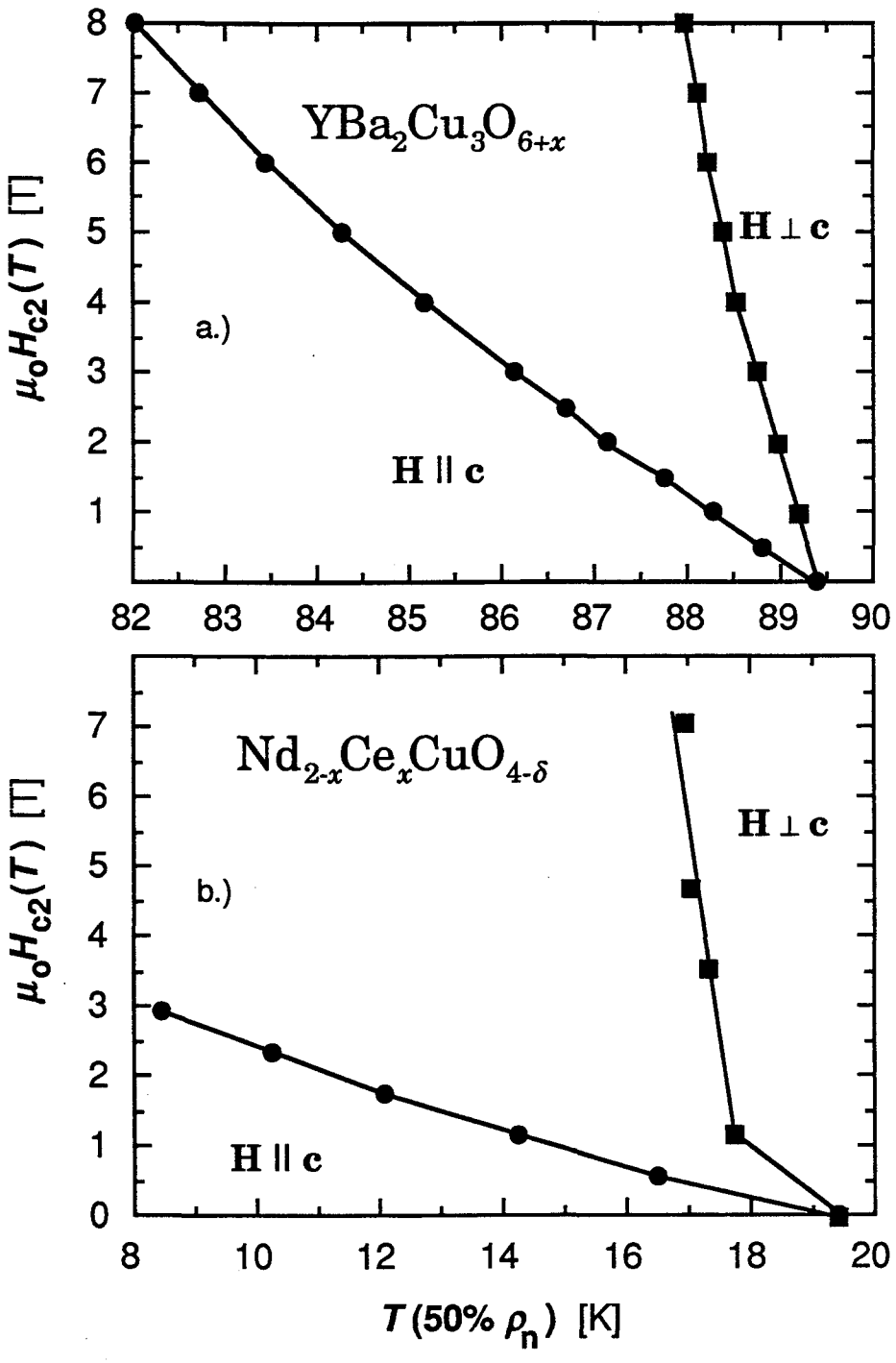

Figure 4.5 $H_{c2}(T)$ versus T plot for both orientations for a.) $Y_1Ba_2Cu_3O_{6+x}$ and b.) $Nd_{2-x}Ce_xCuO_{4-\delta}$.

Thus we used the steep slope in table 4.1, assuming a parallel shift of the curve with extrapolation to T_c. Taking the shallow slope would have resulted in $\mu_o H_{c2}(0)_{\perp \mathbf{c}} = 9.28$T. This is an unrealistic value, since the sample still showed perfect conductance at $T = 12.5$ K in 7T field.

With $H_{c2}(0)$ the coherence length in a-b and c-direction can be determined from Ginzburg-Landau theory[6], in the dirty limit:

$$\xi_{ab} = \sqrt{\frac{\phi_o}{2\pi H_{c2}(0)\big|_{\mathbf{H}\|\mathbf{c}}}} \; ; \quad \xi_c = \frac{\phi_o}{2\pi H_{c2}(0)\big|_{\mathbf{H}\perp\mathbf{c}} \cdot \xi_{ab}} \; . \qquad (17)$$

In table 4.1 the results for both films are summarized.

	$Nd_{2-x}Ce_xCuO_{4-\delta}$		$Y_1Ba_2Cu_3O_{6+x}$	
	H ⊥ c	**H ∥ c**	**H ⊥ c**	**H ∥ c**
$-(d\mu_o H_{c2}/dT)_{at\ T=Tc}$	5.09 T/K	0.20 T/K	4.88 T/K	0.91 T/K
$\mu_o H_{c2}(0)$	68.2 T	2.7 T	300 T	56.0 T
ξ_{ab}	-	108.76 Å	-	24.28 Å
ξ_c	4.27 Å	-	4.37 Å	-
$H_{c2}(0)_{\perp c}/H_{c2}(0)_{\|c}$	25.45		5.55	

Table 4.1 Experimental results for dH_{c2}/dT, H_{c2}, ξ_{ab} and ξ_c, obtained from the 50% of ρ_n criterion.

T. Fukami *et al.*[54] find $\xi_{ab} = 80$Å and $\xi_c = 2.3$Å and Suzuki and Hikita[55] find $\xi_{ab} = 70$Å and $-(d\mu_o H_{c2}/dT)_{\mathbf{H}\perp\mathbf{c}} = 9.3$K/T at $T_c = 21.6$K and $\xi_c = 2.3$Å for $Nd_{2-x}Ce_xCuO_{4-\delta}$. Since the CuO plane spacing is equal to 6.03Å, with the temperature dependence of ξ_c the latter authors calculated a two to three dimensional crossover for **H** ⊥ **c** at 15K. Our

value of $\xi_c = 4.27$Å is more than 2/3 of the CuO plane spacing and so we find $Nd_{2-x}Ce_xCuO_{4-\delta}$ more three dimensional. Fukami *et al.* and Suzuki and Hikita used (17) with 2π replaced by π, assuming our formula they obtain $\xi_{ab} = 99$Å and $\xi_c = 4.6$Å. Almasan *et al.*[56] determined H_{c2} from magnetic measurements of $Sm_{1.85}Ce_{0.15}CuO_{4-\delta}$. This is an n-type superconductor which belongs to the same family $L_{2-x}M_xCuO_{4-\delta}$ (L = Pr, Nd, Sm, Eu; M = Ce, Th). While their anisotropy is much lower $H_{c2}(0)_{\perp c}/H_{c2}(0)_{\parallel c} = 3.7$, $\xi_c(0) = 16.1$Å and $\mu_o H_{c2}(0)_{\parallel c} = 6.48$T lie in between our results obtained for the shallow and steep slopes. In summary, we confirmed an anisotropy as observed by Suzuki and Hikita for $Nd_{2-x}Ce_xCuO_{4-\delta}$, but not the strong two dimensionality.

In the $Y_1Ba_2Cu_3O_{7-\delta}$ case, 50% of ρ_n is not well defined, since ρ versus T shows a linear slope in the normal region and a fan shaped broadening in an applied magnetic field below T_c. Rather than an extension of the linear slope, we used a horizontal line through $\rho = 50\%\ \rho(H = 0T)$ for the above results. The results quoted by Almasan *et al.*[56] on single crystal $Y_1Ba_2Cu_3O_{6+x}$ find a factor of two higher values for $H_{c2}(0)$, but the anisotropy ratio $H_{c2}(0)_{\perp c} / H_{c2}(0)_{\parallel c} = 5.5$ comes close to our results.

Almasan *et al.*[56] find it controversial to determine the temperature dependence of H_{c2} from resistance versus temperature data. They argue that giant flux creep occurs and the $H(T)$ dependence reflects rather an irreversibility line rather than H_{c2}. Generally there is no match with H_{c2} values determined from magnetic measurements. However the 50% of ρ_n method seemed to be useful to us for comparison of our results with

previous work, even though there might be a better way to find the absolute value of these quantities.

4.3 TAFF and Flux Creep

The concept of thermally assisted flux flow and flux creep was already introduced the previous chapter about *I-V* curves. The resistivity versus temperature behavior in the TAFF and flux creep limits can be derived from formula (11) and (12) in chapter three. With the definitions $J_{c0}(H) = U/\mu_0 H \delta V \delta l$, $\rho_{c0}(H) = \mu_0 H \delta l \nu_0 / J_{c0}$ and $J_1 = J_{c0} k_B T/U$ this leads into two limits for the resistivity $\rho = E/J$:

$$\rho = \left(2\rho_c U / k_B T\right) \exp\left(-U / k_B T\right) = \rho_{TAFF} \qquad \text{for } J << J_1 \qquad (18)$$

$$\rho = \qquad \rho_c \frac{J_{c0}}{J} \exp\left(\left(J / J_{c0} - 1\right) U / k_B T\right) \qquad \text{for } J \approx J_1 . \qquad (19)$$

One notices at once that in the TAFF limit the resistivity is independent of the applied current, which we observed for current densities smaller than 10 A/cm^2 in $Nd_{2-x}Ce_xCuO_{4-\delta}$ and smaller than 184 A/cm^2 in $Y_1Ba_2Cu_3O_{6+x}$. An order of magnitude higher current densities showed only slight deviations.

Equation (18) may be written as

$$\rho = \rho_0 \exp(-U/k_B T) \text{ or } \ln\rho = \ln\rho_0 - U/k_B T, \qquad (20)$$

with ρ_0 weakly depending on temperature.

In an Arrhenius type plot logρ is graphed versus $1/T$, yielding U from the slope. Generally high T_c samples show no linear slope, therefore it is necessary to introduce a temperature dependence of $U(T)$.

4.4 The Temperature and Field Dependence of U,δl and δV

A more microscopic view is necessary to discuss the temperature and field dependence of U, δl and δV. Some general behavior can be predicted: the height of the potential well should go to zero for $T \to T_c$ and U is expected to get smaller with increasing magnetic field. A good introduction is given by Beasley *et al.*[57]. We review the literature here to summarize and to attempt to clarify the sometimes conflicting approaches. The simpler case $\mathbf{H} \parallel \mathbf{c}$ is primarily considered.

For the next discussion it is important to know the dimensions of a flux line. The cross sectional area of the normal core of a vortex is about $\pi\xi^2$; exactly $\pi\xi_{ab}\times\xi_{ab}$ for $\mathbf{H} \parallel \mathbf{c}$ and $\pi\xi_{ab}\times\xi_c$ for $\mathbf{H} \perp \mathbf{c}$. In the field direction a flux line extends either over the thickness of the film or the width of the bridge for $\mathbf{H} \parallel \mathbf{c}$ and $\mathbf{H} \perp \mathbf{c}$, respectively. Generally d will stand for the length that moves coherently in c-direction, what exactly it will be is model dependent. If the flux line is stiff, the whole length moves coherently. Brandt[46] suggests a flexible, spaghetti like flux line, which can cross and entangle other flux lines. In this case d would be close to the defect spacing. For a material which shows two dimensional superconductivity ($\xi_c <$ interlayer spacing) Clem[58] suggests pancake vortices for $\mathbf{H} \parallel \mathbf{c}$. These vortices are like pearls on a string loosely aligned along the c-direction of the unit cell. In that case the characteristic length scale in c-direction would be the layer spacing.

Due to the anisotropy in high T_c superconductors, the pinning center density is not expected to be homogeneous throughout the material. We define a *line density of pinning centers* in the *a*-,*b*- and *c*-directions of the unit cell: N_a, N_b, and N_c, with $N_a \approx N_b$. The *size of the*

defect in the a-b-direction of the superconductor is about r_p. In the c-direction a defect extends over r_c (for point defects $r_c = r_p$). The average spacing between defects in the a-b-direction is r_{inh}: $N_a = N_b = 1/r_{inh}$, and in the c-direction is L_c ($N_c = 1/L_c$).

For core pinning, which is the case most commonly discussed, a "perfect" defect would be of volume $\pi\xi^2 d$, with an interaction energy between defect and flux line $\varepsilon_0^* = (H_c^2/8\pi)\times\pi\xi^2 d$. Generally the interaction energy between the vortex and one pinning center will be called ε_0; how close it is to the pinning energy of a perfect defect depends on the model.

To estimate δV, the volume moving coherently when a flux line is unpinned, it is important to know $N_\square$, the density of pinning centers in the plane perpendicular to the direction of motion of the vortex. $N_\square$ can be either $N_c\times N_a$ or $N_a\times N_b$, depending on orientation of the external field. The *concentration of the defects* is given by $C = N_a\times N_b\times N_c$. Often the *number of defects in the coherence volume* is important, it will be called n_c.

The length δl is that distance an unpinned flux line moves until it is pinned again. It is not necessarily equal to the width of the potential barrier X_p, although some authors use them interchangeably. X_p is a measure of *the effective range of a pinning center*. A stiff correlated flux lattice will always move only the lattice spacing ($\delta l = a_0$), if the next pinning center is further away than a_0. For completely uncorrelated stiff flux lines (melted flux lattice) $\delta l \approx r_{inh}$, independent of the relative sizes of length scales. Based on Beasley's ideas[57] we discuss X_p and δl in figure 4.6 for a *highly correlated, stiff flux lattice.*

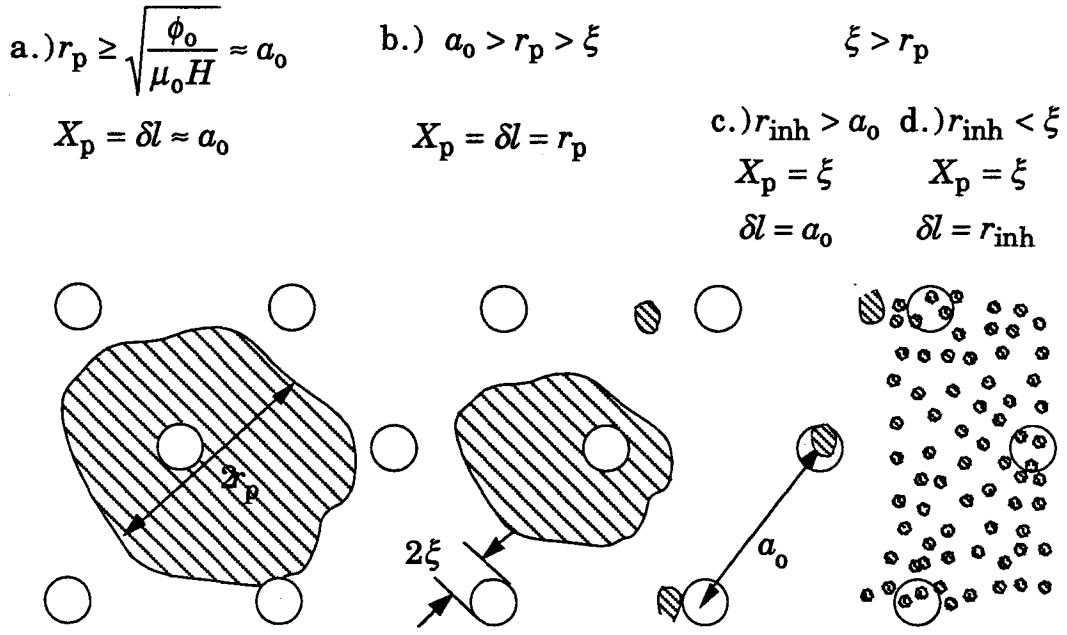

Figure 4.6 Relative size of pinning center r_p to flux line (open circles) and flux lattice spacing a_0. For pinning centers smaller than 2ξ the defect spacing r_{inh} becomes important. View: magnetic field perpendicular to the paper plane.

With the assumption for X_p in cases a to c, Beasley *et al.* distinguish between the three cases:

I.) low density of pining centers

high density of pinning centers

pinning centers distributed:

II.) randomly III.) in clusters

In case I the coherence volume $\delta V \approx 1/C$ and $U = \varepsilon_0$, one pictures a whole bundle of flux lines being relieved from the pinning center and moving together through the material. For dense, randomly distributed pinning centers, case II, the number of pinning centers per coherence volume n_c is given by the cross-section: $n_c = L_c X_p N_\square$, $L_c X_p$ defines the effective area of a pinning center perpendicular to the flux line motion. As the pinning centers are randomly distributed, only local variations in

the density of pinning centers account for the preferred places for flux lines to stay. So $U = \sqrt{n_c}\,\varepsilon_0$ and $\delta V = d\,a_0^2$, because the flux lines are stiff and there is not more than one pinning center per flux line. Beasley quotes Webb[59] for ε_0, we assume here $\varepsilon_0 = (H_c^2/8\pi)\times\pi r_p^3$ for a point defect, and $X_p = \xi_{ab}$ (case c. in figure 4.6). With Beasley's formulation and our assumptions for ε_0 and X_p this leads to:

$$U = \sqrt{\frac{L_c \xi_{ab}}{L_c r_{inh}}}\,\frac{H_c^2}{8\pi}\,\pi r_p^3 \qquad \text{after Beasley } et\ al.\,. \tag{21}$$

For the cluster case III. the energy difference per unit length of the flux line $\Delta E \approx \xi \Delta N \varepsilon_0$ with ΔN the difference in pin density. The activation energy is then given by $U = \Delta E l_c$, with l_c the extension of the cluster in c-direction in contrast to r_c the extension of the defect in c-direction. The average coherence volume would be given by $\delta V \approx 1/C$.

Yeshurun and Malozemoff[60] apply a scaling argument for $Y_1Ba_2Cu_3O_{6+x}$. They start with the perfect defect $\varepsilon_0^* = (H_c^2/8\pi)\times\pi\xi^2 d$, and argue that above $a_0 = 6\,\xi$ the energy per flux line is spread out evenly through the entire cell of the flux lattice. So ξ^2 should be replaced by a_0^2, and since ξ_c is the minimal length which moves coherently in c-direction, they set $d = \xi_c$:

$$U = \frac{H_c^2}{8\pi}\,\pi a_0^2 \xi_c \qquad \text{Yeshurun and Malozemoff} \,. \tag{22}$$

Tinkham[61] argues that rows of flux lines pass neighboring rows and that the kinetics of the thermally activated motion of these rows is similar to the phase motion in a current-driven Josephson junction, where the Ambegoakar-Halperin model applies. Using this model Tinkham

obtains the same temperature and field dependence for $Y_1Ba_2Cu_3O_{6+x}$ as in (22).

Fisher[62] starts from the idea of a perfect defect, so $\varepsilon_0 = \varepsilon_0^* = (H_c^2/8\pi)\times\pi\xi^2 d$. If there are many pinning centers present per flux line (case d. figure 4.6) the energy ε_0^* has to be multiplied by the square root of the fraction the pinning centers occupy of the volume of a flux line. It is not clear why Fisher uses the square-root of the fraction as pre-factor, maybe he has a similar statistical argument to Beasley. His analysis leads to:

$$U = \sqrt{\frac{r_p^3}{\pi\xi^2 d}}\frac{H_c^2}{8\pi}\pi\xi^2 d \qquad \text{Fisher .} \qquad (23)$$

One of Yeh's models[63] treats the same case as Fisher (case d. in figure 4.6). She sets the pinning potential equal to the perfect defect divided by the number of pins per flux line:

$$U = \left(\frac{r_{inh}^2 L_c}{\pi\xi_{ab}^2 d}\right)\frac{H_c^2}{8\pi}\pi\xi^2 d \qquad \text{after Yeh ,} \qquad (24)$$

note that she also leaves out the square root, even though she quotes Fisher's result for the origin of the formula. Formula (24) is not Yeh's final result, she introduces more length scales and approximations, in the end $(H_c^2/8\pi)\pi\xi^2 d$, which is field independent and temperature dependent, is replaced by a field dependent, temperature independent quantity.

Suzuki and Hikita[55] start with $\varepsilon_0 = (H_c^2/8\pi)\times\pi r_p^2 d$, which is a much smaller volume than $(H_c^2/8\pi)\pi\xi^2 d$ in Fisher's model. They reduce further by dividing with the same pre-factor that Yeh (24) uses:

$$U = \left(\frac{r_{inh}^2 L_c}{\pi\xi_{ab}^2 d}\right)\frac{H_c^2}{8\pi}\pi r_p^2 d \qquad \mathbf{H}\|\mathbf{c} \qquad \text{Suzuki and Hikita .} \qquad (25)$$

For the case $\mathbf{H}\perp\mathbf{c}$ they replace the one ξ_{ab} with ξ_c. Then they argue to replace L_c with ξ_{ab}, and set ξ_c = const. They do not really specify the length scale in c-direction of the unit cell. We would change the length in field direction to either the width w or the length l of their bridge, and replace L_c by ξ_c, because they assume 2-dimensionality, and finally one factor of r_{inh} in (25) by ξ_{ab}. Either approach results in the same temperature dependence:

$$U = \left(\frac{r_{inh}\xi_{ab}\xi_c}{\pi\xi_{ab}\xi_c d}\right)\frac{H_c^2}{8\pi}\pi r_p^2 w \qquad \mathbf{H}\perp\mathbf{c}. \qquad (26)$$

For the $\mathbf{H}\perp\mathbf{c}$ orientation intrinsic pinning is large due to the larger order-parameter (or probability amplitude) for the paired electrons in the CuO planes. Probably the intrinsic effect is larger than the effect of the pinning centers. A indication of this is the large anisotropy for the two orientations. Simply a higher line density of defects in a-b-direction could not account for the big change of T_c.

These temperature dependences can be made explicit by using Ginzburg-Landau theory[6] :

$$H_c(t) \propto 1-t^2; \;\; \xi^2(t) \propto \frac{1+t^2}{1-t^2}; \; a_0 = \sqrt{\frac{2\phi_0}{\sqrt{3}\mu_0 H}}\,, \qquad (27)$$

where the first two approximations are restricted to reduced temperatures $t = T/T_c \geq 0.5$.

All activation energies U depend on temperature and in some models on the applied magnetic field. Because U only contains temperature originating from either H_c or ξ, all suggestions discussed so far can be summarized in:

$$U(H,t) \propto H_c^2(t)\xi^n(t) \quad \text{with } n \text{ between } -2 \text{ and } 1. \tag{28}$$

Introducing $q = 2 - n/2$ this leads to:

$$U(t) = U_0 \frac{\left(1-t^2\right)^q}{\left(1+t^2\right)^{q-2}} \quad \text{with } q \text{ between 3 and 1.5 .} \tag{29}$$

A summary of the different models is given in table 4.1.

group:	model valid for:	field:	n =	q =
after Beasley *et al.*[57]	random, dense pins	-	0.5	1.75
Malozemoff *et al.*[60]	$Y_1Ba_2Cu_3O_{6+x}$,twin boundary	U~1/H	1	1.5
Fisher[62]	random, very dense pins	-	1	1.5
after Yeh[63]	random, very dense pins	-	0	2
Suzuki and Hikita[55]	small, very dense pins:**H**‖**c**	-	-2	3
	H⊥**c**	-	0	2

Table 4.2 Temperature and field dependence of the activation energy in various models.

Very close to T_c (for t larger than 0.9) one can approximate:

$$\mathbf{H}_c(t) \propto 2(1-t) \quad \text{and} \quad \xi^2(t) \propto \frac{1}{1-t}\,, \tag{30}$$

which explains the commonly used approximation for $U(t)$, here called $U_{Tc}(t)$ to distinguish:

$$U(t)\big|_{T \approx T_c} = U_0\, 4(1-t)^q \tag{31}$$

however the factor of 4 seems to be left out very often. In the literature either $U(\rho = 0.1\ \mu\Omega cm)$ or $U(\rho = 1\%\ \rho_n)$ or $U_0 = U(T{=}0)$ is quoted. One has to be careful with comparisons for different materials.

There are two methods to extract the potential U(t) from the data. Both methods start with an initial guess of the exponent q in (29) or (31). The first method assumes U to be temperature independent and then applies a correction to account for temperature dependence. Most data published on $Y_1Ba_2Cu_3O_{6+x}$ follow this method. The second method does a three parameter fit to $\ln\rho$ versus T^{-1} with parameters U_0, T_c and ρ_0.

4.5 The Activation Potential with the Enhancement Method

First a straight line is interpolated through the low temperature data plotted in an Arrhenius type plot and the slope is extracted. From a temperature dependent activation energy $U(T)$ as in (29), together with (20) follows:

$$\frac{\partial \ln(\rho)}{\partial 1/T} = -\partial U(T)/\partial(1/T) = -U(T)\times enh, \tag{32}$$

where

$$enh = 1 + 2t^2\left\{\frac{q}{\left(1-t^2\right)} + \frac{q-2}{\left(1+t^2\right)}\right\}. \tag{33}$$

In Malozemoff's paper[64], where this method was introduced first, $U(T)$ on the right of (32) appears as U_0.

Thus the slope in an Arrhenius plot does not give $U(T)$, but $U(T)$ enhanced by some temperature dependent factor *enh*. One can extract $U(T)$, and hence U_0, by picking a particular t (this implies a choice of T_c)

and correcting the value obtained from the slope of the straight line by dividing by enh (33). The temperatures at which $\rho = 0.1$ μΩ cm or $\rho = 0.01\ \rho_n$ and $q = 1.5$ are common choices. We will call this reduced value for the activation energy: U_{red}, because it is only valid at a particular resistivity.

This method should give reasonable results, provided the enhancement factor varies slowly with temperature in the region the slope is interpolated. In figure 4.7 the temperature dependence of enh is plotted in the form (33) and for the approximation $\partial \ln\rho/\partial(1/T) = -U_0 4(1-t)^q enh$ with $enh = 1+qt/(1-t)$, which follows from (31); Palstra *et al.*[65] missed the factor of four in their derivation of this approximation. With increasing exponent q one needs to be further away from T_c to keep the errors small due to the straight line interpolation. We applied this analysis at temperatures $T(\rho = 1\%\ \rho_n)$, which corresponds to $\rho = 6.5$ μΩcm for $Nd_{2-x}Ce_xCuO_{4-\delta}$ and $\rho = 2.7$ μΩcm for $Y_1Ba_2Cu_3O_{6+x}$. T_c was defined as T at $\rho = 90\%\ \rho_n$ and $q = 1.5$ in (33) this lead to values U_{red}, smaller by a factor 2 to 12 than the slope for $Nd_{2-x}Ce_xCuO_{4-\delta}$, and smaller by 13 to 70 for $Y_1Ba_2Cu_3O_{6+x}$.

The results are tabulated for $Y_1Ba_2Cu_3O_{6+x}$ for **H** ∥ **c** in table 4.3 and the rest is shown in Appendix B.

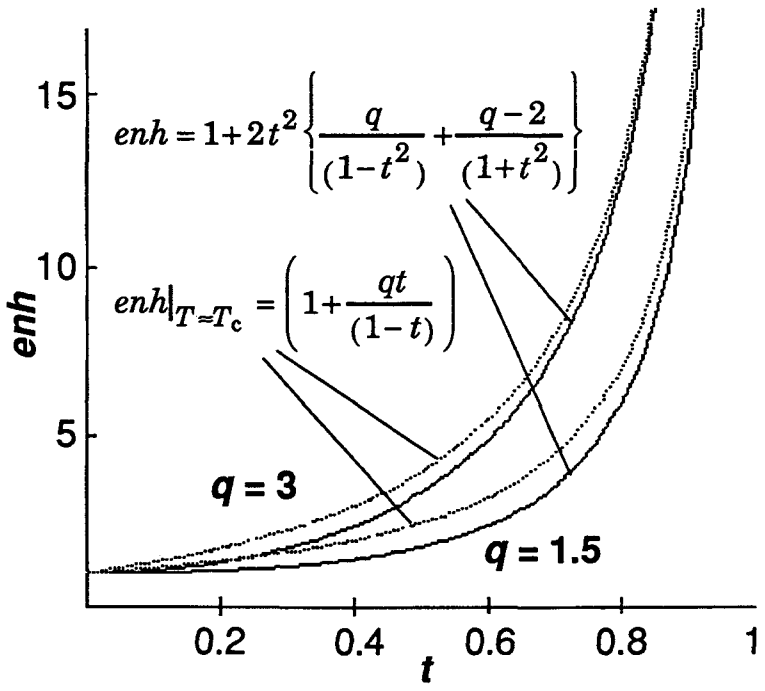

Figure 4.7 Enhancement factor for $U(T)$, exact and with approximation. *Enh* starts to vary strongly with temperature above $t = 0.6$ and $t = 0.8$ for $q = 3$ and $q = 1.5$ respectively.

	$\mu_0 H$ [T]	T_c [K]	slope [eV]	1000/T [K^{-1}]	$t = T/T_c$	enh	U_{red} [meV]
H ‖ c	1	90.62	2.317	11.560	0.9546	31.3	73.954
	2	90.16	1.702	11.786	0.9410	23.7	71.733
	3	89.41	1.330	12.013	0.9310	20.1	66.329
	4	88.93	1.137	12.240	0.9189	16.8	67.600
	5	87.98	1.015	12.438	0.9138	15.7	64.526
	6	87.12	0.939	12.626	0.9091	14.8	63.297
	7	86.56	0.869	12.796	0.9028	13.8	63.102
	8	85.75	0.817	12.957	0.9000	13.3	61.235

Table 4.3 U_{red} with 1% of ρ_n resistive criterion for $Y_1Ba_2Cu_3O_{6+x}$ for **H ‖ c** orientation. See also text.

The effect of the reduction is plotted for $Nd_{2-x}Ce_xCuO_{4-\delta}$ in figure 4.8. While the linearly interpolated slope as function of the applied magnetic field falls off strongly with increasing field, U_{red} varies slowly almost linearly with H. A straight line fit results in U_{red}[meV] = 6.08 – 1.27H for **H** ∥ **c** and U_{red}[meV] = 5.97 – 0.15H for **H** ⊥ **c** (H in Tesla). U_{red} for $Y_1Ba_2Cu_3O_{6+x}$ behaves similarly: U_{red}[meV] = 89 – 1.71H for **H** ∥ **c** and U_{red} nearly independent of H for **H** ⊥ **c**. Interesting is that the U_{red} values for $Y_1Ba_2Cu_3O_{6+x}$ are within a factor 12 of the $Nd_{2-x}Ce_xCuO_{4-\delta}$ values, even though the slopes are more than two orders of magnitude higher.

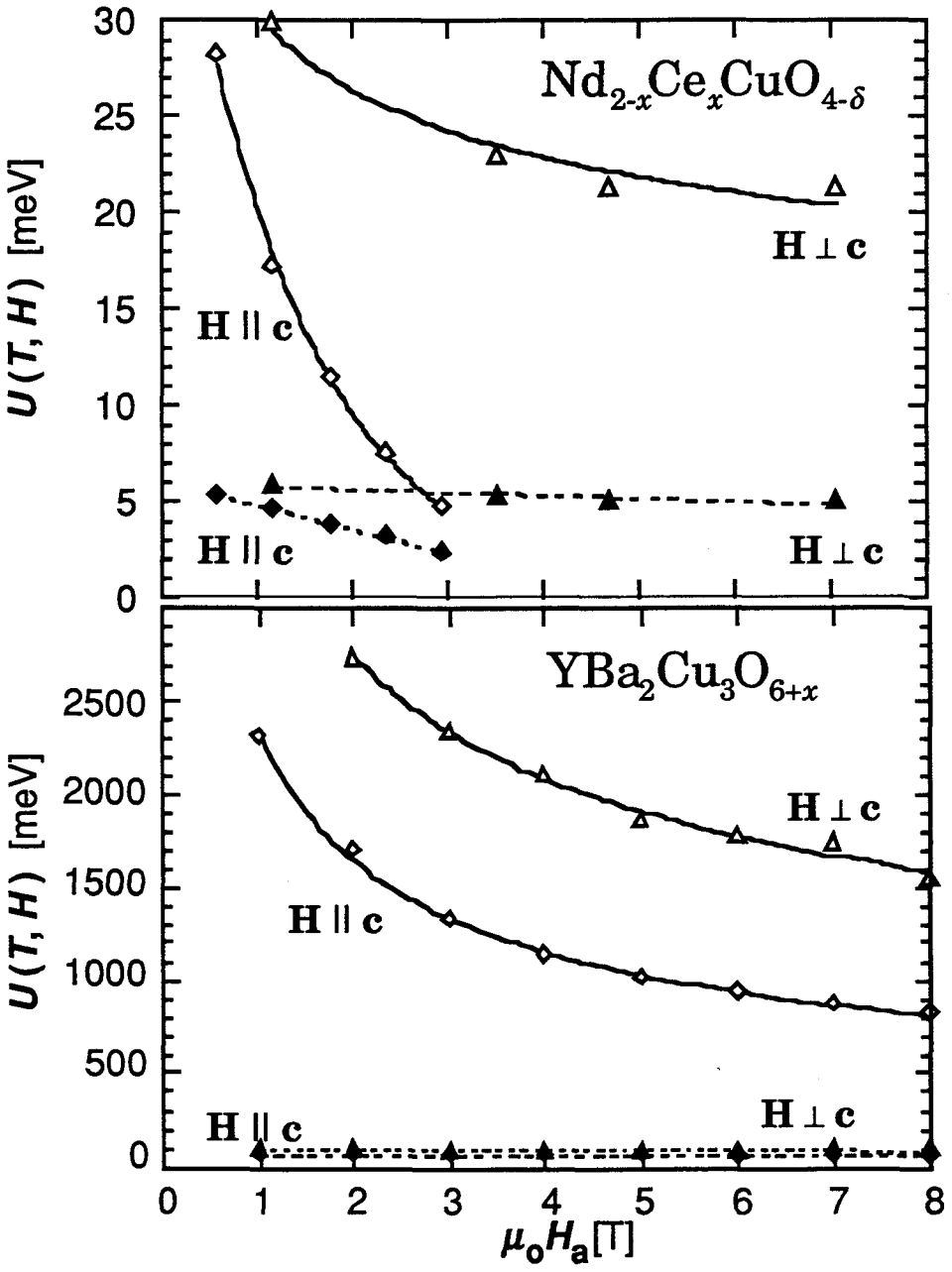

Figure 4.8 Results of enhancement correction for activation energies of $Nd_{2-x}Ce_xCuO_{4-\delta}$ and $Y_1Ba_2Cu_3O_{6+x}$. Open symbols: slope at ρ = 1% ρ_n, solid line guide to the eye; solid symbols: U_{red} calculated assuming q = 1.5 and T_c values as in table 4.3, dashed line linear fit.

Malozemoff *et al.*[64] have obtained U_{red} values for single crystal $Y_1Ba_2Cu_3O_{6+x}$ at 0.1 μΩ cm (q = 1.5, T_c = 92.8 K, **H** ∥ **c**, J = 5 A/cm^2) between 116.33 and 86.12 meV for $\mu_0 H$ between 1 and 9 T. Palstra's results, re-anlysed by Malozemoff *et al.*[55] (ρ = 0.1 μΩ cm, q = 1.5, T_c = 88 K, **H** ∥ **c**), lie between 142 and 99 meV for $\mu_0 H$ between 1 and 10 T. Our values compare well. They are slightly lower maybe because we applied the correction at 1 % rather than 0.1 μΩcm. They do not assume a shifting T_c which results in slightly lower values for t (Malozemoff has t between 0.96 and 0.82 for $\mu_0 H$ between 1 and 9 T) and consequently lower values for *enh* (see figure 4.7). This is one point of criticism about this method, that T_c, which influences t and therefore *enh*, has to be guessed. A second point is that in the region in which the correction is applied, *enh* varies still strongly with T, even for Malozemoff's and Palstra's lower values of t. In fact, for **H** ⊥ **c**, because of the minimal voltage which can be measured, no data point can be obtained in a region where *enh* is almost constant with t. Also, for **H** ∥ **c** we have to argue that different T_c's for different fields need to be chosen (at least for $Nd_{2-x}Ce_xCuO_{4-\delta}$), which is a new point of uncertainty in the analysis. This method also only reveals a set of $U(T)$ which are defined by a certain resistive criterion and only valid at this particular resistance. One could argue that, if one knows $U(T)$ at a particular resistivity and therefore T, and the dependence of $U(T) = U_0(1-t)^q$ is known, as well as q, one can calculate U_0. However the slope was obtained from interpolating many data points in a region of t, where *enh* varies strongly with t; a slightly different choice of the resistivity and a lower T_c might account for a factor two to four different *enh*. Attention has to be given also to the current

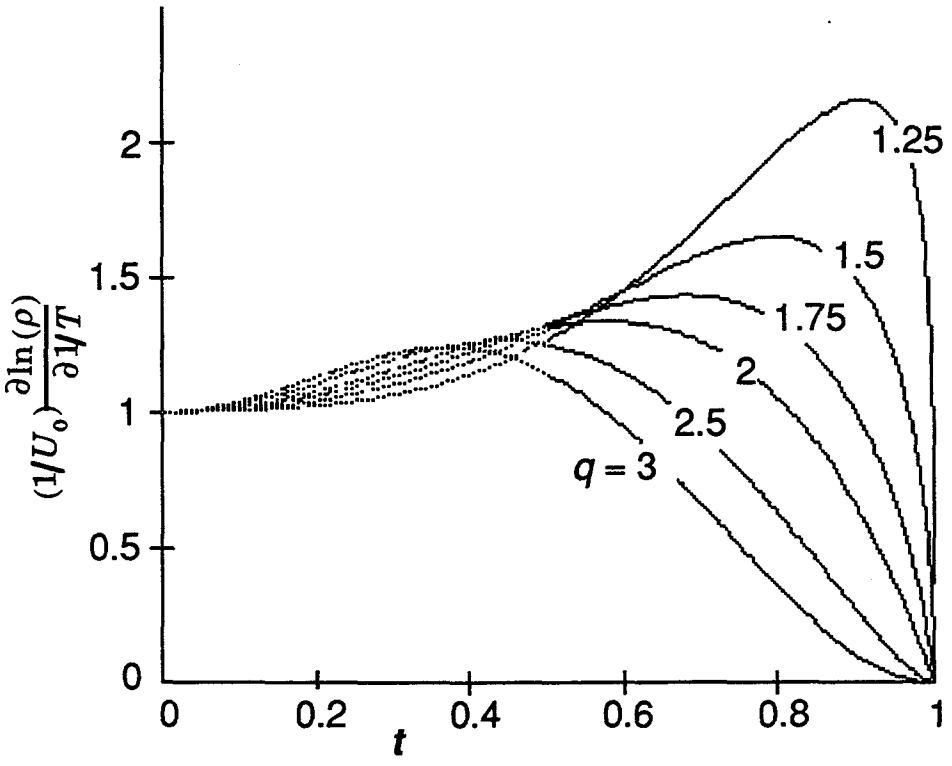

Figure 4.9 Plot of theoretical temperature dependence of the normalized slope of an Arrhenius type plot.

dependence of the slope see chapter 4.3. A good point about this method is that it is fast for comparison with other people.

The correction methods does make a statement of what $\partial \ln\rho/\partial(T^{-1})$ versus T^{-1} looks like, see figure 4.9. We calculated $\partial \ln\rho/\partial(T^{-1})$ and normalized the data with U_0 calculated assuming $q = 1.5$. U_{red} divided by $(1 - t^2)^q / (1 + t^2)^{q-2}$ extracts U_0 from formula (29) and (32). The result is shown in figure 4.10. One would expect the data to lie on top of each other. Since they are normalized with U_0, the curve should only reflect the enhanced temperature dependence of $U(T)$ formula (32 and 22), independent of the applied field. This is not quite the case, but the high

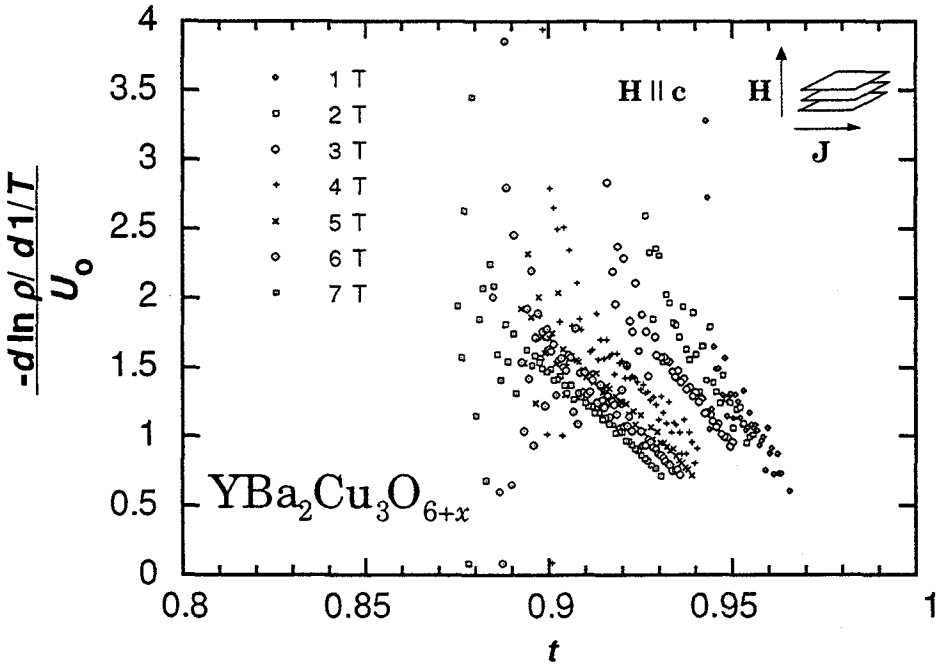

Figure 4.10 Normalized Arrhenius slope for $Y_1Ba_2Cu_3O_{6+x}$ with the assumption $q = 1.5$. Data for different fields should fall on top of each other.

fields come close. In figure 4.10 only the data which were used for the straight line interpolation are showed. A linear extraction of the data to high t does not yield $\partial \ln\rho/\partial(T^{-1}) = 0$ for $t = 1$, as theoretically predicted for $q = 1.5$ (see figure 4.9). Thus one might tend to higher values of q, which show a more gradual increase with decreasing t.

The models reviewed in chapter 4.4 predicted a field dependence only for $U_0 = U(T = 0)$. We used the three parameter fit, described next, to extract a pure field dependence of $U_0(H)$ and compare both methods in the section after that.

4.6 The Activation Energy with a Three Parameter Fit

This method determines U_0, ρ_c and T_c by a least squares fit of

$$\ln\rho = \ln\rho_0 - \frac{U_0}{k_B T}\frac{\left(1-(T/T_c)^2\right)^q}{\left(1+(T/T_c)^2\right)^{q-2}} \qquad (34)$$

to the data in an Arrhenius plot. Just as in the enhancement method, described in section 4.5, a value for q has to be initially guessed. In the $Nd_{2-x}Ce_xCuO_{4-\delta}$ case, this method was applied with exponents q=2 or 3 for $\mathbf{H} \parallel \mathbf{c}$ and $\mathbf{H} \perp \mathbf{c}$[55] or q=3 for both orientations[66]. We used q = 1.5, 2 and 3 to try to fit our data, in the hope that the best fit would favor one of the models reviewed in section 4.4 and eventually give some microscopic insight about pinning.

We found that all three values of q fit the $Nd_{2-x}Ce_xCuO_{4-\delta}$ data very well; and we discovered that more data close to T_c can be included with a larger q. Also $Y_1Ba_2Cu_3O_{6+x}$ can be fit beautifully to q = 2 and 3, even though q = 1.5 is standard and higher values were never discused. A q = 3 fit for $Y_1Ba_2Cu_3O_{6+x}$ in the $\mathbf{H} \perp \mathbf{c}$ orientation is shown in figure 4.11, all the data shown were included in the fit. Our results for q = 1.5 are shown in figure 4.13 for $Nd_{2-x}Ce_xCuO_{4-\delta}$ and figure 4.12 for $Y_1Ba_2Cu_3O_{6+x}$. The overlaid line represents the curve fit, and only data in the overlay region were included into the fit.

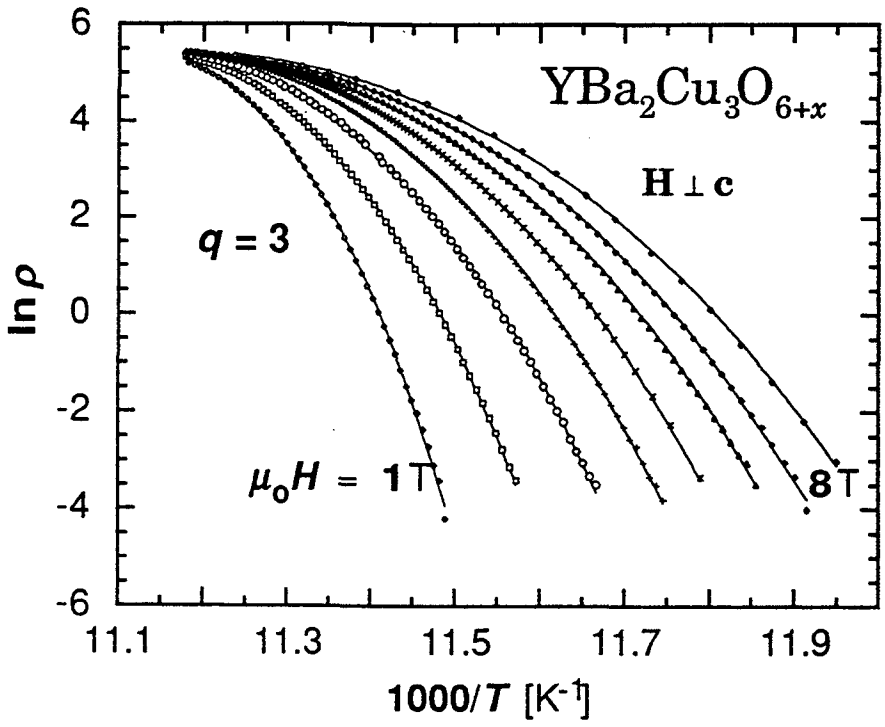

Figure 4.11 Curve fit with q = 3 for **H** ⊥ **c** for $Y_1Ba_2Cu_3O_{6+x}$.

If one compares figure 4.11 with 4.12 the ability of the fitting function (34) with $q = 3$ to fit data much closer to T_c is obvious. For $Y_1Ba_2Cu_3O_{6+x}$ (figure 4.12) the constant change in slope to steeper values is very pronounced, even enlargements of small parts of the curve show a distinct convex bending. The necessity of a temperature dependent activation energy is clear.

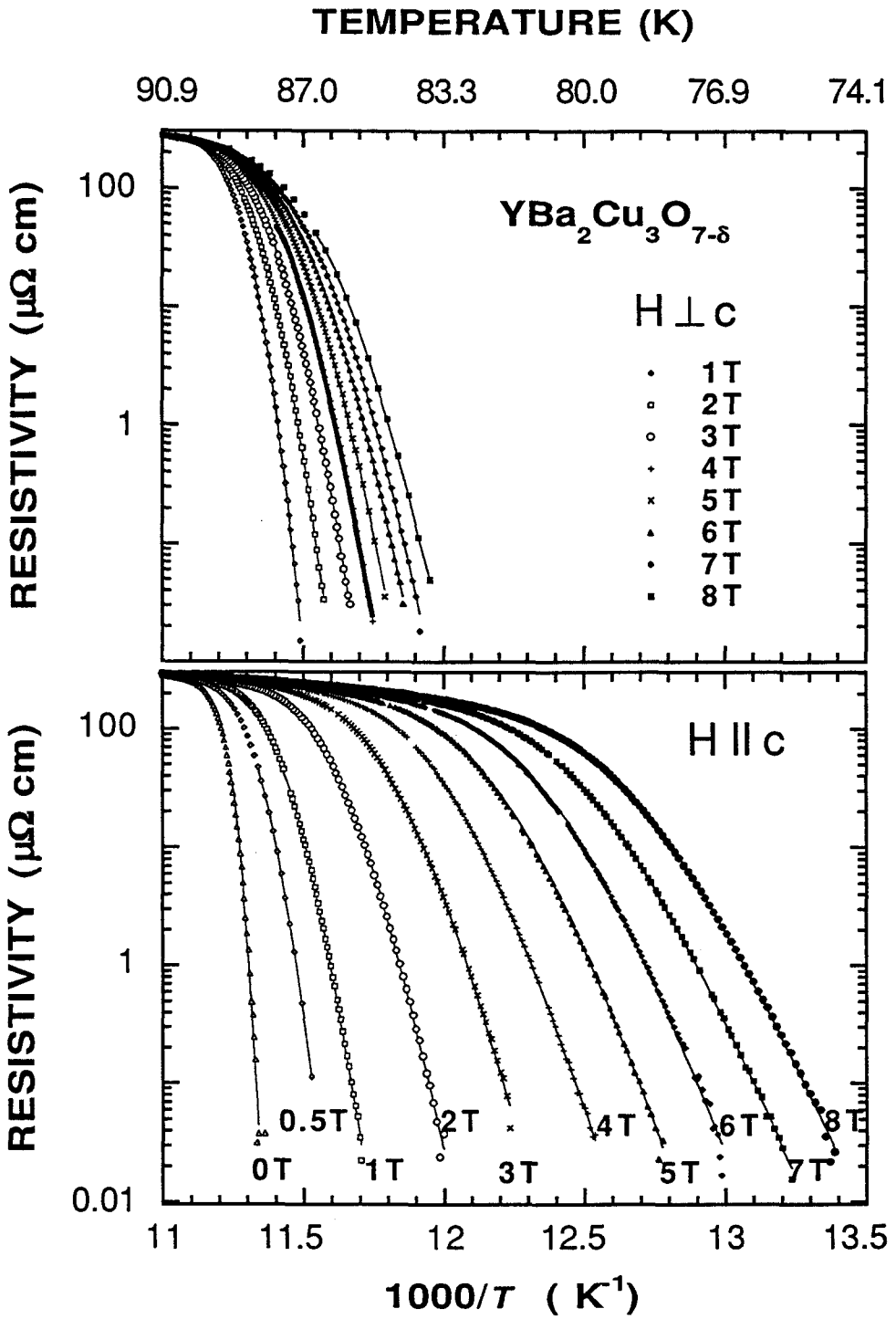

Figure 4.12 Curve fit (solid line) with $q = 1.5$ for $Y_1Ba_2Cu_3O_{6+x}$.

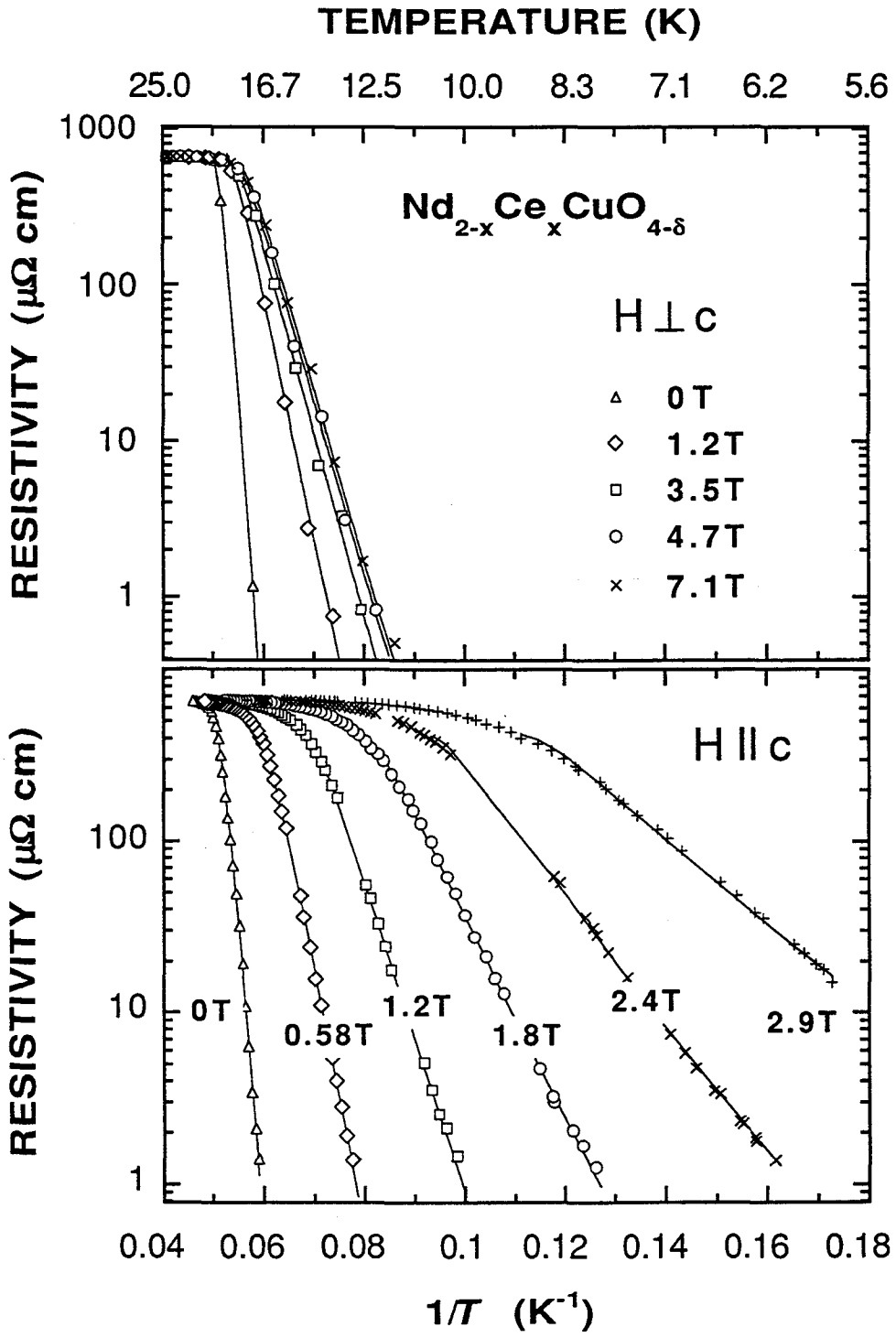

Figure 4.13 Curve fit (solid line) for $Nd_{2-x}Ce_xCuO_{4-\delta}$, $q = 1.5$.

$Nd_{2-x}Ce_xCuO_{4-\delta}$ shows an almost linear behavior of log resistivity with $1/T$. The resistivity data span 3 orders of magnitude. The sensitivity of our equipment allows us to measure further 3 orders lower, but there was a distinct change in slope of the resistivity at all fields below about 0.5 μΩcm. The resistivity fell off much more slowly, at a rate independent of field. The distinct change in slope always occurs at the same resistivity, independent of applied current. Therefore dissipative mechanisms at a certain power or some instrumental systematic error at a certain measured voltage can be excluded. We might have a second superconducting phase in the sample, which shows a broader transition at lower temperatures, since the data fall below measurable resistance even with the change to a shallower slope. We do not include this data in our analysis here.

Since our findings were partially in contradiction with the two Japanese groups[55,54], we tried to distinguish between the three curve fits for $Nd_{2-x}Ce_xCuO_{4-\delta}$, which looked equally good to the bare eye. One way was to calculate χ^2 values for the curve fits. It was hard to compare results, because the fits included different numbers of data points. However when we fit data up to $t \approx 0.89$ for all values of q, $q = 1.5$ showed a somewhat better response.

The fitting parameters, which we obtained from the least squares fit, depend on the choice of q. To get comparable results, we fit the data up to $t = T/T_c = 0.89$. That corresponds to different amount of data included close to high temperatures and resistivities, due to the different shapes of (34) for the different values of q.

The values obtained for the parameter T_c are plotted in figure 4.14. For $Nd_{2-x}Ce_xCuO_{4-\delta}$ (bottom of figure 4.14) and $\mathbf{H} \perp \mathbf{c}$, regardless of the choice of q, T_c decreased less than 2 K between 0 and 7 T, while for $\mathbf{H} \parallel \mathbf{c}$, T_c decreased by 10 K in a 3-T range. The error bars on T_c are only slightly larger than the symbol size, so it is clear that different choices of q require different interpretations of "T_c", at least for the $\mathbf{H} \parallel \mathbf{c}$ orientation. For $q = 1.5$, T_c corresponds to a point where deviations of $\ln\rho$ vs T^{-1} from linearity just become significant, that corresponds roughly to a choice of T_c with a 50% of ρ_n criterion. While for $q = 2$ or 3, T_c corresponds to a point where the resistivity is just beginning to drop from the normal state value, and is close a 90% ρ_n criterion for $q = 2$.

That higher q values correspond to "T_c" at higher resistivities is also true for $Y_1Ba_2Cu_3O_{6+x}$. However the shift to lower T_c with increasing field is much weaker. T_c decreased only by 8.5 K in an 8–T range for $\mathbf{H} \parallel \mathbf{c}$ and by less than 1 K for $\mathbf{H} \perp \mathbf{c}$, for the same field range. Remarkably the $q = 3$ fit, which is shown in figure 4.11, produces a T_c independent of applied field.

The values of ρ_0, shown in figure 4.15, are also sensitive to exactly which data are included in the fit. There is a tendency for higher q values to produce a ρ_0 which decreases slightly with higher field. This parameter is within a factor of two of the normal state resistivity in the case of $Nd_{2-x}Ce_xCuO_{4-\delta}$ for any choice of q, and a factor of five in the case of $Y_1Ba_2Cu_3O_{6+x}$. In almost all cases $q = 1.5$ produces almost constant values of ρ_0 with applied field. Eventually the full temperature dependent form (formula (9) chapter 3.1) for ρ_c, which is contained in $\rho_0 = 2\rho_c U_0/k_B T$, has to be used for higher values of q.

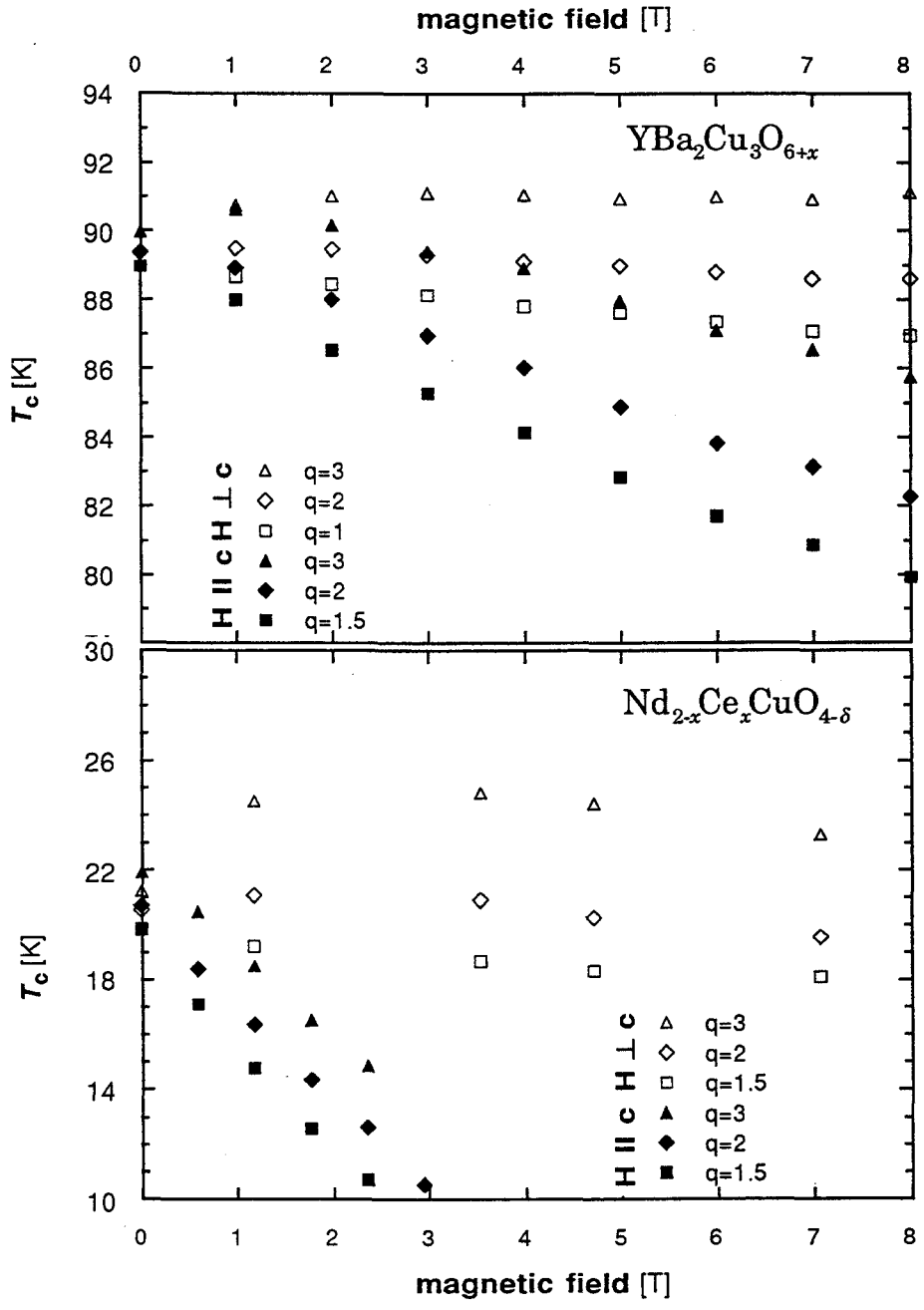

Figure 4.14 Field dependence of fitting parameter T_c. For **H ∥ c** both $Y_1Ba_2Cu_3O_{6+x}$ and $Nd_{2-x}Ce_xCuO_{4-\delta}$ show a down ward shift of T_c with increasing field.

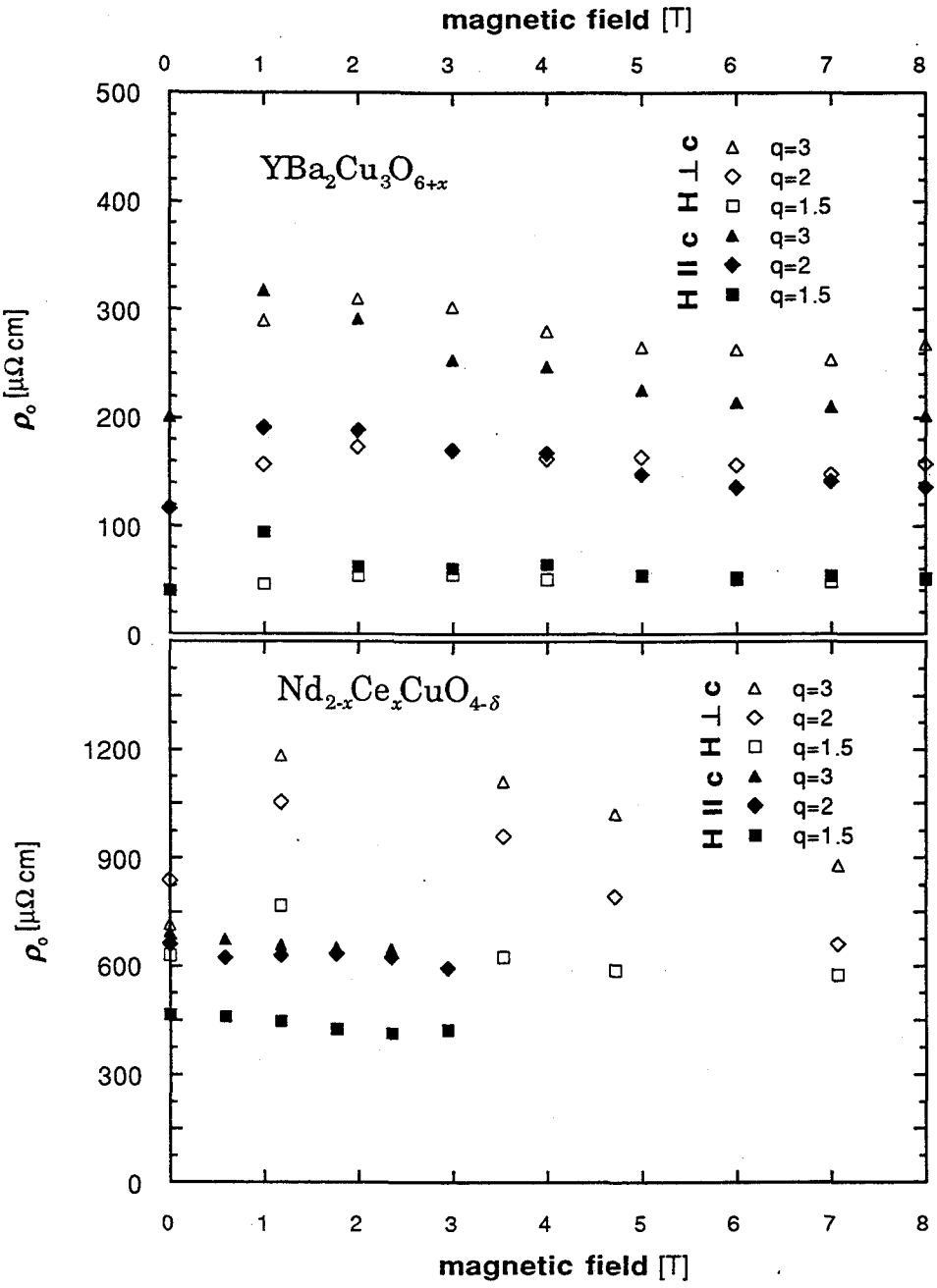

Figure 4.15 Field dependence of fitting parameter ρ_0.

For $Nd_{2-x}Ce_xCuO_{4-\delta}$ in the **H** ∥ **c** orientation, the values of $U_0(H)$ range from about 80 meV to 3 meV (0.5 to 3 T). The results of Fukami *et*

al.[66] range from 102 meV to 0.7 meV spanning the same field range. Suzuki and Hikita[55] obtained values between 200 meV and 30 meV (also 0.5 to 3 T). For $\mathbf{H} \perp \mathbf{c}$, $U_0(0T)$ is about 100 meV (not plotted), while for $H > 0$, the values are almost constant at about 20 meV up to 7 T. Reference [66] shows corresponding $U_0(H)$ values decreasing from about 1 eV to 0.5 eV from 1 to 7 T and reference [55] from 2 to 1 eV (same field range). Reference [67] quotes a range of 140 to 20 meV for the field dependent activation energy in single crystals of $Nd_{2-x}Ce_xCuO_{4-\delta}$, determined from the frequency dependence of the dissipation peak and the TAFF model (highest field 4 T). Our values of $U_0(H)$ show general agreement, though they tend to be somewhat lower than the other thin-film values.

For $Y_1Ba_2Cu_3O_{6+x}$, the activation energies vary more strongly with q. Notice the different scales on the y–axis of figure 4.16. The values for $\mathbf{H} \parallel \mathbf{c}$ range from 3 eV to 0.8 eV for $q = 1.5$, 10 eV to 1 eV for $q = 2$ and 90 eV to 7 eV for $q = 3$ for an applied field between 1 and 8 T. For $\mathbf{H} \perp \mathbf{c}$, $U_0(H)$ varies from 7 eV to 2 eV for $q = 1.5$, 11 eV to 6 eV for $q = 2$ and from 120 eV to 12 eV for $q = 3$ for the same field region. A comparison with the enhancement method is presented in the next section.

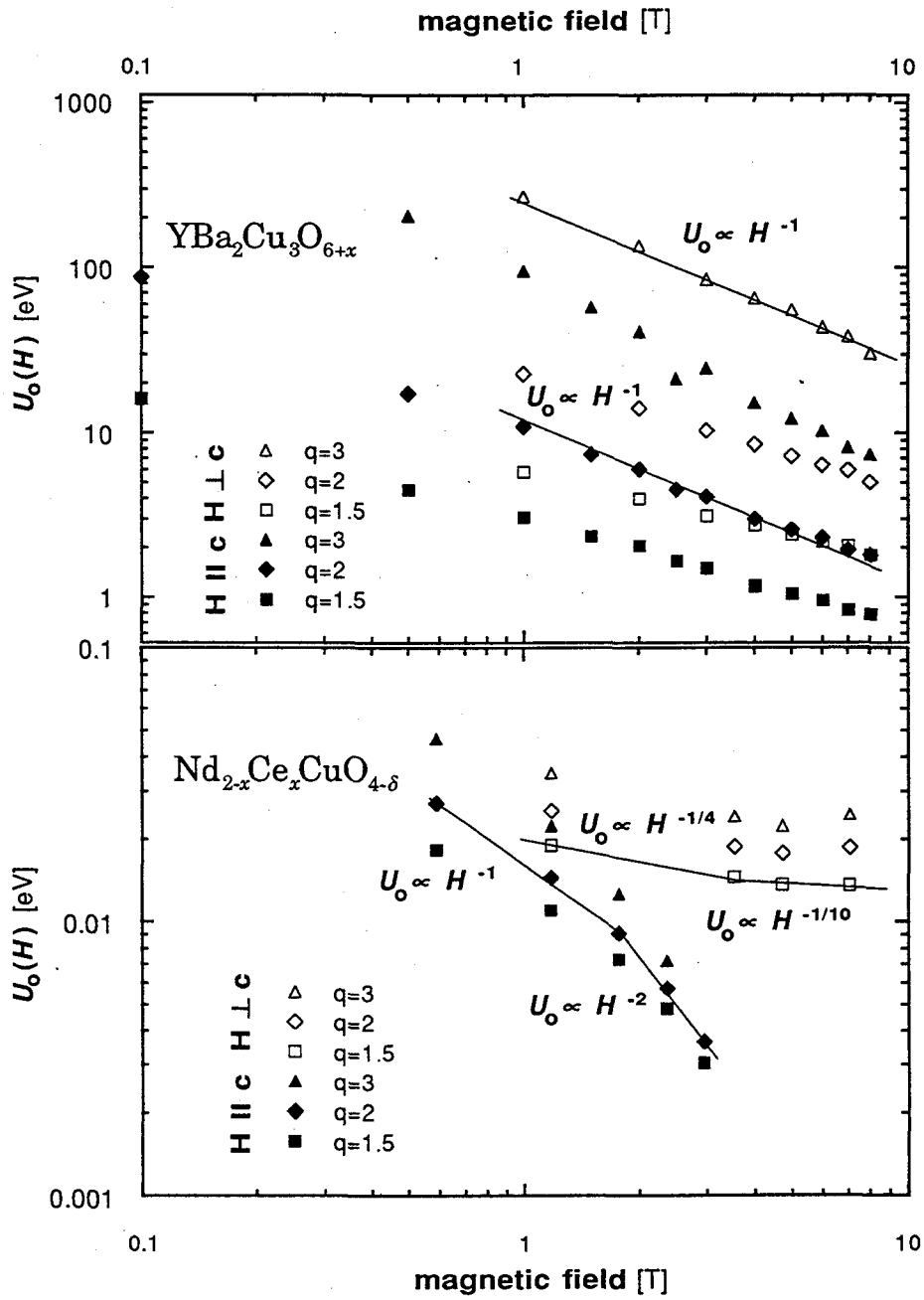

Figure 4.16 Field dependence of the activation energy. $Y_1Ba_2Cu_3O_{6+x}$ follows a H^{-1} dependence for some q, $Nd_{2-x}Ce_xCuO_{4-\delta}$ has a more complicated dependence on H.

In section 3.3 a few theoretical models for $U(H,T)$ predicted a dependence with the magnetic field. We can confirm $U_0 \propto H^{-1}$ for $Y_1Ba_2Cu_3O_{6+x}$ in $\mathbf{H} \perp \mathbf{c}$ orientation for $q = 3$, with slightly weaker dependence for lower q. For $\mathbf{H} \parallel \mathbf{c}$, $q = 2$ gives $U_0 \propto H^{-1}$, while $q = 1.5$ shows a stronger and $q = 3$ a still stronger dependence of $U_0(H)$ on H. $Nd_{2-x}Ce_xCuO_{4-\delta}$ shows a more complicated dependence. Most of the models suggested U_0 *independent* of H, but we find that U_0 is never really independent of H. We observed a very weak dependence for magnetic fields between 4 and 8 T in the $\mathbf{H} \perp \mathbf{c}$ orientation. For low fields in this orientation $U_0 \propto H^{-1/4}$. Our results agree with Fukami *et al.*[66], who were, however, able to measure in 10 T applied field, where the log-log plot takes an downturn once again. For $\mathbf{H} \parallel \mathbf{c}$, almost independently of q, $U_0 \propto H^{-1}$ for low fields and $U_0 \propto H^{-2}$ for high fields, again conforming with [66].

There exists the possibility of using the parameters obtained from the curve fit (formula 34) and plot:

$$\frac{k_B T}{U_0}(\ln\rho - \ln\rho_0)\left(1+(T/T_c)^2\right)^{-2} \text{ vs. } \left(1-(T/T_c)^2\right)\Big/\left(1+(T/T_c)^2\right), \qquad (35)$$

to extract the originally guessed exponent as slope in a double log plot. All data, even of different fields, should fall on a straight line and the slope should reflect the exponent. This is a consistency check on the assumed value for q. Our data fell on a straight line and we obtained values within 0.2 of the initially guessed value of q for both samples. Curve fits with higher values of q showed a greater tendency to result in data points deviating from the straight line for temperatures closer to T_c.

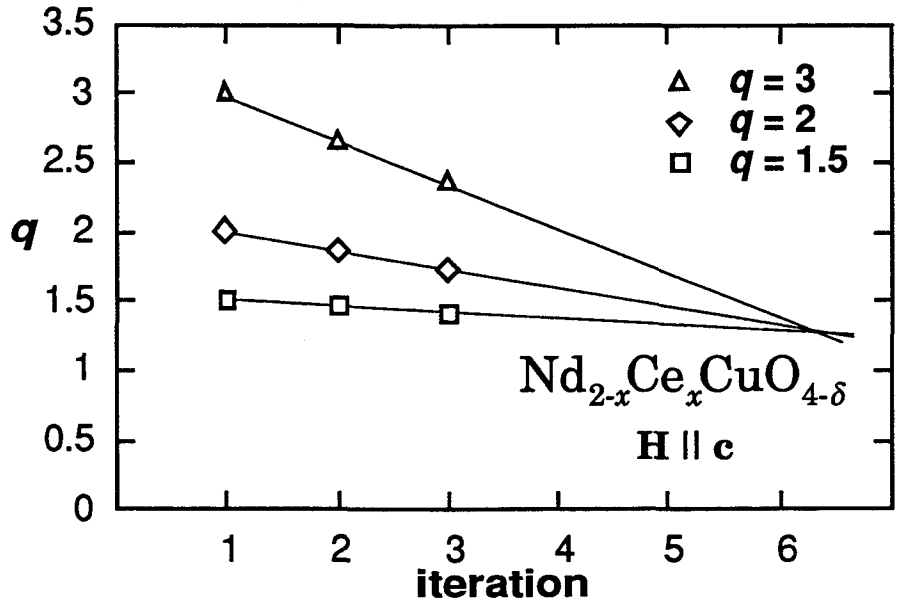

Figure 4.17 Convergence of exponents q. Independent of the starting value the slope yields 1.45, when data when data below 330 μΩ cm are selected.

All along we suspected that how well a particular curve fit, depends on how much data were included at high resistivities. That was the reason why we fit different amount of data in the first place for different q. We suspected that the dispute for $Nd_{2-x}Ce_xCuO_{4-\delta}$ between exponents $q = 2$ or 3 for **H||c** and **H⊥c**[55] or $q = 3$ for both orientations[66] really boils down to how much high temperature data were included into the curve fits. With an iteration method[55] based on taking the slope obtained from plotting (35) as a new starting value for curve fits, we could show that when the data selection with the best fit to $q = 1.5$ is fit to $q = 3$ or 2, that the iteration yields $q = 1.45$, independent of the starting value (see figure 4.17). We could also show that the data window selected for $q = 2$, yields to 2 regardless of wether one started with a higher value of q, like

three. Due to the nature of the functions it is not possible to fit a lower q to data chosen to include high resistivities. We regard our finding as a major result of this work.

Since for higher temperatures and resistivities, different mechanisms like flux flow and fluctuations may play a role, we decided to include only data up to 330 $\mu\Omega$cm and show a plot of (35) for the different values of q in figure 4.18. The straight lines are remarkable.

Three parameters allow quite a degree of freedom however the curve fit is done over a wide region of the data, rather than applying a correction at a special resistivity. Certainly this method is labor-intensive. To obtain one point in the convergence plot (figure 4.17) approximately 2 1/2 hours work of a skilled person are necessary. With the unfortunate fact that the exponent q depends on the data range chosen, a lot of power of this method is lost. However if one could find an upper limit which data should be included, this method would certainly be powerful to find the exponent in the temperature dependence of $U(T,H)$.

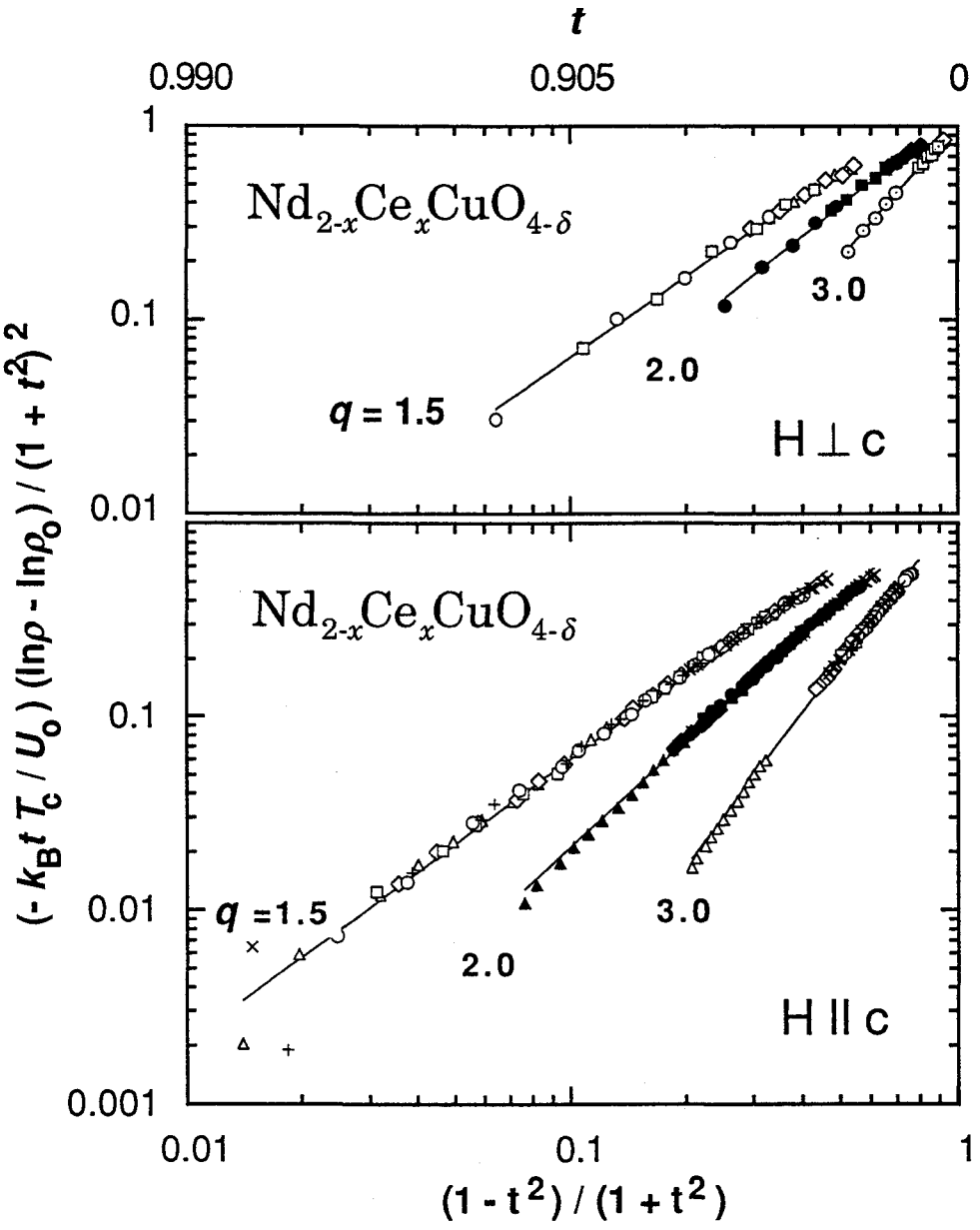

Figure 4.18 Double log plot which yields q from the slope. Here the same data were fit with q = 1.5, 2 and 3. Notice the shallower slopes for q = 2 and q = 3.

4.7 Summary and Comparison of the Two Methods

We found it necessary to introduce a temperature dependent activation energy. The activation energy at a particular temperature and in the limit $T \to 0$, can be obtained in two ways. The enhancement method, commonly used for $Y_1Ba_2Cu_3O_{6+x}$ allows one to obtain a fast estimate to compare with other people. The three parameter fit requires much more effort, however it also provides information about T_c and ρ_0. A full comparison of both methods is shown in table 4.4. While the methods do compare well for $q = 1.5$ and $q = 2$, discrepancies occur for $q = 3$ and $\mathbf{H} \perp \mathbf{c}$. For the highest field, agreement is particularly good. Data in ambient field were not included in this comparison, since the enhancement methods resulted in a factor two or three higher activation energies U_0.

	$Nd_{2-x}Ce_xCuO_{4-\delta}$				$Y_1Ba_2Cu_3O_{6+x}$			
	U_0[meV]: **H⊥c**		U_0[meV]: **H‖c**		U_0 [eV]: **H⊥c**		U_0 [eV]: **H‖c**	
from:	*enh*	fit	*enh*	fit	*enh*	fit	*enh*	fit
$q = 1.5$	18-13	≈ 15	17-3	20-3	3-1	7-2	2-0.5	3-0.8
$q = 2$	27-18	≈ 20	26-4	30-3.5	12-3	11-6	7-1	10-1
$q = 3$	69-39	≈ 25	68-4	40-4	213-22	120-12	100-8	90-7

Table 4.4 Comparison of the activation energies at zero temperature U_0 obtained by two different methods. *Enh* refers to the method described in chapter 4.5, fit to the three parameter fit of chapter 4.6. Only identical field ranges were compared.

5. Conclusions

A series of transport measurements were performed on the high temperature superconductors $Y_1Ba_2Cu_3O_{6+x}$ and $Nd_{2-x}Ce_xCuO_{4-\delta}$. Current - voltage isotherms were measured at different magnetic fields, and resistivity - temperature data were obtained for different fields and different applied currents.

The broadening of the resistive transition was modelled using a formalism based on thermally activated flux motion and the activation energies and other parameters in this formalism were compared with published results. Two different methods of extracting the activation energies were used and compared. The three parameter method proved that $Y_1Ba_2Cu_3O_{6+x}$ can be fit very well to higher exponents of q in (32) despite the fact the commonly only $q = 1.5$ is used. For $Y_1Ba_2Cu_3O_{6+x}$, the field dependence of the activation energy clearly favors Malozemoff's and Tinkham's model with $q = 1.5$. However, some models yielding higher exponents may be revised to predict the correct field dependence. The dispute over $Nd_{2-x}Ce_xCuO_{4-\delta}$ to fit to $q = 2$ and 3 (for $\mathbf{H} \perp \mathbf{c}$ and $\mathbf{H} \parallel \mathbf{c}$ respectively) or $q = 3$ for both cases, could be resolved, by showing that the exponent depends on the data range included into the curve fit. Unfortunately no clear decision in favor one of the reviewed models describing the activation energy could be made for $Nd_{2-x}Ce_xCuO_{4-\delta}$.

In general, the results agree well with published work and we have shown that the discrepancies that do exist can be explained rather simply by the range of data included in the fits. Values of the upper

critical field $H_{c2}(T=0)$ and hence the coherence length were obtained from the resistivity data.

The current - voltage characteristics of both materials clearly demonstrate the validity of thermal activation models, showing regions where thermally activated flux flow applies, and where flux creep is the dominant mechanism. Behavior consistent with a transition to a vortex-glass state, where flux lines show longer range coherence and their motion is severely restricted, was observed. In the region around this transition, the isothermal current-voltage curves scale onto two universal curves, one above and the other below the glass transition temperature. We obtained values for the scaling exponents which agree with those obtained for other $Y_1Ba_2Cu_3O_{6+x}$ thin films, but which differ from values obtained for single crystals.

It proved successful to analyze current-voltage characteristics together with resistivity - temperature curves. The regions where the vortex glass, TAFF and creep models are applicable could be clearly defined in field, current and temperature space.

Careful rewiring of the system resulted in a reduced noise level, that gave the stable and reproducible data presented here. Mostly, the noise level was below 40 nV, with the best result being ±10 nV over half an hour. The correct parameters to control the temperature stabilization were established. This was especially important for current - voltage isotherms, and to avoid hysteresis in the resistance-temperature curves. A record temperature stability of less than 1 mK over 15 min was obtained, and a typical stability of 5 mK. The software to automate the data-taking and analysis was rewritten and vastly improved.

Bibliography

1. Y. Tokura, H. Takagi, and S. Uchida, *Nature*, Vol. **337**, 345 (1989).
2. V. J. Emery, *Nature,* **337**, 306 (1989).
3. S. Kubo, and M. Suzuki, *Physica C.* Vol. **185-189**, 1251 (1991).
4. S. A. Wolf and V. Z. Kresin, *Fundamentals of Superconductivity,* (Plenum Publishing Corporation, New York, NY, 1990).
5. J. G. Bednorz and K. A. Müller, *Z. Physik B*, Vol. **64**, 379 (1987).
6. M. Tinkham, *Introduction to Superconductivity* (Robert E. Krieger Publishing Company, Inc., Malabar, FL, 1985).
7. W. Warnes, *Principles on Superconductivity, Metals Handbook*, Vol. **2**, 1030 (ASM International, 1990).
8. H. Ullmaier, *Irreversible Properties of Type II Superconductors* (Springer Verlag, Berlin, 1975).
9. A. C. Rose-Innes and F. H. Rhoderick, *Introduction to Superconductivity* (Pergamon Press, 1969).
10. R. D. Parks, *Superconductivity* (Marcel Dekker, Inc., New York, 1969), Vol. **2**.
11. M. Gurvitch, J. M. Valles, Jr., A. Cucolo, R. C. Dynes, J. Carno, L. F. Schneemeyer, and J. V. Waszczak, *Phys. Rev. Lett., Vol.* **63**, 1008 (1989).
12. W. W. Warren, Jr., R. Waldstedt, G. Brennert, G. Espinosa, and J. Remeika, *Phys. Rev. Lett.*, Vol. **59**, 1860 (1987).
13. R. Fischer, J. Gordon, and N. Phillips, *J. Superconductivity*, Vol. **1**, 231 (1988).
14. A. Kussmaul, *PhD Thesis; MIT*, 18 (1992), unpublished.

15. H. Oyanagi, Y. Yokoyama, H. Yamaguchi, T. Katayama, Y. Nishihara, Y. Kuwahara, *Physica C*, Vol. **185-189**, 841 (1991).
16. J. Tate and B. A. Hermann, *Physica C*, Vol. **193**, 207 (1992).
17. P. Berberich, J. Tate, W. Dietsche, and H. Kinder, *Applied Phys. Lett.*, Vol. **53**, 925 (1988).
18. LakeShore DRC-91CA Temperature Controller, *Users Manual*, 3-8.
19. U. Eschmann and H. Träuble, *Phys. Lett.*, Vol. **24A**, 526 (1967).
20. N. Missert, J. Clarke, D. Fork, L. Lombardo, and A. Kapitulnik *Proceedings of the Americ. Phys. Society, March Meeting, p.382* (1992).
21. A. Tonomura, *presented at the workshop: Microstructure of Magnetic Materials* (Wickenburg, Arizona Jan. 8-11, 1992).
22. H. F. Hess, R. B. Robinson, R. C. Dynes, J. M. Valles, Jr. and J. V. Waszczak, *Phys. Rev. Lett.*, Vol.**62**, 214 (1989).
23. J. D. Shore, M. Huang, R. C. Dorsey, and J. P. Sethna, *Phys. Rev. Lett.*, Vol. **62**, 3089 (1989).
24. L.G. Aslamasov, A. J. Larkin, *Phys. Lett.*, Vol. **26A**, 238 (1968).
25. K. Maki, *Prog. Theor. Phys.*, Vol. **39**, 897 (1968).
26. R. S. Thompson, *Phys. Rev. B*, Vol. **1**, 327 (1970).
27. W. E. Lawrence and S. Doniach, *Proceedings of the 12th Int. Conf. on Low Temp. Phys.* edited by E. Kanda (Academic Press of Japan, Kyoto, 1971), *p.* 361.
28. R. Hopfengärtner, B. Hensel, and G. Saemann-Ischenko, *Phys. Rev. B*, Vol. **44**, 741 (1991).
29. G. Weigang and K. Winzer, *Zeit. Phys. B*, Vol. **77**, 11 (1989).

30. Y. B. Kim, C. F. Hempsted, and A. R. Strnad, *Phys. Rev.*, Vol. **139**, A 1163, (1965).

31. Z. Yuheng, L. Xiao-Guang and C. Linq, *Phys. Rev. B*, Vol. **44**, 12009 (1991).

32. M. P. A. Fisher, *Phys. Rev. Lett.*, Vol. **62**, 2661 (1991).

33. M. P. A. Fisher and D. A. Huse, *Phys. Rev. B*, Vol. **43**, 130 (1991).

34. R. H. Koch, V. Foglietti, W. J. Gallagher, G. Koren, A. Gupta, and M. P. A. Fisher, *Phys. Rev. Lett.*, Vol. **63**, 1511 (1989).

35. N.-C. Yeh, W. Jiang, D. S. Reed, A. Gupta, F. Holtzberg and A. Kussmaul, *Phys. Rev. B*, Vol. **45**, 5710 (1992).

36. D. A. Huse, M. P. A. Fisher, and D. S. Fisher, submitted to *Nature* (1992).

37. J. M. Kosterlitz and D. J. Thouless, *J. Phys. C*, Vol. **6**, 1181 (1973).

38. J. Halbritter, *J. Appl. Phys.*, Vol. **71**, 339 (1992).

39. K. A. Müller, M. Takashige, and J. G. Bednorz, *Phys. Rev. Lett.*, Vol. **58**, 1143 (1987).

40. T. Tsuneto, *J. Phys. Soc. Jpn.*, Vol. **57**, 3499 (1988).

41. W. K. Kwok, U. Welp, G. W. Crabtree, K. G. Vandervoort, and J. Z. Liu, *Int. Conf. on Highly Corr. Electrons; Santa Fe, New Mexico* (1989).

42. S. Kambe, M. Naito, K. Kitazawa, I. Tanaka and H. Kojima, *Physica C*, Vol. **160**, 243 (1989).

43. Y. Iye, S. Nakamura, and T. Tamegai, *Physica C*, Vol. **159**, 433 (1989).

44. K. C. Woo, K. E. Gray, R. T. Kampwirth, J. H. Kang, S. J. Stein, R. East and D. M. McKay, *Phys. Rev. Lett.*, Vol. **63**, 1877 (1989).

45. B. I. Ivlev and N. B. Kopnin, *Europhys. Lett.*, Vol. **15**, 349 (1991).

46. E. H. Brandt, *Int. Conf. on Transport Properties of SC; Rio de Janeiro, Brazil* (1990).

47. P. W. Anderson, *Phys. Rev. Lett.*, Vol. **9**, 309 (1962).

48. E. H. Brandt, *Physica C*, Vol. **162-164**, 276, 1167 (1989).

49. E. H. Brandt, *Physica C*, Vol. **185-189**, 270-275 (1991).

50. N.-C. Yeh, W. Jiang, D. S. Reed, U. Kriplani, and F. Holtzberg, submitted to *Phys. Rev. Lett.*.

51. J. Tate, B. A. Hermann, and J. Roberts, in preparation.

52. B. A. Hermann and J. Tate, in preparation.

53. E. Helfand and N. R. Werthamer, *Phys. Rev. B*, Vol. **147**, 288 (1966).

54. T. Fukami , K. Hayashi, T. Nishizaki, Y. Horie, V. Soares, T. Aomine, and L. Rinderer, *Int. Conf. on Advanced Materials: High Tc SC Thin Films, Straßbourg, France* (1991).

55. M. Suzuki and M. Hikita, *Phys. Rev. B*, Vol.**41**, 9566 (1990).

56. C. C. Almasan, S. H. Han, E. A. Early, B. W. Lee, C. L. Seaman, and M. B. Maple, *Phys. Rev. B*, Vol. **45**, 1056 (1992).

57. M. R. Beasley, R. Labusch, and W. W. Webb, *Phys. Rev.*, Vol. **181**, 682 (1969).

58. J. R. Clem, *Phys. Rev. B*, Vol. **43**, 7837 (1991).

59. W. W. Webb, *Phys. Rev. Lett.*, Vol. **11**, 191 (1963).

60. Y. Yeshurun and A. P. Malozemoff, *Phys. Rev. Lett.*, Vol. **60**, 2202 (1988).

61. M. Tinkham, *Phys. Rev. Lett.*, Vol. **61**, 1658 (1988).

62. D. S. Fisher, *Phys. Rev. B*, Vol. **22**, 1190 (1980).

63. N.-C. Yeh, *Phys. Rev. B*, Vol. **40**, 4566 (1989).

64. A. P. Malozemoff, T. K. Worthington, E. Zeldov, N.-C. Yeh, M. W. McElfresh, and F. Holtzberg, *Strong Correlations and Superconductivity* (Springer Series in Solid State Sciences, Vol.89; Springer-Verlag Berlin Heidelberg, p. 349-360).

65. T. T. Palstra, B. Batlogg, R. B. van Dover, L. F. Schneemeyer, and J. V. Waszczak, *Phys. Rev. B*, Vol. **41**, 6621 (1990).

66. T. Fukami, K. Hayashi, T. Yamamoto, T. Nishizaki, Y. Horie, F. Ichikawa, T. Aomine, V. Soares, and L. Rinderer, *Physica C*, Vol. **184**, 65 (1991).

67. L. Fabrega, M. A. Cruesellas, J. Fontcuberta, X. Obradors, S. Piñol, C. J. van der Beek, P. H. Kes, T. Grenet and J. Beille, *Physica C*, preprint.

Appendices

Appendix A

Rutherford backscattering (RBS) results and an x-ray diffraction pattern for a $Y_1Ba_2Cu_3O_{6+x}$ sample similar to the one examined in this thesis are shown in figure A.1. $Nd_{2-x}Ce_xCuO_{4-\delta}$ RBS results are not shown, there the ceria and neodymium peaks cannot be resolved because their atomic numbers are too close to each other.

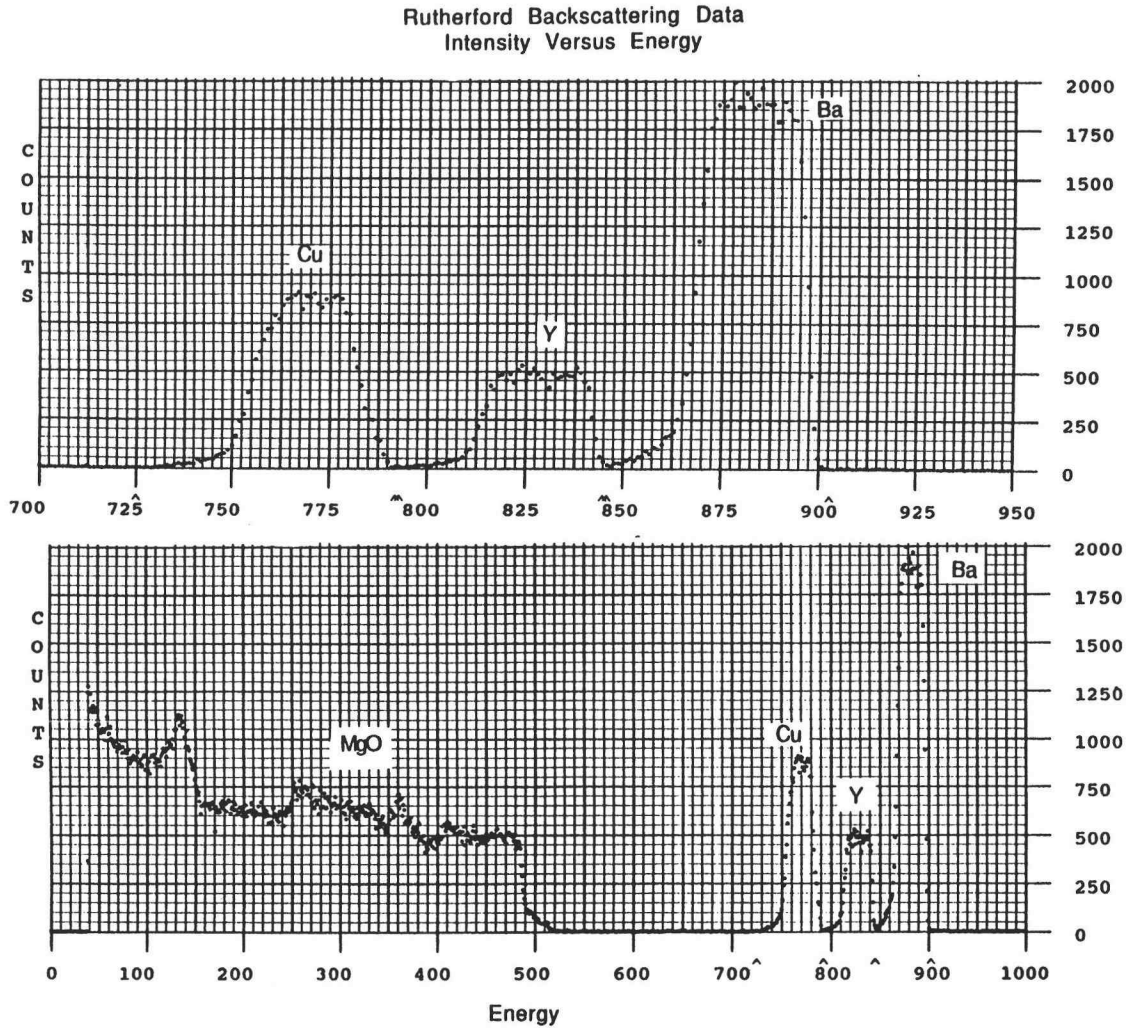

Figure A.1 RBS data for $Y_1Ba_2Cu_3O_{6+x}$.

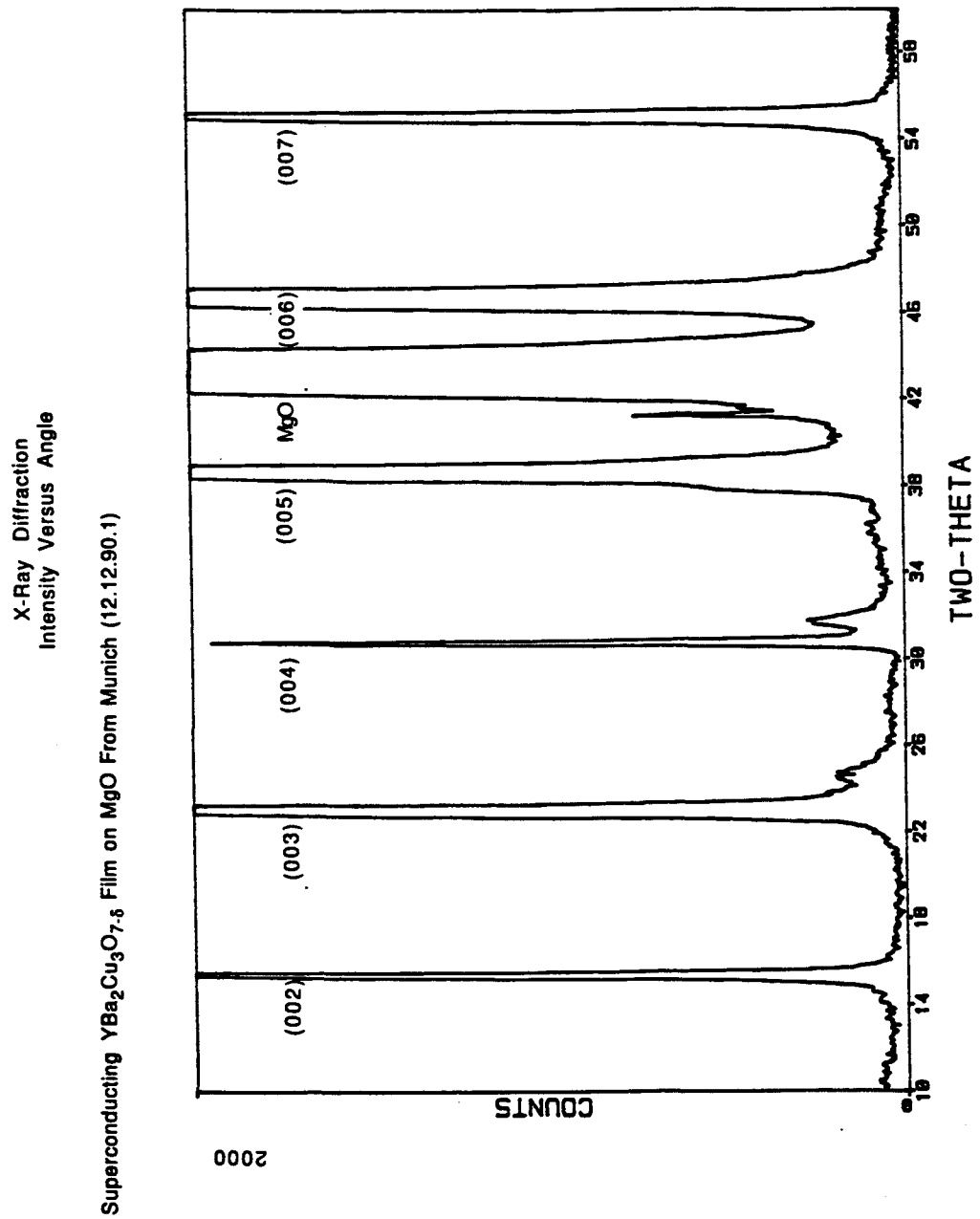

Figure A.2 X-ray pattern for $Y_1Ba_2Cu_3O_{6+x}$.

Appendix B

Complementary results for the enhancement analysis described in chapter 4.5 are shown in table B.1. We applied this analysis at temperatures $T(\rho = 1\% \ \rho_n)$, which corresponds to $\rho = 6.5$ μΩcm for $Nd_{2-x}Ce_xCuO_{4-\delta}$ and $\rho = 2.7$ μΩcm for $Y_1Ba_2Cu_3O_{6+x}$. T_c was defined as T at $\rho = 90\% \ \rho_n$ and q=1.5 was used in (33).

a.)	$\mu_0 H$ [T]	T_c [K]	slope [meV]	$1/T$ [K^{-1}]	$t = T/T_c$	enh	U_{red} [meV]
H ⊥ c	0.00	19.9	74.62	0.0562	0.8942	12.5	5.958
	1.18	19.2	29.94	0.0673	0.7723	5.1	5.917
	3.53	18.7	23.00	0.0721	0.7417	4.3	5.332
	4.71	18.3	21.29	0.0741	0.7374	4.2	5.041
	7.07	18.1	21.31	0.0748	0.7386	4.2	5.016
H ∥ c	0.00	20.0	64.26	0.0572	0.8741	10.0	6.250
	0.58	17.5	28.19	0.0732	0.7806	5.3	5.318
	1.18	15.4	17.22	0.0910	0.7135	3.8	4.563
	1.77	13.4	11.47	0.1130	0.6604	3.0	3.802
	2.36	11.7	7.477	0.1438	0.5944	2.4	3.144
	2.94	9.7	4.76	0.1890	0.5455	2.0	2.332
b.)	$\mu_0 H$ [T]	T_c [K]	slope [eV]	$1000/T$ [K^{-1}]	$t = T/T_c$	enh	U_{red} [meV]
H ⊥ c	1	90.75	3.542	11.457	0.96179	37.541	94.351
	2	90.75	2.738	11.546	0.95438	31.172	87.835
	3	90.75	2.343	11.631	0.94741	26.818	87.367
	4	90.75	2.113	11.699	0.94190	24.120	87.605
	5	90.75	1.865	11.754	0.93749	22.303	83.619
	6	90.75	1.780	11.813	0.93281	20.636	86.259
	7	90.75	1.738	11.860	0.92911	19.475	89.244
	8	90.75	1.549	11.977	0.92004	17.081	90.683

Table B.1 U_{red} for a.) $Nd_{2-x}Ce_xCuO_{4-\delta}$ and b.) $Y_1Ba_2Cu_3O_{6+x}$. See also paragraph 4.5 and table 4.3.

Appendix C

The data acquisition program is presented here. The main program is attached in a map pocket. The following program listing, starts with the hidden windows of the main program and then lists the subroutines in alphabetical order.

LabVIEW II is written in a form similar to a circuit diagram. The wires are the line number and command pathways and the order of execution is data driven. The program consists of four main structures - a "film strip", case statement, "while loop" and "for loop". The film strip regulates the order of execution similar to conventional programming languages in which the commands are executed in order of the line numbers. The subroutines within a film strip are executed following the film strip number. Only after the whole film strip is finished will the program continue. The case statement is very much like a "if x = true, then..." in Basic. The while loop is identical to the do while loop used in FORTRAN and other programming languages. The for loop corresponds to "for i = 1 to N do ..., after that goto ...".

The program is organized from upper left to lower right similar to a written page. Further information can be obtained in the LabVIEW II manual.

Connector Pane and Description

R-T/I-V 182nVM version 3.1

R-T/I-V version 3.1 main program
Measures voltage across superconductor with either varying current and constant temperature or varying temperature and constant current. Controls temperature. Plots and saves data in different options.

Frames are numbered:

convention:
f : film strip ; c : case statement
F : false ; T : true

example: f3.6 /c2.F /c1.0

f3.: third film strip in main program
6 : picture #6 in film strip
/c : previous mentioned frame contains case statement
c2.: second case statement in that frame
F : false case
/c : previous mentioned frame contains case statement
c1.: first (possibly only) case statement in that frame
0 : case #0 of case statement

Programmer Bianca

c2.F to c6.F

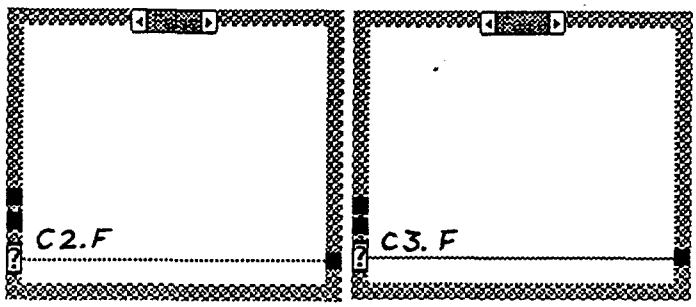

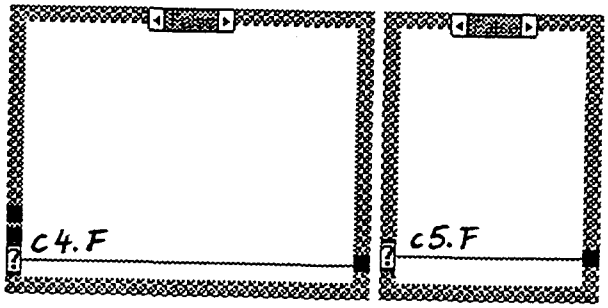

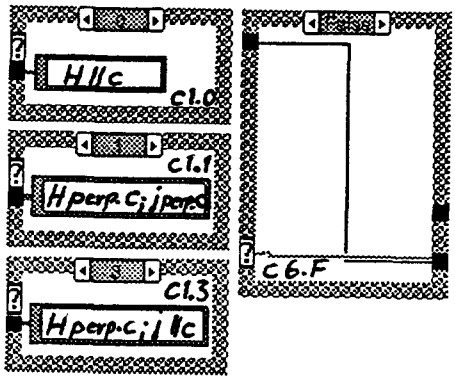

f1.4/c1.F and f1.0

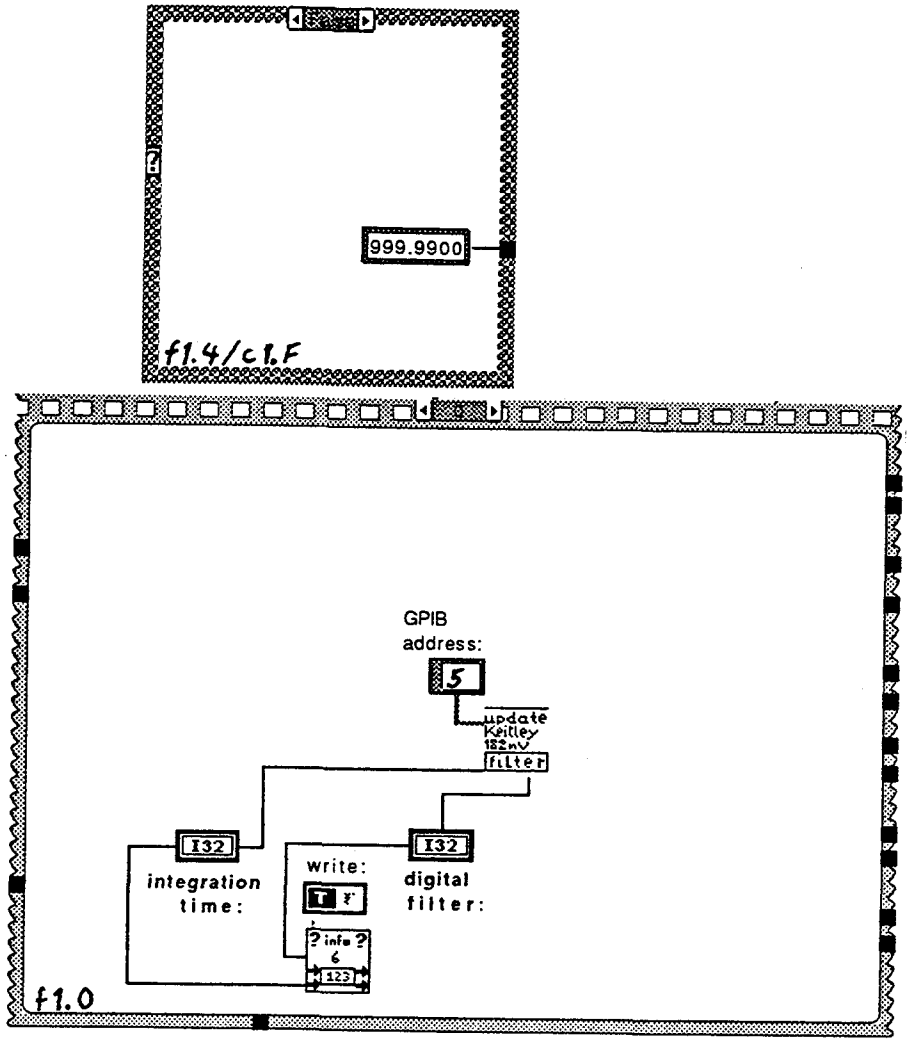

f1.1 and f1.2

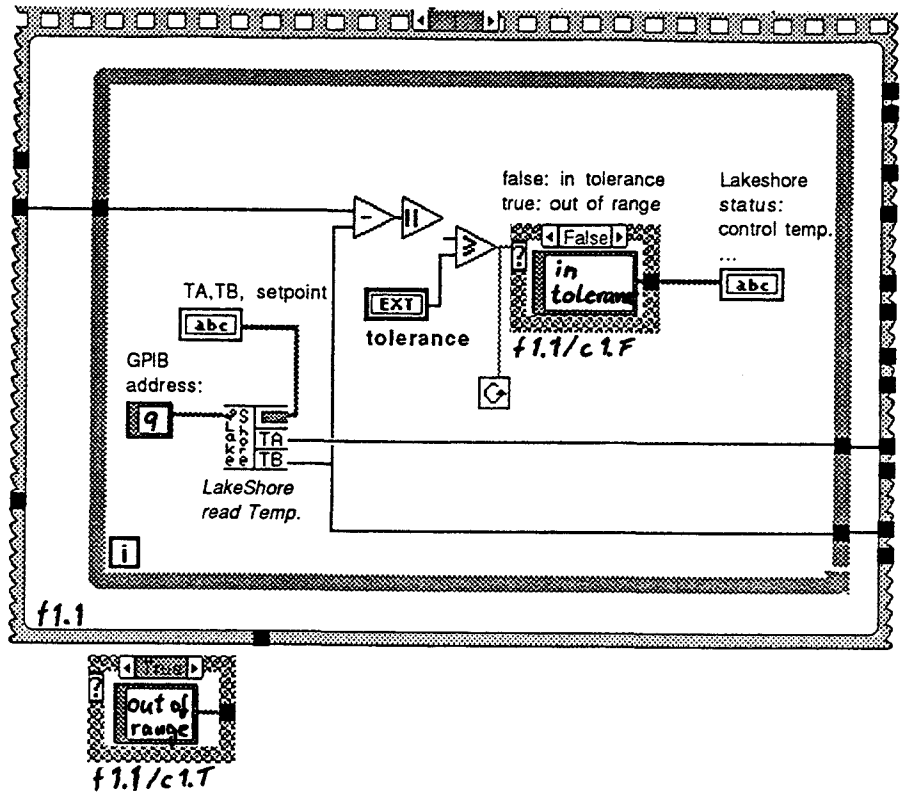
false: in tolerance
true: out of range
Lakeshore
status:
control temp.
...
False
in tolerance
abc
TA,TB, setpoint
EXT
tolerance
f1.1/c1.F
GPIB
address:
9
error
TA
TB
LakeShore
read Temp.
f1.1
out of range
f1.1/c1.T

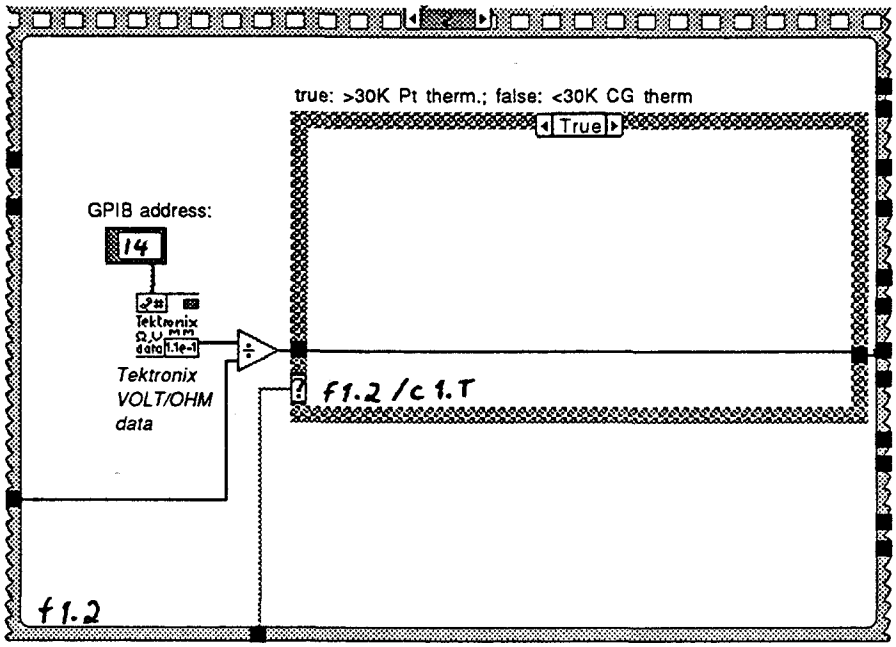
true: >30K Pt therm.; false: <30K CG therm
True
GPIB address:
14
Tektronix
Tektronix
VOLT/OHM
data
f1.2 /c 1.T
f1.2

f1.2 to f1.5

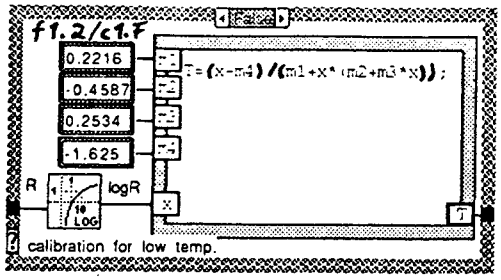
f1.2/c1.F
False
0.2216
-0.4587
0.2534
-1.625
T=(x-m4)/(m1+x*(m2+m3*x));
R
logR
10 LOG
calibration for low temp.

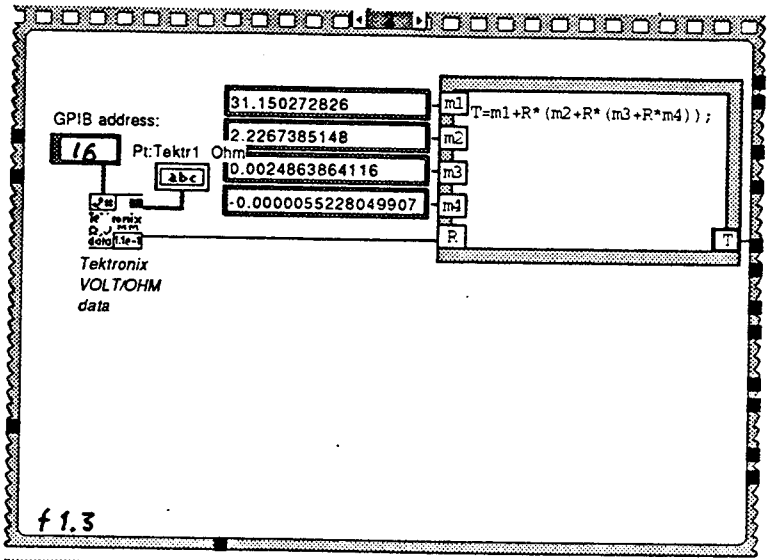
GPIB address:
16
Pt:Tektr1 Ohm
abc
Tektronix VOLT/OHM data
31.150272826
2.2267385148
0.0024863864116
-0.0000055228049907
m1
m2
m3
m4
R
T=m1+R*(m2+R*(m3+R*m4));
T
f1.3

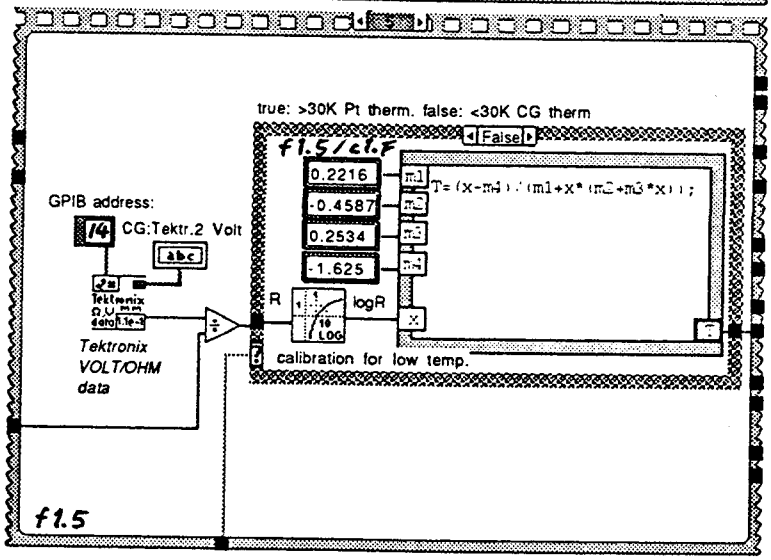
true: >30K Pt therm. false: <30K CG therm
f1.5/c1.F
False
0.2216
-0.4587
0.2534
-1.625
T=(x-m4)/(m1+x*(m2+m3*x));
GPIB address:
14
CG:Tektr.2 Volt
abc
Tektronix VOLT/OHM data
R
logR
10 LOG
calibration for low temp.
f1.5

f1.5/c1.T and f1.6

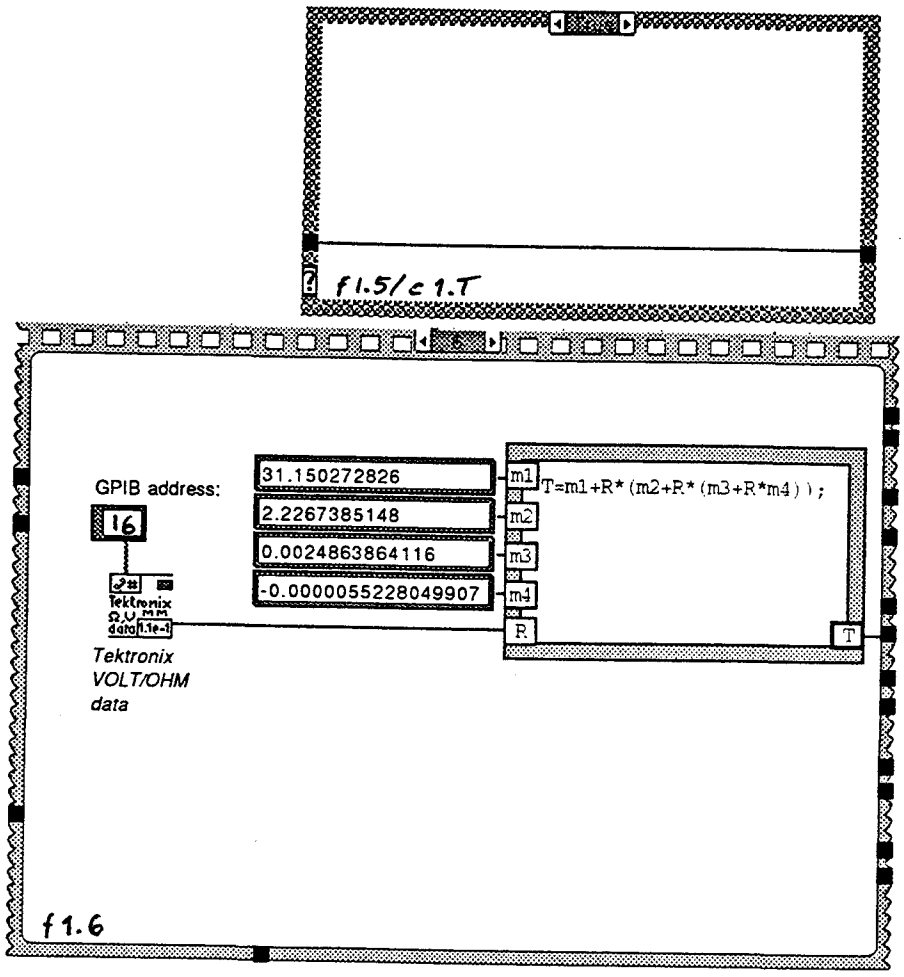

f1.7 and f1.8

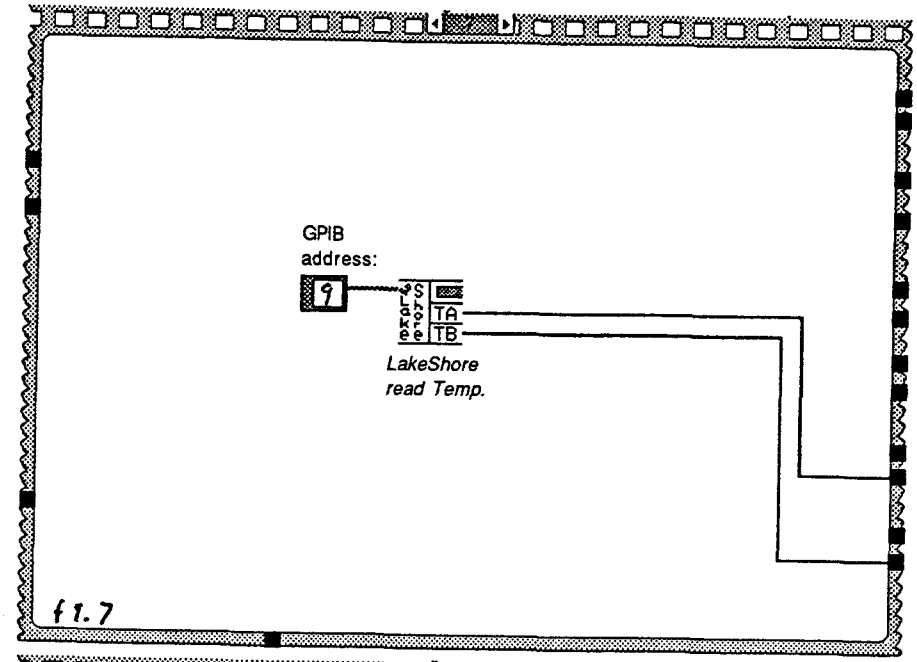
GPIB
address:
9
LakeShore
TA
TB
LakeShore
read Temp.
f1.7

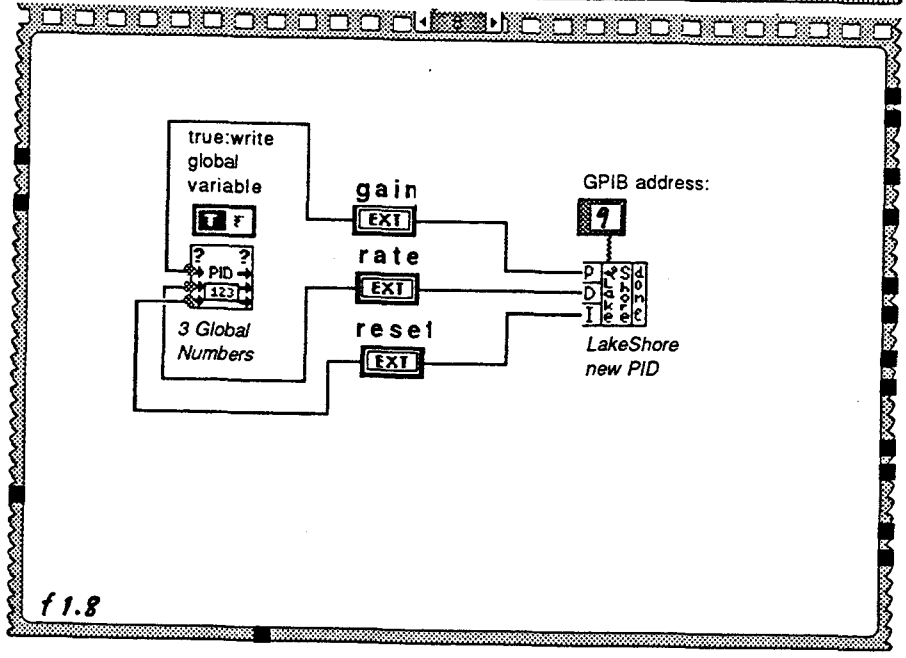
true:write
global
variable
T F
PID
123
3 Global
Numbers
gain
EXT
rate
EXT
reset
EXT
GPIB address:
9
P
D
I
LakeShore
new PID
f1.8

f1.9

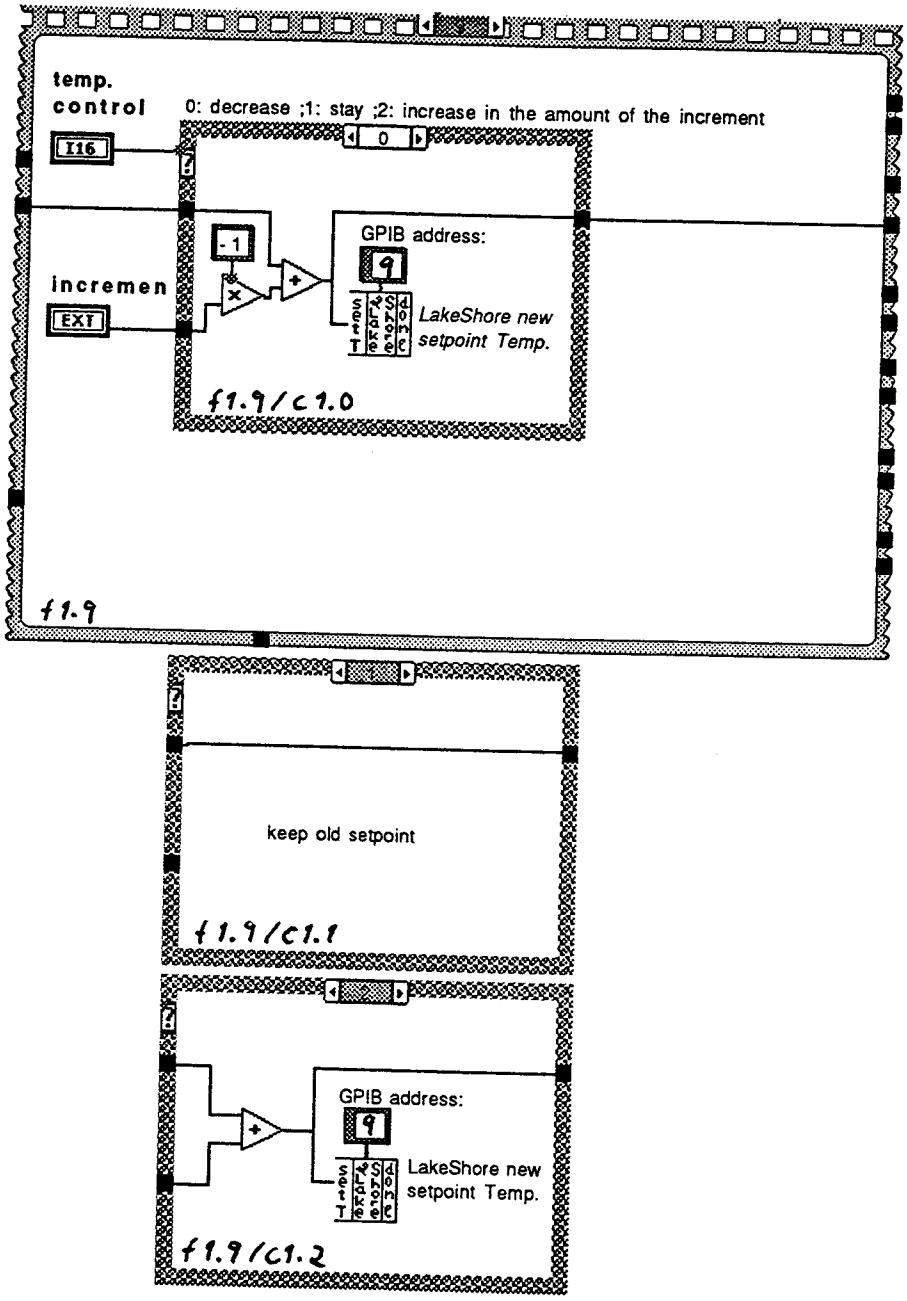
temp.
control
0: decrease ;1: stay ;2: increase in the amount of the increment
I16
0
-1
GPIB address:
9
incremen
EXT
LakeShore new
setpoint Temp.
f1.9/c1.0
f1.9
keep old setpoint
f1.9/c1.1
GPIB address:
9
LakeShore new
setpoint Temp.
f1.9/c1.2

c7 to c9

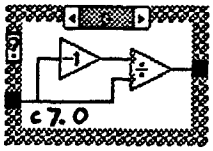

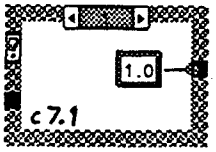

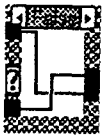

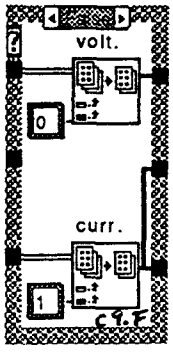

c10.1 and c11

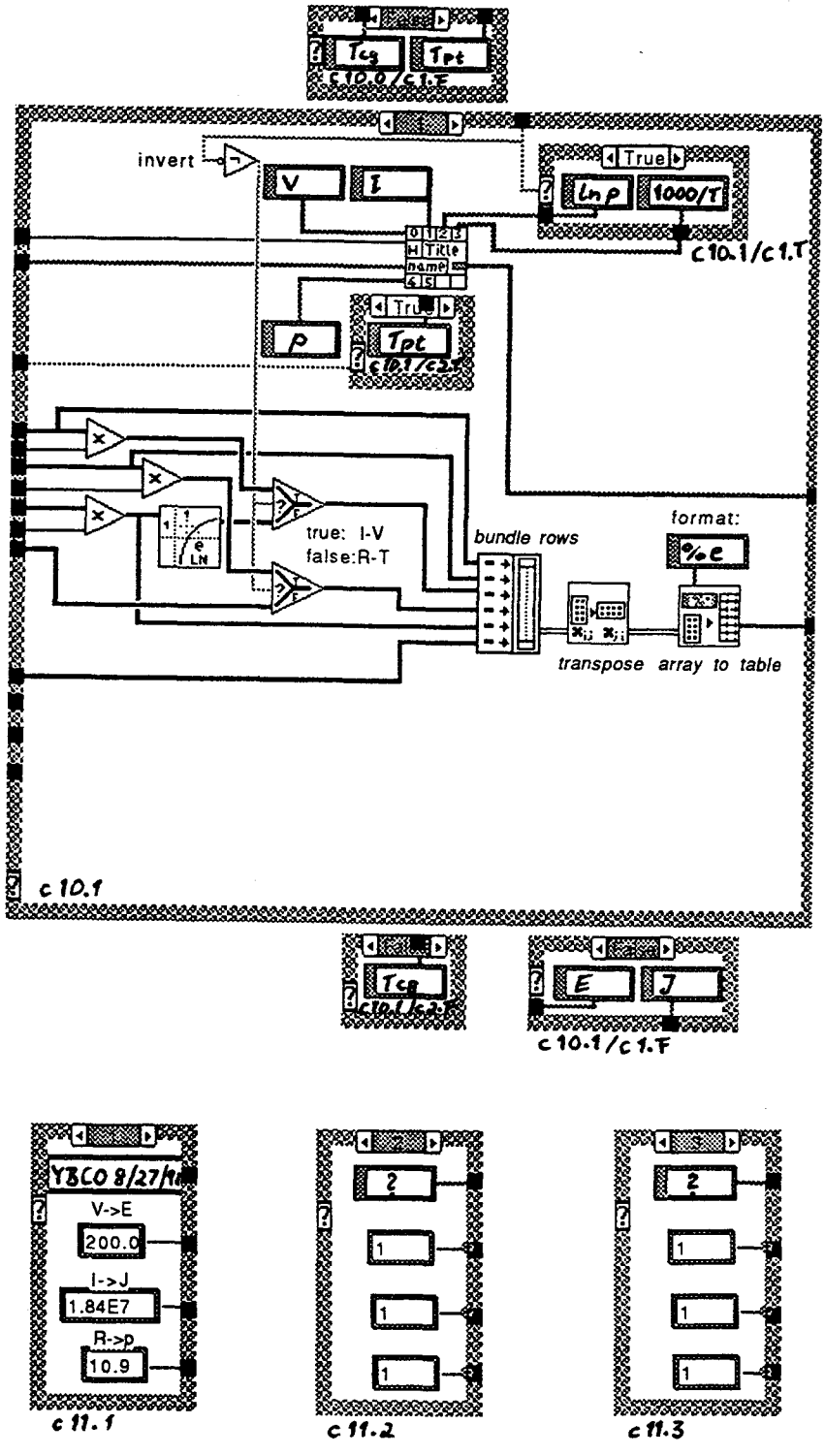
Tcg
Tpt
c10.0/c1.E
invert
V
I
True
Ln ρ
1000/T
c10.1/c1.T
Title
name
ρ
Tpt
c10.1/c2.T
true: I-V
false:R-T
bundle rows
format:
%e
transpose array to table
c10.1
Tcg
c10.1/c2.F
E
J
c10.1/c1.F
YBCO 8/27/
V->E
200.0
I->J
1.84E7
R->p
10.9
c11.1
2
1
1
1
c11.2
2
1
1
1
c11.3

c10.2

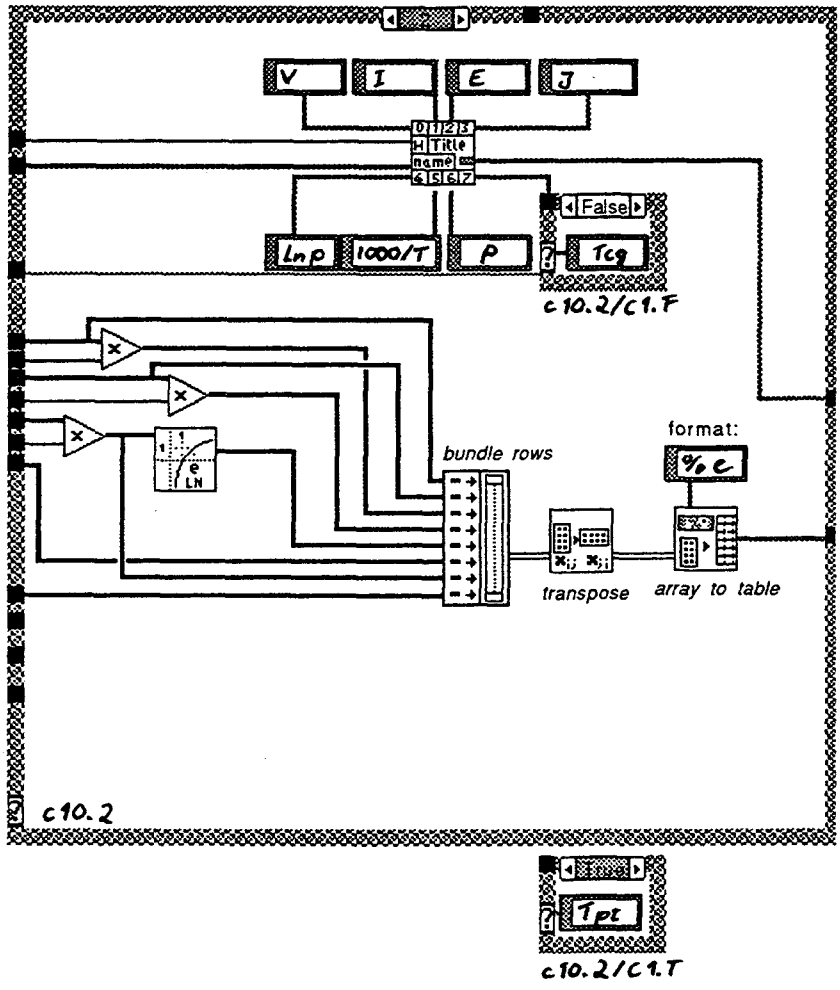
V
I
E
J
Title
name
False
lnp
1000/T
P
Tcg
c10.2/c1.F
bundle rows
format:
%.c
transpose
array to table
c10.2
Tpt
c10.2/c1.T